FABRICATION AND MEASUREMENT OF GRAPHENE ELECTROCHEMICAL MICROELECTRODES

A thesis submitted to The University of Manchester for the degree of
Doctor of Philosophy
in the Faculty of Engineering and Physical Sciences

2016

Stefan David Goodwin

School of Electrical and Electronic Engineering

List of contents

Total word count: 29416

List of figures and tables

All figures were created by the author unless otherwise stated. All illustrations and diagrams are not to scale unless otherwise stated.

List of acronyms

2D – Two dimensions/dimensional

3D – Three dimensions/dimensional

AFM – Atomic force microscope

C_{dl} – Double layer capacitance

CE – Counter electrode

C_g – Geometric capacitance

C_q – Quantum capacitance

C_T – Total capacitance

CV – Cyclic voltammetry

CVD – Chemical vapour deposition

DF – Dark field

DoS – Density of electronic states

DP – Dirac Point

EDL – Electrochemical double layer

FET – Field effect transistor

FFT – Fast Fourier transform

FWHM – Full width at half maximum

GO – Graphene oxide

h-BN – Hexagonal boron nitride

HMDS – Hexamethyldisilazane

HOPG – Highly ordered pyrolytic graphite

IHP – Inner Helmholtz plane

OHP – Outer Helmholtz plane

OTS – Octadecyltrichlorosilane

PMMA – Poly(methyl-methacrylate)

PTFE – Poly(tetra-fluoroethylene)

RE – Reference electrode

rGO – Reduced graphene oxide

RIE – Reactive ion etching

SEM – Scanning electron microscope/microscopy

SNR – Signal to noise ratio

TEM – Transmission electron microscope/microscopy

UME – Ultra-micro-electrode

vdW – Van der Waals

WE – Working electrode

The University of Manchester

Stefan David Goodwin

Doctor of Philosophy (PhD)

Fabrication and measurement of graphene electrochemical microelectrodes

March 2016

Abstract

The electrochemical properties of graphene were investigated using a novel and clean method to fabricate device structures with mechanically exfoliated graphene samples. Graphene is known as being particularly sensitive to both contaminating fabrication methods and the substrate it is placed on, with these effects being detrimental to accurate research into the fundamental properties and sensing applications of graphene. This thesis presents micron scale graphene electrodes that have not been subject to polymer contamination or micro-lithography methods. The effect of utilising atomically flat hexagonal boron nitride as a substrate material was investigated, believed to be the first example of this for graphene electrochemical measurements.

Cyclic voltammetry demonstrated the expected steady-state behaviour for microelectrodes in the hemispherical diffusion regime. The reduction of $IrCl_6^{2-}$ in weak KCl electrolytes was studied to investigate the electron transfer characteristics of the graphene devices and the reproducibility of the measurements. Average values of the standard rate constant, k^0 and the transfer coefficient, α were found to be $3.04 \pm 0.78 \times 10^{-3}$ cms^{-1} and 0.272 ± 0.024 respectively. These values differ significantly from previous similar studies, with the effect of reduced charge doping from the substrate and the potential dependence of the density of electronic states thought to account for the differences. Despite the clean fabrication methods, a relatively large variation between separate devices was found, highlighting an inherent variation in the properties of graphene samples.

DECLARATION

No portion of the work referred to in this thesis has been submitted in support of an application for another degree or qualification of this or any other university or other institute of learning.

COPYRIGHT STATEMENT

Acknowledgements

I'd like to thank my supervisors, Dr. Bruce Grieve, Dr. Ernie Hill and Prof. Matthew Cobb for guiding me through the ups and downs of completing a PhD project.

I'd like to thank my friends and family for their moral support. Being clever and good at science doesn't get you anywhere without these people.

There is a long list of people that need recognition for their help with various bits of work. In particular, my favourite German Dr. Sebastian Heeg for all things Raman spectroscopy, Dr. Zachary Coldrick and Dr. Matej Velicky for all things electrochemistry and Dr. Greg Auton for his endless optimism. I'd additionally like to thank Dr. Aravind Vijayaraghavan for his input along the way.

Nanofabrication is one of the most frustrating things I have ever encountered in my life, and I ~~hate~~ love all the clean room users for teaching me the skills necessary to make really small things. I'd also like to thank the NowNano group and IT 109 crew for joining me for coffee breaks, lunch, post work drinks etc etc.

Lastly, although not used extensively within this project, I'd like to thank ethanol, my favourite of the organic solvents.

1. Introduction

Since graphene was first isolated on a substrate and its properties measured in 2004 [1], a large number of possible applications for this new, two-dimensional carbon material have been suggested. An equally impressive number of superlatives have been used to describe its properties. The strongest [2] and most conductive [3] material ever discovered, impermeable to everything bigger than a proton [4], nearly transparent [5], high thermal conductivity [6]…

Amongst the proposed applications, sensors have received a lot of academic interest [7] as a number of graphene's properties lend themselves to sensor technology, including that the electronic properties of graphene are particularly sensitive to its surroundings and it is entirely made of up of surface atoms and therefore every atom can be in contact and interact with the sensing medium. The detection of single electrons transferred between a graphene surface and gas molecules was one of the first breakthrough studies with graphene [8], proving its potential as an electronic sensor. Amongst the research into optical [9], gas [8] and pressure sensors [10], electrochemical graphene sensors have received considerable interest [11–13]. Electrochemical sensors can detect changes in current, potential and capacitance at surfaces due to interaction with an analyte and therefore provide a range of measurement regimes. Electrochemical sensors can operate in the native aqueous solutions that all biological systems exist in and therefore have superior specificity in bio-sensing when compared to other techniques [14]. Improvements in sensitivity will always be sought until reliable detection at the ultimate single molecule limit is possible.

Advances in the medical and agricultural applications of sensing can have an important positive impact on healthcare outcomes and food sustainability in an ageing and growing world population, with this motivating the research undertaken for this thesis.

Reducing the size of sensors is favourable for applications requiring high spatial resolution or interfacing with micron scale objects, such as individual cells of living organisms. Electrochemical electrodes can be reduced in size to well below a micron [15,16], and in turn this creates some more advantages over larger scale macroscopic electrodes. Smaller electrodes produce smaller currents and therefore reduce voltage drops due to large resistances, the hemispherical diffusion of analytes toward a small electrode gives increased current densities and allows faster reactions to be detected and smaller electrodes have a reduced background capacitance [17].

Micron scale electrodes also have problems, largely due to fabrication difficulties. Many electrodes are insulated fine wires with a conducting tip exposed [18], however achieving a

precise geometry and surface roughness can be difficult. Using modern lithography techniques to create micro- or nano-meter electrodes is possible [15] but can also leave a lot of contamination from the fabrication steps and is technically difficult. Smaller electrodes also produce smaller currents, requiring more advanced measurement equipment to ensure sources of random electronic noise are not troublesome.

Graphene electrochemical sensors, amongst the breakthroughs, have also suffered from a number of drawbacks including variations in the quality of the source material, contamination issues and fabrication difficulties [19,20]. Central to these are the fact that due to graphenes sensitivity to the external environment, various factors have a strong effect on the way a device behaves. In particular, the substrate a graphene sample is placed on [21,22] and the substances it comes into contact with during processing [23,24] will both lead to often-unpredictable changes in measured properties. Polymers commonly used in fabrication also leave difficult to remove contamination [25]. All these factors need to be controlled if reliable sensing devices are desired.

Thesis objectives

There is plenty of scope for new research into graphene electrochemical sensing, however, some of the more fundamental issues need to be overcome before the research can develop. Therefore the prime aims and objectives of this thesis are to examine some of the key drawbacks outlined above:

- Fabricate a proof of concept micron scale graphene electrochemical device with a well-defined area, exposing the graphene to the fewest procedures possible whilst removing the effect of polymer contamination.
- Use high quality, single crystal graphene samples to remove the effect of crystal edges and defects.
- Use hexagonal boron nitride to reduce the interaction of graphene with its substrate.

The main challenge in this research is the fabrication, however this will then in turn allow the kinetics parameters of electron transfer at the electrolyte-graphene interface to be fundamentally investigated and compared previous studies. By doing this the relative impact of contamination and substrate can be considered for future research and fabrication methods using graphene.

2. Background and literature review

2.1 Electronic properties of graphene

Graphene is a true 2D material composed of a single layer of the sp^2 bonded carbon atoms arranged in the hexagonal, honeycomb lattice of graphite. A carbon atom has four valence electrons, with graphene three of these from the *2s*, $2p_x$ and $2p_y$ orbitals participate in planar, covalent *σ (sigma)* bonds with neighbouring carbon atoms. The bond angles are 120 ^{o} and the bond length is 1.42 Å. The fourth electron forms a *π (pi)* bond in the $2p_z$ orbital, perpendicular to the plane of the lattice and centred on each carbon atom. The *π* bonds from each carbon atom hybridise forming a π-π^* band. The electrons within the π-π^* band are responsible for the charge transport properties of graphene. For purposes of calculating the electronic band structure of graphene, the hexagonal lattice can be split into two distinct triangular sublattices (A and B), as each adjacent carbon atom has a geometrically reversed bond structure. All the atoms in the two sublattices have the same bonding arrangement when compared to each other, with an atom in sublattice A having three nearest neighbour atoms in sublattice B, and *vice versa*. The application of the tight binding approximation [26] to each sublattice yields a linear dispersion relation in momentum-energy space for the charge carriers in graphene at low energies (< 2 eV) [20,27,28]. A summary of graphenes lattice and band diagram is shown in Figure 2.1.1.

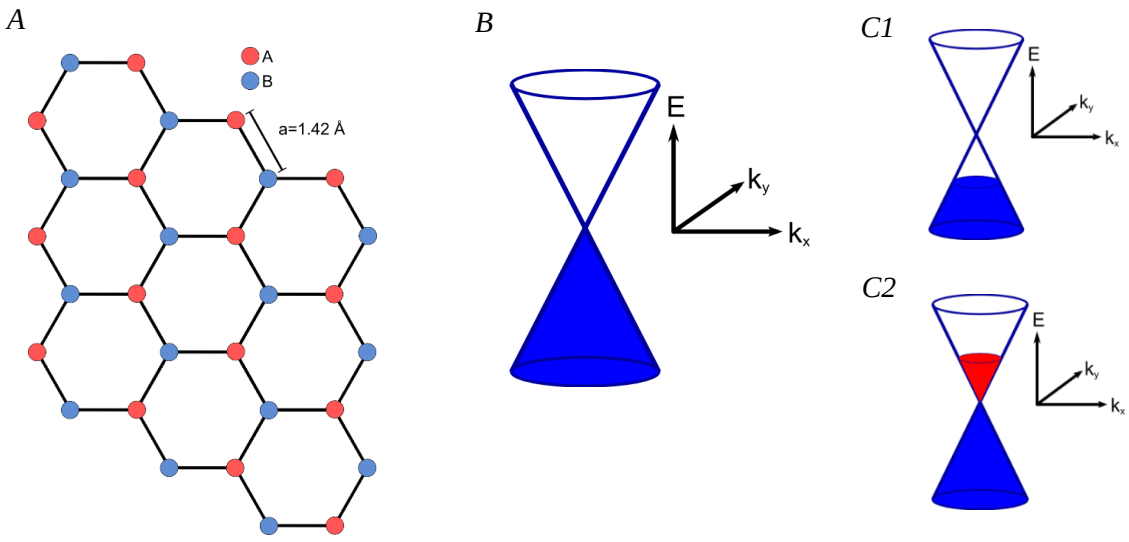

Figure 2.1.1 – Graphene lattice and dispersion relation

- *A- Diagram of the graphene lattice. Red circles denote the sublattice A and blue circles denote the sublattice B. a denotes the lattice spacing between carbon atoms.*
- *B- 'Dirac cone' band structure of graphene valence (blue filed) and conduction (white filled) bands at low energies in momentum-energy space.*
- *C- Shift in Fermi level due to (1) hole doping, increasing the density of hole conduction states and (2) electron doping, increasing the density of electron conduction states.*

The linear dispersion relation for charge transport in graphene leads to the 'Dirac cone' band structure, with this being responsible for many of the unique electronic properties observed in graphene. The valence and conduction bands have no bandgap between them, with the Fermi energy sitting at the point at which they meet, referred to as the '*Dirac point*' (DP). At this point the density of electronic states (DoS) is negligible and conductivity is at a minimum. The DoS in graphene is shown in Figure 2.1.2 as a function of energy. When doped, for example due to the application of an electric potential or charge transfer from an external molecule or lattice impurity, the fermi level moves, changing the density of states and therefore the free charge carrier concentration and conductivity. The position of the DP with respect to potential depends on the initial doping in the graphene, with impurities or defects shifting the DP away from 0 V [20]. Graphene has a far lower intrinsic charge carrier concentration than a typical metal (10^{12} vs 10^{22} cm^{-3}) [28,29] and therefore changes in the carrier concentration due to doping have a sizeable effect on the electronic transport properties of graphene. Another interesting feature of this band structure is the ability to alter the majority charge carrier from electrons to holes by passing the fermi level through the DP.

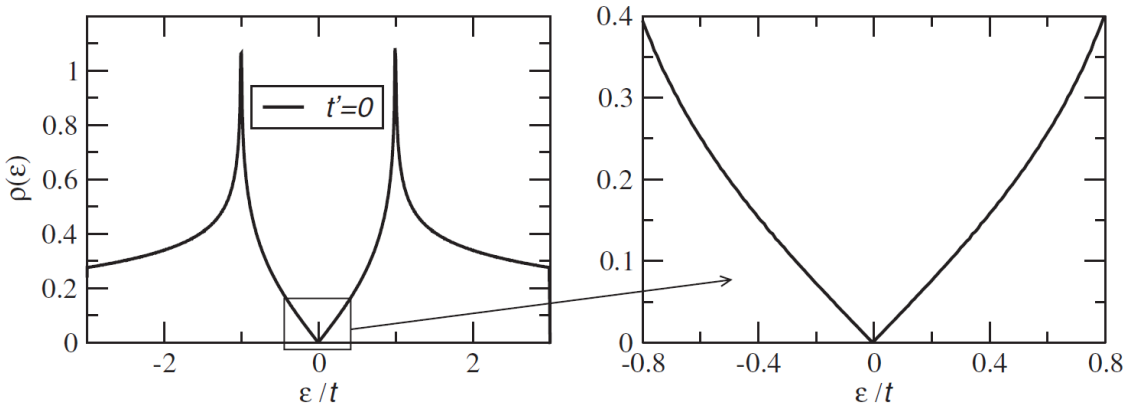

Figure 2.1.2 – Graphene density of electronic states

Density of states (ρ(ε)) per unit cell as a function of energy (ε) (in units of t), demonstrating the electron-hole nature of graphenes charge transport.

t is the nearest neighbour hopping energy between different sublattices (A & B) (=2.8 eV) and t' is the nearest neighbour hopping energy between the same sublattice. A zoom-in of the density of states at low energy is also shown, with this being the common regime for graphene experiments. If t'>0, the electron-hole symmetry is broken, and is not shown here for simplicity.

Image adapted from Reviews of Mod. Phys. 81 (2009) 109-162.

The charge carrier mobility in graphene surpasses most other conductors and is one of the highest ever measured. Values range from around 1000 to well over 200,000 $cm^2 \cdot V^{-1} \cdot s^{-1}$ depending on various factors such as substrate type, initial quality of graphene and temperature, with higher quality graphene and lower temperatures increasing mobility

[1,24,30,31]. The substrate effect is variable and depends on several factors [32,21], but suspended graphene (effectively no substrate) achieves the highest mobility [31,33]. The high mobility values give rise to a conductance surpassing all other known materials [22]. The combination of large charge carrier mobility and low charge carrier concentration make this material particularly sensitive to changes in its surrounding electronic environment, as changes in the carrier concentration are easily detected, and the high mobility means this can equate to large changes in the conductance.

The capacitance of graphene is quantum in nature due to the small DoS as compared to a metal or highly doped semi-conductor. The limited DoS leads to the effect that an electric field applied perpendicular to a graphene sheet is only partially screened, modifying the typical capacitance effects seen with conductors where an applied field is completely screened at the surface (penetration depth < 1 Å) [34,35]. This effect leads to the addition of an effective quantum capacitance in series with the classical geometric capacitance. The measured total capacitance (C_T) will be a reciprocal combination of the standard geometric capacitance (C_g) and the quantum capacitance (C_q) as shown in Equation 2.1.1 [36].

$$\frac{1}{C_T} = \frac{1}{C_q} + \frac{1}{C_g} \qquad (2.1.1)$$

It is clear from equation 1 that the smaller capacitance will dominate the measured total capacitance and therefore the ratio of the two contributions is important. For an electrochemical system, the C_g term is the equivalent of the ionic electrochemical double layer capacitance (C_{dl}) [37], discussed in more detail in Section 2.8. At potentials close to the DP, C_q varies with potential in a linear, V-shaped manner, with a theoretical minimum at the DP, with this minimum capacitance value increased when residual doping from charged impurities or temperature effects are present. The quantum capacitance increases with increased DoS, and therefore charge carrier density, either side of the DP [36,38–40], with the increased charge carriers increasing the screening of the applied electric field. The measured experimental values are typically < 10 μF.cm^{-2} over a potential range of ±0.5 V from the capacitance minimum at the DP [38,41]. Values for C_g in electrochemical systems are relatively potential independent at around 25 μF.cm^{-2}, therefore up to an order of magnitude larger than C_q [37,41]. As the potential on the graphene is increased either side of the DP, the measured capacitance increases from the C_q minimum, reaching a constant value that is dominated by the C_g term [36].

At higher potentials, when $C_q >> C_g$, a small change in potential will shift the entire band structure of the graphene by an amount eV_g, where V_g is the voltage drop across the dielectric

layer. This represents the classical case observed in metals. At potentials close to the DP, $C_q << C_g$ and a small change in potential shifts the fermi level by an amount eV_q where the V_q is the graphene potential [38,40,42]. In this region, the quantum capacitance effect dominates. Typical values of C_g and C_q show graphene sits in an intermediate area between the two limiting cases, complicating the analysis of graphene capacitance measurements [38,43]. The quantum capacitance is particularly useful for graphene sensor technology. The reduced capacitance gives smaller background parasitic signals, improving SNR, and allows the detection of small capacitance changes due to interaction with an analyte [44].

2.2 Graphene chemistry

Graphene is a relatively chemically inert material, undergoing very few permanent chemical reactions on its surface. This is partly due to the lack of 'dangling bonds', in that no covalent bonds need to be broken when creating a graphene surface from stacked graphene layers in graphite. Dangling bonds are very reactive as the surface seeks to reduce the excess energy produced when bonds are broken during the creation of a new surface. Secondly, graphenes low DoS means there are relatively few electrons available to undergo reactions when the transfer of an electron is required for a reaction to proceed, such as is the case with diazonium salt chemistry [45].

For the graphene surface (known as the basal plane) to react permanently, a sp^2 bond must be broken and a sp^3 type defect created. The π electron forms the bond, creating a tetrahedral bond structure that corrugates the graphene sheet into 3D. The loss of the π electron structure also leads to a reduction in conductivity, charge carrier mobility and changes the doping level of the graphene [46]. This defect can be the temporary addition of a chemisorbed molecule, where the bonding is weak and easily reversed, either spontaneously or by annealing [8,46,47]. Several ionic species have been observed to chemisorb to the graphene surface, causing reversible doping [48]. For stronger, permanent bonds the most amount of research has been into diazonium chemistry [49,50], adding phenyl groups to the surface that can then be subsequently functionalised with further reactions [51]. Plasma treatments can also be used to chemically alter the graphene lattice [47,52]. Graphene oxide (GO) [53] is the most commonly utilised form of chemically modified graphene. The formation of GO requires a reaction using a modified Hummers method [54], leaving the graphene surface decorated with several functional groups, with epoxide and hydroxyl being the main types. This creates a hydrophilic surface due to the presence of electronegative oxygen functionalities allowing dipole interactions with water molecules. These functionalities can be used in subsequent reactions to create a wide variety of graphene chemical composites [55,56]. This process can

also be partly reversed, creating partially oxidised graphene known as reduced graphene oxide (rGO) [53]. The large number of sp^3 defects created during oxidation means GO is insulating with poor electron mobility, with rGO moderately restoring the conductivity to that of pure graphene.

In contrast to the graphene basal plane, graphene edges are far more chemically reactive. The DoS at graphene edges is increased over the basal plane and therefore more electrons are able to participate in reactions [39,49]. There is also a difference in reactivity in the termination of the edge, with 'zig zag' (vertical edge in Figure 2.1.1) having higher reactivity than 'armchair' edges [48]. The role of edges is therefore important in any study of chemical reaction rates.

2.3 Graphene doping

The effect of doping in graphene samples, whether controlled or unwanted, is the subject of many research papers [32,57–59]. Doping can come from many sources, with the application of an electric gate field across a dielectric layer in a FET device being the most common way to control intentional doping. Figure 2.3.1 outlines this device geometry. The gate field will create a capacitance between the graphene and the gate electrode (usually doped Si), causing the band structure of the graphene to shift to higher or lower energy and therefore raising or lowering the fermi level with respect to the DP. As can be seen in Figures 2.1.1 & 2.3.1, this doping changes the majority carriers from electrons (positive gate field) to holes (negative gate field) as the band structure moves from lower to higher energy respectively. However, the initial position of the fermi level (at 0 V gate potential) within the band structure is influenced by the unwanted sources of doping in the graphene. A typical FET response of conductance against gate voltage is shown in Figure 2.3.1. The conductance minimum indicates the position of the DP. This is rarely at exactly 0 V gate potential, the theoretical position for pure intrinsic graphene. If it is shifted to more negative potentials then there is some residual electron doping in the graphene (referred to as n-type doping) or shifted to more positive potentials for residual hole doping (referred to as p-type doping) [57]. Adding electrons to the graphene shifts the fermi level up with respect to the DP as extra states are filled. The opposite case is true for hole doping, with electrons being removed and the fermi level lowering with respect to the DP. This can be due to several effects, with molecular and ionic contaminants being a common source.

Alkaline metals are good electron donors and therefore trace contamination can lead to excess electron doping in the graphene [48], and therefore a negative gate potential needs to be

applied to positively dope the graphene to shift the fermi level down to the DP. A source of p-type doping in graphene is gaseous nitrogen dioxide (NO_2) [58], where the electron withdrawing property of this molecule can be detected down to the limit of a single molecule in graphene FETs [8]. These sources of doping can be the simple transfer of an electron at the surface or the formation of a chemical bond, creating a sp^3 type defect. Another source of doping is lattice impurities such as boron and nitrogen [60], the method of doping traditionally used in the semi-conductor industry. The precise nature of the doping plays a role in whether the mobility and conductivity of the graphene are affected, with charged impurities and defects scattering electrons and reducing mobility [57].

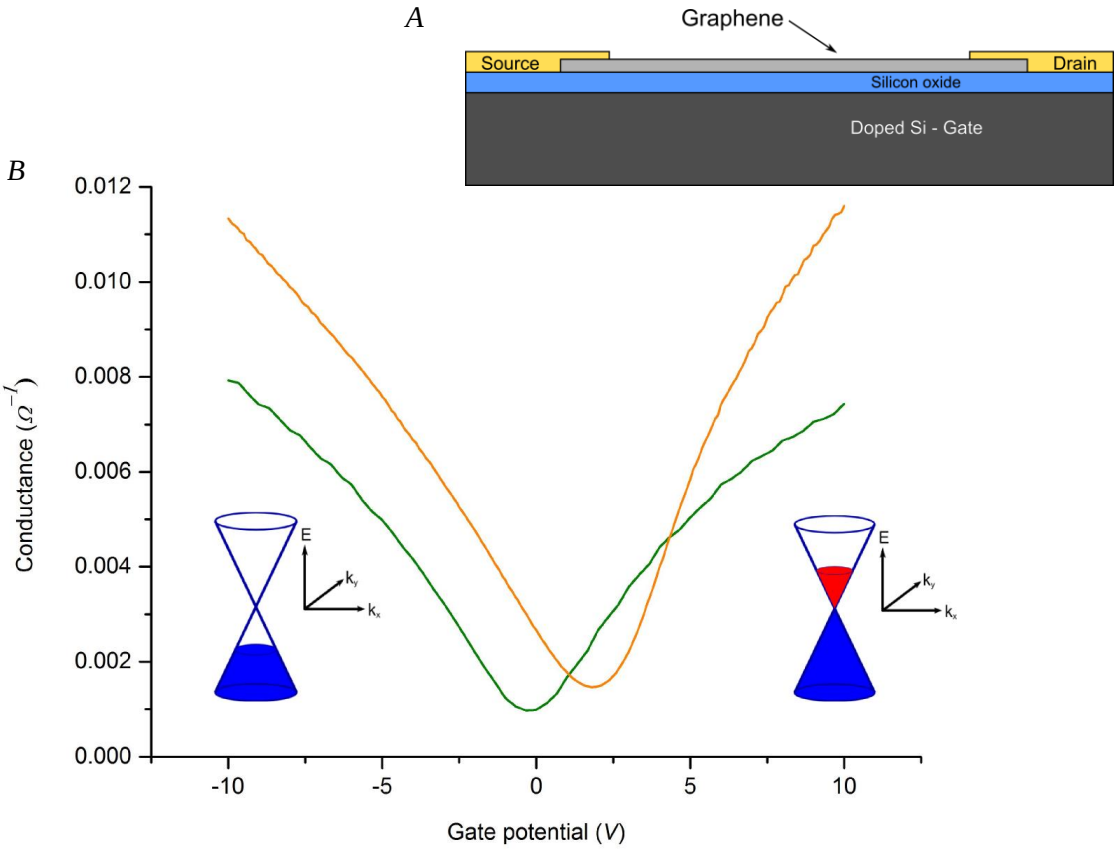

Figure 2.3.1 – Graphene FET response

A- Diagram of a typical graphene FET - a potential is applied between the source and drain contacts and the conductance of the graphene layer between them is measured. A gate potential is applied to the doped Si substrate, with the SiO_2 layer acting as a gate dielectric.

B- A comparison of conductance against gate potential of two different graphene FETs – as the gate potential drop is increased either side of the DP, the increased doping means more charge carriers are available for conduction.
The green trace shows slight initial n-type doping, whilst the orange trace shows p-type doping. Both sources of doping are unwanted and due to atmospheric and processing contamination.
The minimum conductance value on the orange trace is higher due to increased charge inhomogeneity in the graphene sheet, caused by charged impurities.
Data provided by and used with permission from Dr G.H Auton (Uni. of Manchester)

2.4 Contamination of graphene

The processing of graphene exposes it to several sources of contamination, which can all lead to unwanted doping effects. Most common sources are photon and electron beam lithography resists [61], solvents such as chloroform and acetone, transfer polymers such as PMMA and substrate etchants such as potassium hydroxide (KOH). Exposure to solvents has a variable effect, with research showing chloroform can both reduce [23] or increase [62] doping. The exact doping mechanisms are complex and poorly understood, with strain, substrate and surface morphology changes being important [62–65]. Overall, PMMA is used in the vast majority of graphene research both as electron beam lithography resist and transfer polymer to aid in physically manipulating graphene samples. The doping effects are relatively weak and the deposits easier to remove with PMMA compared to photolithography resist [66]. Acetone is most commonly used as a solvent to subsequently remove the PMMA and is not known to cause any significant doping [62], however polymer removal with solvents leaves a large amount of residue [67]. Acetone (along with other solvents) is known to effect electron transfer rates of an electrochemical redox reaction on HOPG surfaces, but the precise mechanism of this is unknown [68]. Annealing samples in an Ar or H_2/Ar atmosphere effects the doping level by further removing adsorbed residues. Most research suggests the removal of polymers via this method improves unwanted doping but the process can initiate chemical reactions that are detrimental to overall graphene quality [20,24,23]. Even with annealing, polymers adsorbed on the graphene surface cannot be removed completely, with the adhesion being partly physisorption and partly due to bonding with sp^3 defects [25]. Graphene cannot be cleaned via traditional methods such as plasma [46,47,52], UV/Ozone [69], H_20_2/H_2SO_4 (*Pirahna*) etches [70] and sonication [71] as they all lead to graphene damage. Methods avoiding exposure to solvents and in particular polymer contamination are ideal and increasingly being used [21,43,72–74].

Surface contamination is particularly troublesome with surface studies, such as AFM, STM and in particular electrochemistry. Surface residue from polymers will change the electron transfer characteristics and chemical interactions at the graphene-electrolyte interface. Therefore any fundamental results need to consider the effects of this carefully, which some research papers have addressed [39,75], with others clearly showing processing residue present on optical images [76]. Any electrochemical or gas sensor applications of graphene [8,77] need to ideally have atomically clean surfaces to both maximise the active graphene sensing area and to be sure that detection of electronic signals due to interaction with an analyte are not altered by unintentional interaction with surface contaminants. There have currently been no

studies that allow the processing of pristine, edge defect free graphene into devices for electrochemical sensor applications without introducing polymer or surfactant contamination.

Aside from processing contamination, graphene samples suffer from significant atmospheric contamination from exposure to ambient air conditions. Gas molecules such as H_2O and NO_x can easily adsorb to the graphene surface, altering the electronic and surface properties [8], but can be removed via annealing and vacuum measurements. This effect is seen when comparing the air and vacuum measurements of graphene FET devices [78]. Atmospheric hydrocarbons also easily adsorb to graphene surfaces, which can be seen in TEM images of graphene samples [79,80]. These hydrocarbons are thought to alter the measured hydrophobicity of graphene, with a pristine surface having a smaller water wetting angle when compared to atmosphere aged samples [81]. The timescale of this atmospheric adsorption is fast with effects seen in minutes and reaching saturation in around an hour, and therefore is unavoidable for most exposed graphene devices as sample preparation and measurement time is usually at least 24 hours or longer [39,75,82–85]. Any graphene sensor surface that requires atmospheric exposure will suffer from drawbacks due to this contamination. The effect of this contamination needs to be considered carefully when interpreting any measurements, however the chemical composition and specific structure (such as different adsorption mechanisms and chemical reactions) of atmospheric adsorbents is difficult to precisely quantify so their effect will be also [58,66,68].

2.5 Substrate effects

Substrate effects play a big role in graphene devices and limit the performance of graphene FETs, in particular the highest achievable charge carrier mobility. The main substrate induced effects are a result of surface roughness and charge inhomogeneity. Surface roughness reduces charge carrier mobility due to electron scattering at topological changes in graphene caused by the tendency of graphene to conform to the underlying substrate. It is also thought that corrugations and strain in graphene sheets alter the local DoS and therefore change the electronic properties in that region. Charge transport measurements using graphene FETs clearly show higher carrier mobility on samples with flatter substrates [21,24]. Chemical reactions are observed to be faster on rough substrates due to corrugations and strain [63,86].

Charge inhomogeneity results from charged impurities trapped on or near the surface of several substrate materials, in particular SiO_2. These charged impurities, such as substrate

defects or molecules such as water, can lead to the local accumulation of electrons or holes in a graphene sheet placed above, known as electron-hole 'puddles'. This leads to a local change in the DoS and DP with a characteristic spatial dimension of around 150 nm [87]. The charge density of these fluctuations is measured as 2×10^{11} to 2×10^{12} electrons.cm^{-2} [87–89]. For graphene FET measurements, the minimum conductivity value is determined by these charge fluctuations (see Figure 2.3.1). Although the DoS is negligible at the DP, the DP is different across a sample and therefore there will always be some charge carriers available for conduction at every gate voltage. These fluctuations are also important for graphene electron transfer chemistry, with substrates that induce lower charge fluctuation having lower chemical reactivity [45,49,90]. A locally varying DoS will allow a reaction to proceed at a faster rate when electron transfer is the rate limiting step, as more electrons will be available at the correct energy to participate in the reaction.

Graphene on SiO_2 and mica substrates shows poor electron transport [21] and high chemical reactivity [90]. Even though mica is atomically flat with reduced surface roughness effects, it has a high density of charged impurities [91]. Hydrophobic coatings on a substrate such at OTS or HMDS can help reduce the adsorption of charged molecules, provide electronic screening of charged impurities and prevent electron transfer between impurities and the graphene sheet [92,93]. Graphene deposited on these substrates has increased charge carrier mobility and lower chemical reactivity [32,45]. Hexagonal boron nitride (h-BN) has become the standard substrate for graphene devices where preservation of graphenes intrinsic electronic properties is required. h-BN is atomically flat and presents very few charged defects, making it the ideal substrate for graphene [24].

Hexagonal boron nitride has a lattice structure very similar to graphite. It has the same hexagonal 2D bond arrangement, with the carbon atoms replaced by alternating boron and nitrogen atoms. The layered 2D structure permits the separation of individual thin crystals down to the limit of a single monolayer. The h-BN lattice constant is ~1.8% larger than graphene and it is an insulator, with a direct band gap of 5.9 eV [94]. A summary of h-BN is shown in Figure 2.5.1.

When a monolayer of graphene is placed on a h-BN substrate they are held together by van der Waals (vdW) forces, with a binding energy of 10 meV per carbon atom [95–97]. Thin h-BN crystals lack any unpaired surface bonds and have a very low density of charged defects, presenting a pristine substrate for graphene to adhere to. This process helps to remove contamination from the interface between the graphene and the substrate, moving it into pockets of contamination that are clearly visible under TEM and DF optical microscopy [21,80].

In between the pockets of contamination graphenes electronic properties are preserved to a level only surpassed by suspended graphene sheets with no substrate interaction. This is due to the cleansing process both creating an atomically flat surface reducing charge carrier scattering due to topological inhomogeneity and removing charge defects that create inhomogeneous doping [21]. This vastly reduces substrate doping effects and increases charge carrier mobility by orders of magnitude [24].

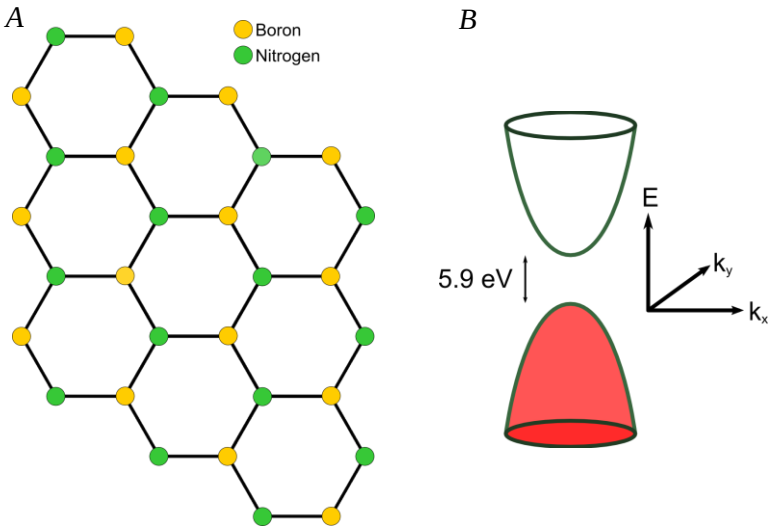

Figure 2.5.1 – h-BN

A – Lattice structure of a single h-BN 2D monolayer.

B – Band structure of h-BN. The filled valance band lies below the empty conduction band. A large band gap sits between them making h-BN an ideal insulator.

2.6 Graphene characterisation

Graphene was first identified via a combination of optical microscopy and AFM [1]. Optical identification of graphene, including the number of layers, is straight forward on the SiO_2 surface of a Si/SiO_2 substrate. A SiO_2 layer of ~100 nm or ~300 nm thickness is ideal for viewing graphene due to interference of light between the graphene and those approximate thicknesses of SiO_2 [5]. Other substrates produce a variable effect, with some such as 100 nm SiN_x producing very little optical contrast making viewing graphene very difficult [98]. DF optical microscopy highlights the edges of graphene flakes very clearly due to the increased photon scattering at the edges where the DoS is increased. This technique also shows up defects, contamination, bubbles and grain boundaries with sizes down to the resolution limit of optical light [21,99]. AFM can identify graphene flakes but the number of layers can be more difficult to deduce due to the limiting resolution of many AFMs. AFM is a useful tool for investigating the level of contamination on graphene, processing residue such as polymer resist shows up clearly on a graphene sample under AFM imaging. The AFM tip can then be used to clean areas of the graphene giving contamination free images [96,100].

Graphene has a very prominent Raman spectroscopy signal, from which several properties can be probed in a quick and non-destructive manner. Raman permits the quantification of

the number of layers and the level of strain and doping [101–103]. The spectrum is made up of 3 main peaks, the D, 2D and G peaks. The D peak sits at a wave shift of ∼1350cm^{-1} and requires a defect in the crystal lattice for activation. This means the D peak is a good probe for the level of defectiveness of the graphene, with its presence highlighting defects visible up to the laser and optic resolution (typically > 500 nm) [103]. The G and 2D peaks sit at a wave shift of ∼1580cm^{-1} and ∼2700cm^{-1} respectively. The ratio between the intensity of these peaks compared to their position gives an indication of the level of doping [104]. With low doping, the 2D peak is 3-5 times more intense than the G peak, however this depends on the laser wavelength used. Doping also upshifts and reduces the width of the G peak [102]. The effect of doping on the 2D peak is more subtle and due to charge transfer, with electron doping leading to a down shift and the opposite occurring for hole doping [105]. The shape of the 2D peak when excited with 514 nm laser indicates the number of layers, with a near perfect Lorentzian shape (with some Gaussian broadening) indicating monolayer. Two or more layers leads to noticeable distortion of this shape due to the appearance of extra peaks, with 10 layers or more being indistinguishable from graphite [101]. Graphene under strain shows distinct changes in the Raman spectrum [106]. The 2D and G peaks both show downshifts with increasing strain [107], also leading to a splitting of the G peak into two separate peaks (G^+ and G^-) that are polarisation sensitive and hence Raman can be used to determine the crystallographic orientation of a graphene sheet [108]. This downshift has been measured as 64, 10.8 and 31.7 cm^{-1} per % strain for the 2D, G^+ and G^- peaks respectively [108] and therefore is a sensitive way to measure strain in samples. The Raman spectrum is also altered when graphene is placed on an h-BN substrate. The G peak shows a small downshift and broadening, consistent with reduced substrate doping. The 2D peak shows more pronounced changes, with a small upshift and narrowing of the FWHM by ~8-9 cm^{-1} [109,110]. The excellent choice of h-BN as a substrate is also highlighted in Raman spectra, with the distribution of measured values over the surface being much narrower for h-BN when compared to SiO_2 [110].

Graphene can be imaged with different types of electron microscopy. TEM gives atomic resolution images of the graphene lattice, revealing the size, type and dynamics of nanoscopic defects that are always present on graphene samples [79]. Imaging graphene with SEM is also possible but will add deposits of carbon based contamination. This is due to interaction of trace hydrocarbon contamination with the electron beam and must be considered before imaging if contamination reduction is important [4].

2.7 Introduction to electrochemistry

Electrochemistry [111] is a branch of chemistry that studies the interaction between chemical and electrical systems. It covers a wide range of topics from corrosion and fuel cells to electrolyte based sensors and fundamental studies of physical chemistry, the latter two being the main topic of interest for this report. The basic electrochemical system concerns the reactions between an electrode surface and a chemical species in solution. There will be a transfer of electrons from (or to) a surface to (or from) a chemical species when two main criteria are satisfied: Firstly the surface and chemical species must be within a small enough distance of each other that an electron can travel between the two, with this distance typically being the order of a few nanometers. Secondly, there must be free energy levels available within the surface and chemical species to accommodate the moving electrons, outlined in Figure 2.7.1. Processes that involved the transfer of electrons and thus the generation of electric current are known as *faradaic.* The energy required for electrons to actually move across the solution-surface interface and the speed at which this occurs depends on a number of others factors [29]. Electrochemistry is a powerful technique as an electrode can change its surface potential and allow the continuous flow of electrons if an external circuit is connected to the system under study. This allows the study of the energetics and kinetics of these reactions under a variety of conditions to be closely investigated. For the vast majority of electrochemistry measurements this external circuit takes the form of a *potentiostat*, detailed in Section 2.12.

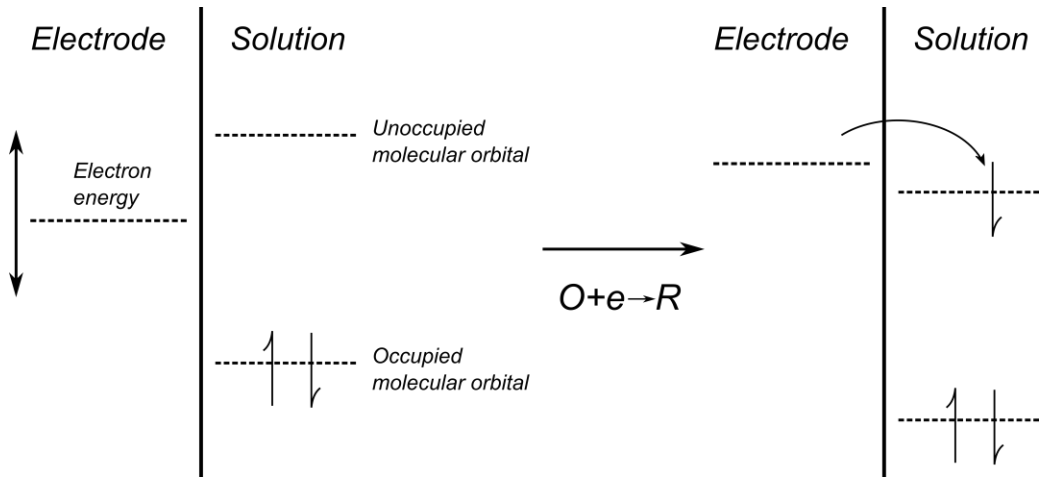

Figure 2.7.1 – Electrode reactions

A simplified diagram outlining the basic electronic structure of the electrode-solution interface. The left hand side illustrates the case where the electrode energy level sits between the occupied and unoccupied energy levels of a chemical species in solution. In this state no transfer of electrons occurs. The right hand side illustrates the case where the electrode energy has risen above the unoccupied molecular energy level barrier and an electron can travel from the electrode to the chemical species in solution, representing a reduction process.

2.8 The electrode-electrolyte interface

The electrode-electrolyte interface is an important aspect of electrochemical systems. When an object is surrounded by an electrolyte, a surface charge will build up due to the transfer of electrons from adsorbed molecular species and specifically adsorbed ions or processes such as protonation. This can take place spontaneously until the system reaches equilibrium [112]. A surface charge is also induced in conducting surfaces due to the application of an electric potential. This surface charge then causes the formation of an electrochemical double layer (EDL), where ions in solution of opposite charge to the surface potential are attracted towards the surface, screening the potential and creating a capacitance at the interface. A potential changing in time therefore creates a capacitive charging current, known as a *non-faradaic current.* In the case of polar solvents such as water, a layer of water molecules sits directly on the charged surface with the molecular electronic dipoles aligned against the surface electric field, causing a rapid drop of the potential in solution and acting as a dielectric layer. The exact structure of the EDL is complicated and subject to debate [37,112] and many effects can contribute to it. With graphene in particular, the fact the DoS changes with potential can cause important potential dependent structure and capacitance changes [113]. Figure 2.8.1 outlines the EDL structure suggested by the work of *H. V. Helmholtz, L. G. Gouy* and *D. L. Chapman* [37,112]. A key aspect of the EDL is that the electrode surface potential is reduced to the bulk solution value within a few nm of the surface. This means the transport mechanism for any charged molecules being studied in the bulk electrolyte is purely diffusion, assuming an excess of supporting electrolyte ions are present. Potassium chloride is commonly chosen as a supporting electrolyte as the K^+ and Cl^- ions are relatively inert at the potentials used in measurements and therefore do not contribute to chemical reactions at the electrode surface and only present as a capacitance charging signal in the measured current.

2.9 Electrode reaction kinetic theory

Full details of all the possible interactions at an electrode surface is detailed in *Electrochemical Methods* by *Allen J. Bard* and *Larry R. Faulkner* [37]. The following section summarises the key theory from this book that applies to this report.

The equilibrium state of a reversible redox reaction at an electrode, where an oxidised species reversibly accepts an electron to become reduced ($O + ne \rightleftharpoons R$), is described by the *Nernst equation*. This relates the bulk reactant concentrations to the electrode potential, and sets the fundamental conditions for a theory of electrode reaction kinetics.

$$E = E^{0'} + \frac{RT}{nF}\ln\frac{C_O}{C_R} \qquad (2.9.1)$$

Where E is the electrode potential, $E^{0'}$ is the formal potential for the reaction, R,T,F are the universal gas constant, temperature and Faraday constant respectively, n is the number of electrons transferred in the process and C_O and C_R are the reactant concentrations, with subscripts O and R denoting the oxidised and reduced species respectively. The formal potential for the reaction is the measured potential when the oxidised and reduced species are present in equal concentrations and the other components of the system (such as supporting electrolyte) are present in predetermined concentrations. As experimental conditions can vary between measurements, the formal potential for a reaction needs to be determined or estimated independently for the particular conditions used.

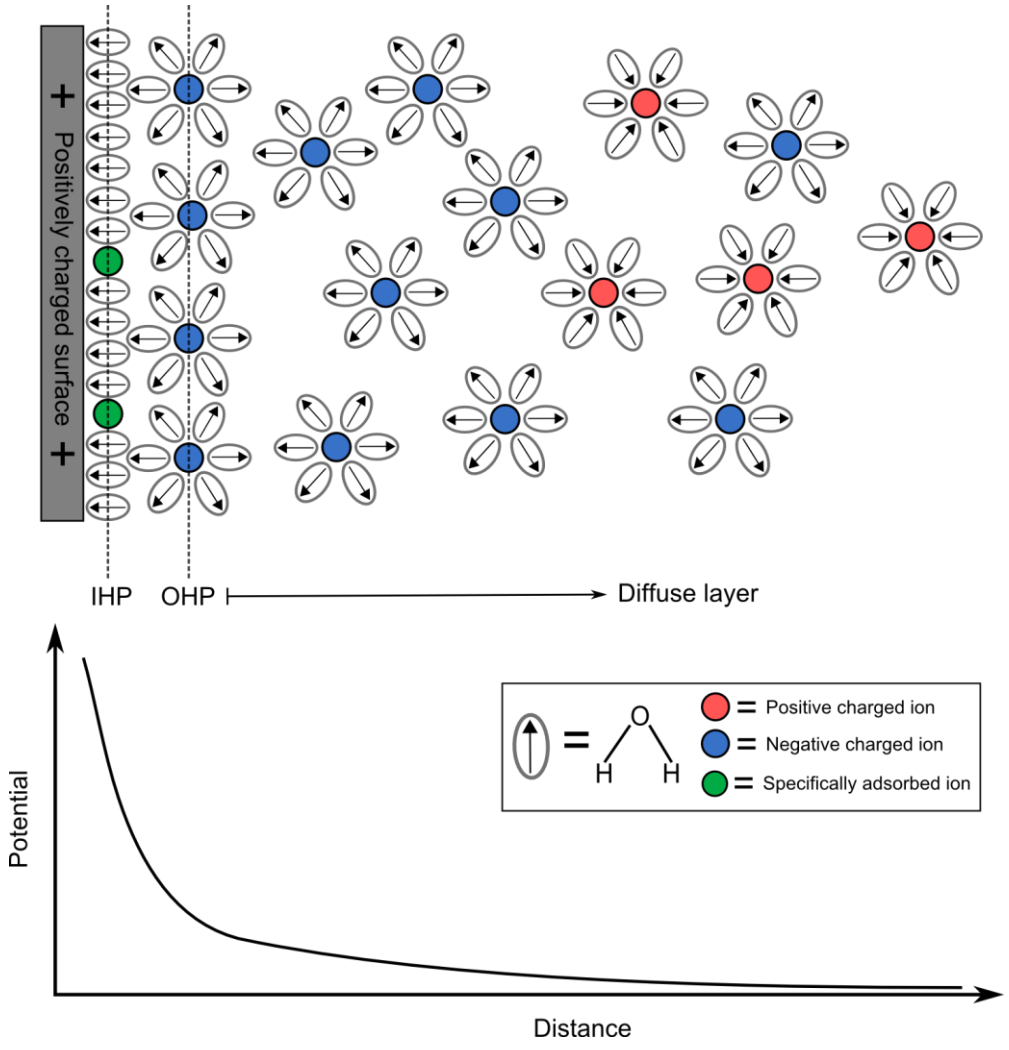

Figure 2.8.1 – The electrochemical double layer

A diagram of the EDL. The IHP is a line passing through the specifically adsorbed ions, the OHP is a line passing through the first row of solvated ions and the diffuse layer is the region beyond the OHP. The length scale of the distance is the order of a few nanometers, but depends on factors such as electrolyte strength.

The Nernst equation can also be expressed as a function of the chemical potentials of the system, where μ is the chemical potential and is equal to the difference in the required energy to take an electron from and donate an electron to the electrode surface. In other words, this is the energy difference between the forward and backward reactions of the reversible redox reaction.

$$\mu = \mu_0 + kT \ln \frac{C_O}{C_R} \qquad (2.9.2)$$

Where μ_0 the chemical potential at C_O=C_R and k is the Boltzmann constant.

The electrode current generated due to a faradaic redox reaction occurring with a surface can be incorporated into the theory by considering three more parameters, k_b, k_f and α. The parameters k_b and k_f denote the heterogeneous rate constants of the backwards and forwards reactions respectively, taking the units of distance per unit time ($cm.s^{-1}$). These parameters link the forward and backward reactions rates to the *surface* concentration of the reactants, C_O and C_R. Hence the cathodic (forwards) and anodic (backwards) current at the electrode can be expressed as,

$$i_c = k_f C_O(t).nFA \qquad (2.9.3)$$

$$i_a = k_b C_R(t).nFA \qquad (2.9.4)$$

Where i is the current with the subscript denoting cathodic (c) and anodic (a) components. A is a parameter known as the *frequency factor* and takes into account the number attempts required for a reaction to proceed over an energy barrier. As the reaction proceeds, the surface concentration of reactants can change and therefore must be expressed as a function of time, t. The total current at the electrode is therefore the sum of the currents due to the forward and backward components of the reaction.

$$i = i_c - i_a = nFA\left[k_f C_O(t) - k_b C_R(t)\right] \qquad (2.9.5)$$

As shown in Figure 2.7.1, electrode reactions are dependent on the electrode potential and the energy of the electrons in the reactants, denoted by E and $E^{0'}$ respectively. The heterogeneous rate constants change with electrode potential, with the forward reaction rate increasing as the difference between E and $E^{0'}$ becomes greater and the energy barrier is reduced. Figure 2.7.1 is simplified, and in reality the energy barriers are smooth functions and not instantaneous barriers, illustrated in Figure 2.9.1. Assuming a Maxwell-Boltzmann distribution of energies, reaction rate constants will depend on energy barrier height with an *Arrhenius form*, with the energy term in the form of a standard free energy,

$$k_f = A_f \exp\left(\frac{-\Delta G_c}{RT}\right) \quad (2.9.6)$$

$$k_b = A_b \exp\left(\frac{-\Delta G_a}{RT}\right) \quad (2.9.7)$$

Where ΔG_c and ΔG_a are the standard free energies of the energy barriers for the forward and backward reactions respectively. This can be related to the electrode potential and formal potential by including the parameter α, the *transfer coefficient*, shown in Figure 2.9.1.

$$\Delta G_a = \Delta G_{0a} - (1-\alpha)F(E - E^{0'}) \quad (2.9.8)$$

$$\Delta G_c = \Delta G_{0c} + \alpha F(E - E^{0'}) \quad (2.9.9)$$

Where ΔG_0 is the standard free energy of the barrier at $E^{0'}$, known as the *activation energy* of the reaction. Inserting the activation energy into expressions 2.9.6 and 2.9.7 gives,

$$k_f = A_f \exp\left(\frac{-\Delta G_{0c}}{RT}\right) \exp\left[-\frac{\alpha F}{RT}(E - E^{0'})\right] \quad (2.9.10)$$

$$k_b = A_b \exp\left(\frac{-\Delta G_{0a}}{RT}\right) \exp\left[\frac{(1-\alpha)F}{RT}(E - E^{0'})\right] \quad (2.9.11)$$

When the interface is at equilibrium and C_O=C_R, equation 2.9.1 shows that E=$E^{0'}$ and therefore k_b=k_f, meaning the forward and backward rate constants are equal at the potential $E^{0'}$. The heterogeneous rate constant in the special case where k_b=k_f is called the *standard rate constant*, k^0. In most real life experimental cases, the heterogeneous rate constants are affected not only by potential but other factors such as electrode contamination, oxide coatings and the electronic structure of the electrode. Therefore the standard rate constant is commonly used to compare the reaction kinetics between different electrode types and can vary by several orders of magnitude between experiments. It follows that k_b and k_f can be simply expressed as functions of this standard rate constant.

$$k_f = k^0 \exp\left[-\frac{\alpha F}{RT}(E - E^{0'})\right] \quad (2.9.12)$$

$$k_b = k^0 \exp\left[\frac{(1-\alpha)F}{RT}(E - E^{0'})\right] \quad (2.9.13)$$

Combining these expressions with current-concentration relation given in equation 2.9.5 gives the complete *current-potential relation* for a single electron redox process at an electrode surface.

$$i = FAk^0\left[C_O(t)\exp\left[-\frac{\alpha F}{RT}(E - E^{0'})\right] - C_R(t)\exp\left[\frac{(1-\alpha)F}{RT}(E - E^{0'})\right]\right] \quad (2.9.14)$$

This formulation is generally known as the *Butler-Volmer equations* and is widely used to describe heterogeneous electron transfer at an electrode.

The transfer coefficient, α can be constructed geometrically from the free energy-reaction coordinate graph in Figure 2.9.1(a). Considering the intersection between the $O+e$ and R energy curves, and the angles θ and φ, it can be shown that,

$$\alpha = \frac{\tan\theta}{\tan\theta+\tan\varphi} \qquad (2.9.15)$$

The transfer coefficient is an important parameter describing the symmetry of the free energy barrier of the reaction, taking a value between 0 and 1. Figure 2.9.1 represents this in terms of a *reaction coordinate,* representing the progression through a reaction taking into account the real coordinate system of the molecules/electrons and the rearrangement of various bonds required for the reaction to progress. This shows the free energy curves as being linear in the area of the intersection so any shift in potential will result in θ and φ being constant and therefore the transfer coefficient is independent of potential, which is an oversimplification. This is a good assumption for small potential perturbations where any curvature could be well approximated by a linear function. With most experimental data α is assumed a constant with the value 0.5, and generally a constant in the range of 0.3-0.7 when not [111]. If larger potential ranges are required for measurement (> 200 *mV*) then the curvature is likely to become more apparent and the assumption breaks down, as is demonstrated in Figure 2.9.1(b). The energy curve is non-linear over the energy range (ΔG_{0a} - ΔG_a) and when the moving from $E=E^{0'}$ to $E=E_1$, α will change with potential. Moreover, when considering an electrode material exhibiting large changes in the DoS over small potential ranges, such as with semi-conductors or graphene, it is possible this will also lead to changes in the free energy of the system. This unknown effect of large DoS changes on the shape of the free energy curve for the $O + e$ side of the reaction is not taken into account in the above theory.

2.10 Marcus-Gerischer theory

It is clear from Section 2.9 that for more complex systems the Butler-Volmer equations are no longer suitable and a more detailed model is required for treatment of electrode reaction kinetics. *R. A. Marcus* proposed a microscopic theory of electron transfer [114] which had further contributions from *H. Gerischer* [115] to allow a model for heterogeneous reaction kinetics at electrodes with more complex electronic properties. The model uses the overlap between the DoS of the reactants and electrode to predict the kinetics for a reaction [37]. In its general form, k_f and k_b can be expressed as,

A

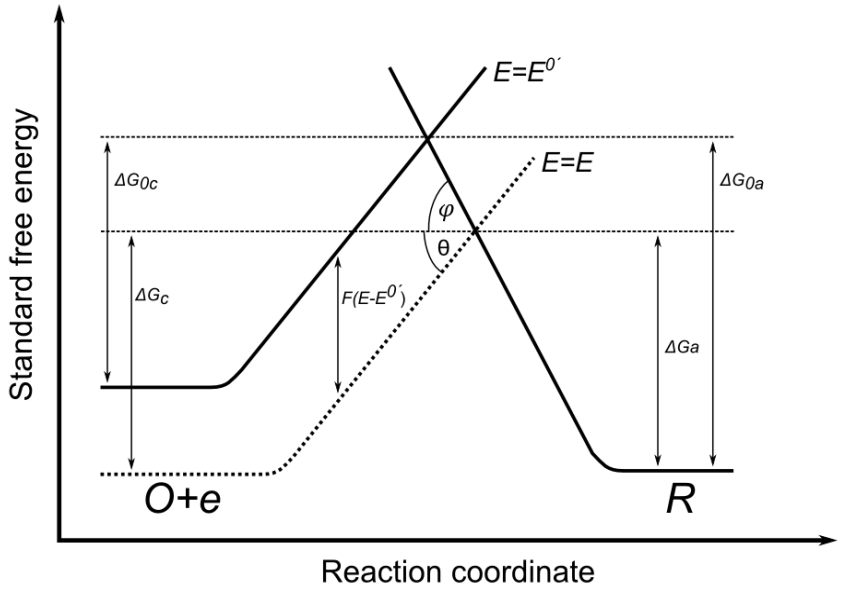

Figure 2.9.1 – Transfer coefficient

A – A diagram illustrating the effect of a potential shift from $E^{0'}$ to E on the free energy barrier of the reaction. The transfer coefficient is a function of angles θ and *φ and is constant assuming the free energy curves are linear in the region of intersection of O+e and R.*

B – The effect on the angles of intersection if the curves are non-linear. E_1 has the same shape as $E^{0'}$ but the angles change due to shifting to a different part of the slope.

B

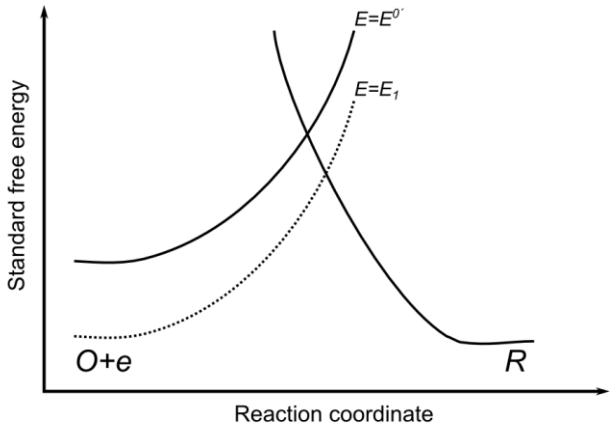

$$k_f = v\int_{-\infty}^{\infty} \varepsilon_{red}(E)W_O(\lambda,E)f(E)\rho(E)dE \quad (2.10.1)$$

$$k_b = v\int_{-\infty}^{\infty} \varepsilon_{ox}(E)W_R(\lambda,E)[1-(f(E))]\rho(E)dE \quad (2.10.2)$$

Where *v* is the nuclear frequency factor, similar to *A* in Section 2.9 and ε is a proportionality function with units of volume-energy (cm^3eV) with the subscript denoting reduction (*red*) and oxidation (*ox*). λ is a function of the equilibrium atomic configurations in O and R and is related to the standard free energy of the reaction. *f(E)* is the standard Fermi-Dirac function and the *W* term is the probability density function for the electrons in the redox species with subscript denoting the oxidised (*O*) and reduced *(R*) forms. It takes the unit energy^{-1} (eV^{-1}) and has a Gaussian distribution form,

$$W_O(\lambda, E) = (4\pi\lambda kT)^{-1/2} \exp\left[-\frac{(E-E^0-\lambda)^2}{4\lambda kT}\right] \qquad (2.10.3)$$

$$W_R(\lambda, E) = (4\pi\lambda kT)^{-1/2} \exp\left[-\frac{(E-E^0+\lambda)^2}{4\lambda kT}\right] \qquad (2.10.4)$$

The function *ρ(E)* is the DoS of the electrode. For graphene, the DoS (per unit cell) at low energies is given by [116],

$$\rho(E) = \frac{2A_C|E|}{\pi v_f^2} \qquad (2.10.5)$$

Where A_c is the unit cell area and v_f is the fermi velocity of electrons in graphene.

The general equation proposed by *Marcus* and *Gerischer* can take into account the quantum effects of band gaps in semi-conductors or the negligible DoS at the DP in graphene. The formula predicts that reaction rate is dependent on the DoS and should become negligible at the DP with a pristine graphene sample. However, to be successfully applied to graphene an accurate determination of the DP energy is required to take into account the linear trend to negligible DoS at this point. As explained in Section 2.3, the DP and DoS function can both significantly change with doping level and hence, although more accurate, implementing this model is difficult experimentally. Currently no reports exist of simultaneous determination of the electrochemical redox properties of graphene and it's DP.

2.11 Effect of concentration gradients

There are primarily two types of electrochemical electrode with respect to area, microscopic (ultra-microelectrode or UME) and macroscopic. The general definition of the UME is having at least one dimension smaller than 25 µm [37], which is key to observing the particular response this limited area electrode produces. To understand the response, the diffusion of the reactant in the electrolyte needs to be understood. As previously stated in Section 2.8, the only mechanism of transport for reactants in solutions with excess supporting electrolytes is diffusion, assuming the solution is unstirred and no convection is present. If a potential negative of $E^{0\prime}$ is applied to an electrode to cause a redox reaction to proceed in one direction, generally $O + ne \rightarrow R$, at a potential sufficiently negative the reaction will proceed at such as rate that the concentration of the reactant will become zero at the surface. This leads to a concentration gradient of the reactant from the bulk solution value to zero at the surface, with this layer referred to as the *diffusion layer*. When the electrode dimensions are small compared to that of the diffusion layer, as is the case with an UME, the diffusion layer has a hemispherical geometry. Understanding the behaviour in position and time of the diffusion layer is important to understand the measured response from an experiment.

Expression 2.9.14 gives the *current-potential relation* for an electrode, with the concentration expressed as a function of time and defined as being limited to the surface. To include the effects of diffusion, the concentration needs to be expressed as a function of position and time. For the case of a *flat, circular* disc shaped UME, expressing the position in a polar-spherical coordinate system, the reaction $O + ne \rightarrow R$ is subject to the following boundary conditions,

$$C_O(t) = C_O(r, z, t) \quad (2.11.1)$$

$$C_O(r, z, 0) = C_O^* \quad (2.11.2)$$

$$\lim_{r\to\infty} C_O(r, z, t) = C_O^* \quad (2.11.3)$$

$$\lim_{z\to\infty} C_O(r, z, t) = C_O^* \quad (2.11.4)$$

Where C_O^* denotes the bulk solution concentration. These conditions can then be applied to *Fick's second law* of diffusion, which describes diffusion along concentration gradients,

$$\frac{\partial C_O(r,z,t)}{\partial t} = D_O\left[\frac{\partial^2 C_O(r,z,t)}{\partial r^2} + \frac{1}{r}\frac{\partial C_O(r,z,t)}{\partial r} + \frac{\partial^2 C_O(r,z,t)}{\partial z^2}\right] \quad (2.11.5)$$

Where D_O is the diffusion constant. Another boundary condition can then be applied, given that no reaction can take place outside the area of the electrode. For the plane defined by z=0, for r greater than the electrode radius, r_0,

$$\left.\frac{\partial C_O(r,z,t)}{\partial z}\right|_{z=0} = 0 \quad (r > r_0) \quad (2.11.6)$$

The final boundary condition comes from the fact that at sufficiently negative potentials the concentration at the electrode surface will be zero, assuming the reaction has started (t>0),

$$C_O(r, 0, t) = 0 \quad (r \le r_0, t > 0) \quad (2.11.7)$$

The solutions to the inclusion of this position-time function of the concentration to the current-potential relation are non-trivial for these boundary conditions [17,117,118], however the key result can be summarised as,

$$i = (4nFD_0C_O^*r_0).f(E_e) = i_d.f(E_e) \quad (2.11.8)$$

Where $f(E_e)$ is a sigmoidal-like function describing the transition from zero current to the *steady-state* current, i_d. The steady-state limiting current is the point at which the measured current is limited by the diffusion of new reactants to the electrode surface, regardless of how negative the potential applied is, known as *steady-state behaviour*. In between these two limits the measured current is also affected by the kinetics of the reaction.

An empirical solution to this diffusion problem was discovered by *K. B. Oldham* and *C. G. Zoski*, that will predict the response of the function $f(E_e)$ to an accuracy of 0.3% [119] with the validity of the work studied in subsequent research [120,121]. Figure 2.11.1 shows the plot of this formula for different values of k^0. Assuming *quasi-reversibility* (Figure 2.11.1, b), that being the case when the reaction neither proceeds in a facile (reversible) nor very slow (irreversible) manner, so that the current is controlled by the kinetics of the reaction and the diffusion of reactants, the current-potential relation can be expressed as,

$$i = \left(\frac{i_d}{\vartheta}\right) \cdot \left[1 + \frac{\pi}{\tau\vartheta}\left[\frac{2\tau\vartheta+3\pi}{4\tau\vartheta+3\pi^2}\right]\right]^{-1} \quad (2.11.9)$$

Where ϑ and τ are functions of the potential, E,

$$\tau = \frac{\pi k^0 r_0}{4D_o} \exp\left[\frac{-\alpha nF}{RT}(E - E^{0\prime})\right] \quad (2.11.10)$$

$$\vartheta = 1 + \exp\left[\frac{nF}{RT}(E - E^{0\prime})\right] \quad (2.11.11)$$

This formula assumes *Butler-Volmer* kinetics apply, the electrode is a flat, circular disc and the diffusion constants are equal for both reactants and products. A further correction to this formula can be added if the electrode is recessed into the surrounding substrate. This has the effect of changing the limiting current and also the function $f(E_e)$ [122–124]. The effect on $f(E_e)$ is complicated, but its relevance to the experiment can be estimated by considering the rate of growth of the diffusion layer [125],

$$t_d \sim \frac{\delta^2}{D_o} \quad (2.11.12)$$

Where t_d is the timescale of measurement and δ is the thickness of the diffusion layer. If the recess is the order of 0.1 μm and D_o is 10^{-6} cm^2s^{-1}, then the diffusion layer will be larger than the recess in a time, $t_d \sim 10^{-5}$ s. This means any effects from a recess this size are unlikely to be noticed in normal experimental timescales.

The effect on the limiting current is given by the factor denoted I_c,

$$I_c = \frac{4L}{\pi r_0} + 1 \quad (2.11.13)$$

Where L is the depth of the recess. A distinction can be made between 'recessed' [122] and 'shallow recessed' [123,124], with this previously investigated by computer simulation. For a recess order of 0.1 μm and r_o =5 μm the correction is ~2.5% using the 'recessed' expression, and this differs by ~0.7% when compared to the 'shallow recess' simulation values. Given the simulation is only accurate to 0.25%, and it is expected other sources of error would be

much larger than this, the distinction between ‘recessed’ and ‘shallow recessed’ can be disregarded for all but the most accurate of experiments.

Furthermore, to take into account the limitations of a constant α discussed in Section 2.9, a linear function of α can be used to allow a first order approximation of how the parameter might change with potential [121], taking the form,

$$\alpha(E) = \beta E + \gamma \qquad (2.11.14)$$

Where β is the gradient of the linear function and γ gives the value of α at zero potential.

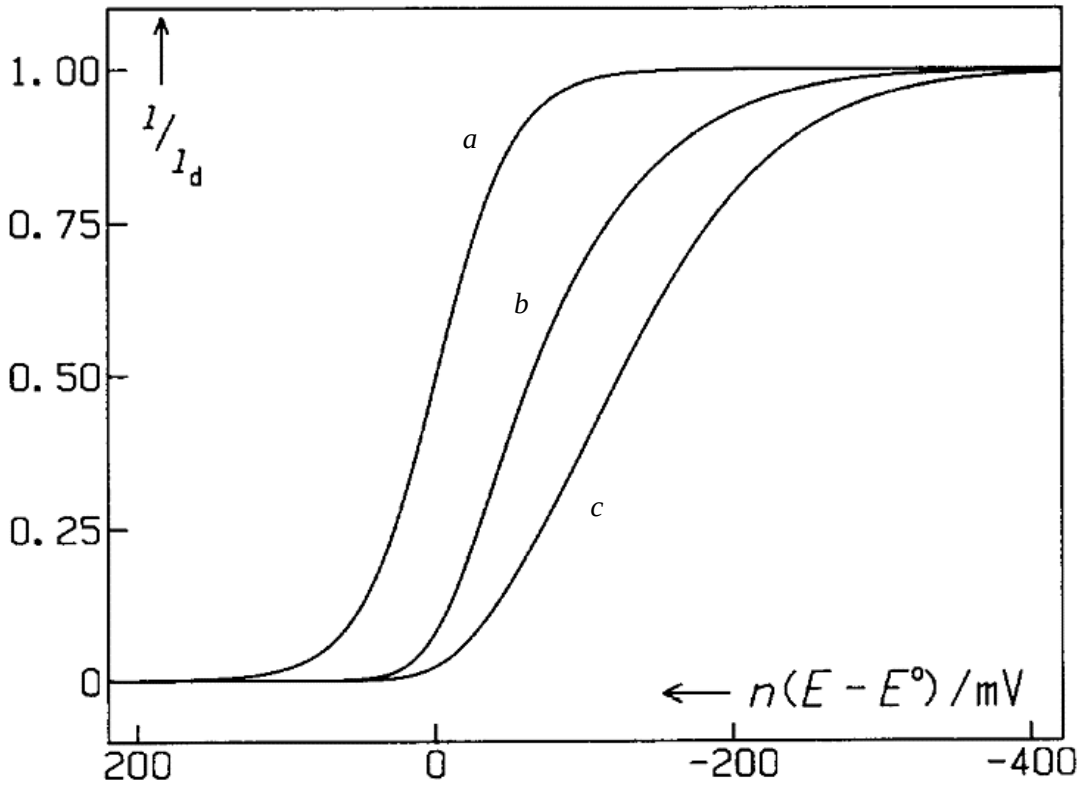

Figure 2.11.1 – Steady-state voltammetry

Plots of Equation 2.11.9 for different values of the standard rate constant, k^0. As k^0 reduces in magnitude, the curves become drawn out over a larger potential range.

$k^0 = \infty$ (a), 1.6 $D_0/\pi a$ (b), 0.4 $D_0/\pi a$ (c). $\alpha = 0.5$, $n = 1$, $T = 298.2$ K.

Figure adapted from J. Electroanal. Chem. 270 (1989) 79-101.

2.12 Principles of electrochemical measurements

The primary piece of equipment for electrochemical measurements is the *potentiostat*. This allows the use of three electrodes to perform measurements, a working electrode (WE), counter electrode (CE) and reference electrode (RE). The WE is the where the reactions of interest are occurring, such as a graphene electrode when studying this material. The CE

ensures there is a complete circuit for current flow and the potentiostat acts to ensure enough current flows through this electrode to maintain the set potential on the WE. Typically this electrode is an inert material such as Pt so it does not produce any electroactive species when current passes that could interfere with the reactions under study. The RE gives a potential reference to measure all other potentials from, therefore a potential on the WE is controlled with respect to the RE. This is important as without this, any potential measurement on the WE would be affected by the current flowing through it due to resistance induced voltage drop. The RE is usually chosen to be a material that has a well-defined potential that does not change with the passage of current, with *Ag/AgCl* being a common choice. *Ag/AgCl* refers to silver with a surface layer of its chloride. In aqueous solutions this RE undergoes the reversible redox reaction $AgCl(s) + e^- \rightleftharpoons Ag(s) + Cl^-$. This reaction occurs with fast kinetics, and hence low resistance, allowing the measured potential of this electrode to stay constant even if current is passed. All potential values in the expressions outlined in the previous sections ($E^{0'}$ and E) are measured against this reference potential. The potential of a RE still needs to be measured against some other common reference point (E^0) and no absolute 'zero' potential exist for electrochemical systems, so typically the reaction of hydrogen gas with platinum is used as zero, referred to as the *normal hydrogen electrode* (*NHE*). The potential of *Ag/AgCl* in saturated *KCl* electrolyte is 0.197 V vs *NHE*. If a different strength *KCl* solution is used then the potential is adjusted using equation 2.9.1.

There are many different techniques used in electrochemistry to perform measurements, with most applying a particular potential between the WE and CE and measuring the resultant current, referred to as a *voltammogram*. This voltammogram can then be analysed using equation 2.9.11 or similar to extract physical parameters. Cyclic voltammetry is a commonly used technique whereby the potential applied is changed in a linear manner with respect to time, cycling within a predetermined potential range. Here a key parameter is the scan rate, which can range from around 10 mV/s to 1 kV/s. The effect of increasing scan rate depends on the electrode size, due to the double later capacitance formed between the electrode surface and the supporting electrolyte. With larger, macroscopic electrodes, increasing the scan rate will increase this capacitance, which appears on a voltammogram as hysteresis between the forward and reverse scans. With microscopic electrodes, increasing the scan rate has relatively little effect on the observed response as the double layer capacitance is negligible. Obviously, when increasing the scan rate to extreme values, such as 100 or more V/s, the capacitance will be great enough to cause a response similar to that of macro-electrodes.

The diffusion of reactants to the electrode surface also needs to be considered alongside the scan rate. With a macro-electrode, the diffusion of reactants to the electrode surface can be approximated as a 2D linear surface, known a *semi-infinite linear diffusion*. At a certain scan rate, the diffusion of fresh reactants to the electrode surface will not be able to keep up with the changing potential and the current will reach a maximum, and as the potential increases further the current will begin to fall, as the reactant in the diffusion layer is used up. This leads to a 'peak' in the response for macro-electrodes. When the potential reaches its maximum point and reverses, the diffusion layer contains only the used reactant, and therefore the opposite reaction occurs, causing a peak in the opposite polarity. With microscopic electrodes, the diffusion layer is a 3D hemisphere, and this convergent diffusion leads to much greater mass transport and therefore a peak is not seen and a limiting current is reached as described in Section 2.11. When reversing the scan direction the increased mass transport means that fresh reactant is always available and therefore the voltammogram retraces itself, apart from a small capacitive hysteresis. When using microelectrodes the scan needs to be slow enough that the time scale to reach steady-state is much shorter than the timescale of the potential scan [125]. This can be expressed as,

$$R_s < \frac{RTD_o}{Fr_o{}^2} \qquad (2.12.1)$$

Where R_s is the scan rate of the measurement required to observe steady-state behaviour. If the scan rate greatly exceeds this limit then the diffusion of fresh redox species to the surface is not sufficient to keep up with the changing potential and peaks are seen in the response, rather than the sigmoidal shape describe by Equation 2.11.8. This peak type response is typical of larger macroscopic electrodes. Assuming R_s satisfies expression 2.12.1 then the scan rate should have little effect on the shape of the voltammogram.

The kinetics of a reaction will also change the shape of a cyclic voltammogram. When using a macro-electrode, slower kinetics will cause the oxidative and reductive peaks to move further apart. This can be expressed mathematically by the method developed by Nicholson [126], using the scan rate, v and a parameter, ψ,

$$\Psi = k^0 \frac{\alpha}{2} \sqrt{\frac{RT}{\pi n F D_{ov}}} \qquad (2.12.2)$$

Where all other symbols are as previously defined. This can then be related to the peak separation, ΔE_p, by the empirical formula,

$$\Psi = \frac{(-0.6288 + 0.0021 n \Delta E_p)}{(1 - 0.017 n \Delta E_p)} \qquad (2.12.3)$$

This method allows the kinetics to be calculated for systems where $\Delta E_p < 220$ mV. These equations show that for a particular system with a given k^0, increasing the scan rate also increases the peak separation. Therefore a plot of ψ against v can be used to calculate k^0.

For microelectrodes, the kinetic parameters are harder to derive from experimental data, however fitting the theoretical response, such as Equations 2.11.9-11 to experimental data allows the appropriate information to be collected. Increasingly slow kinetics will cause the sigmoidal micro-electrode response to become more drawn-out, requiring a larger voltage range to reach the steady state limiting current, as highlighted in Figure 2.11.1. This is analogous to the peaks becoming increasingly separated as with the macro-electrode response. Figure 2.12.1 outlines a comparison of the macro- and micro-electrode voltage-current response when using cyclic voltammetry.

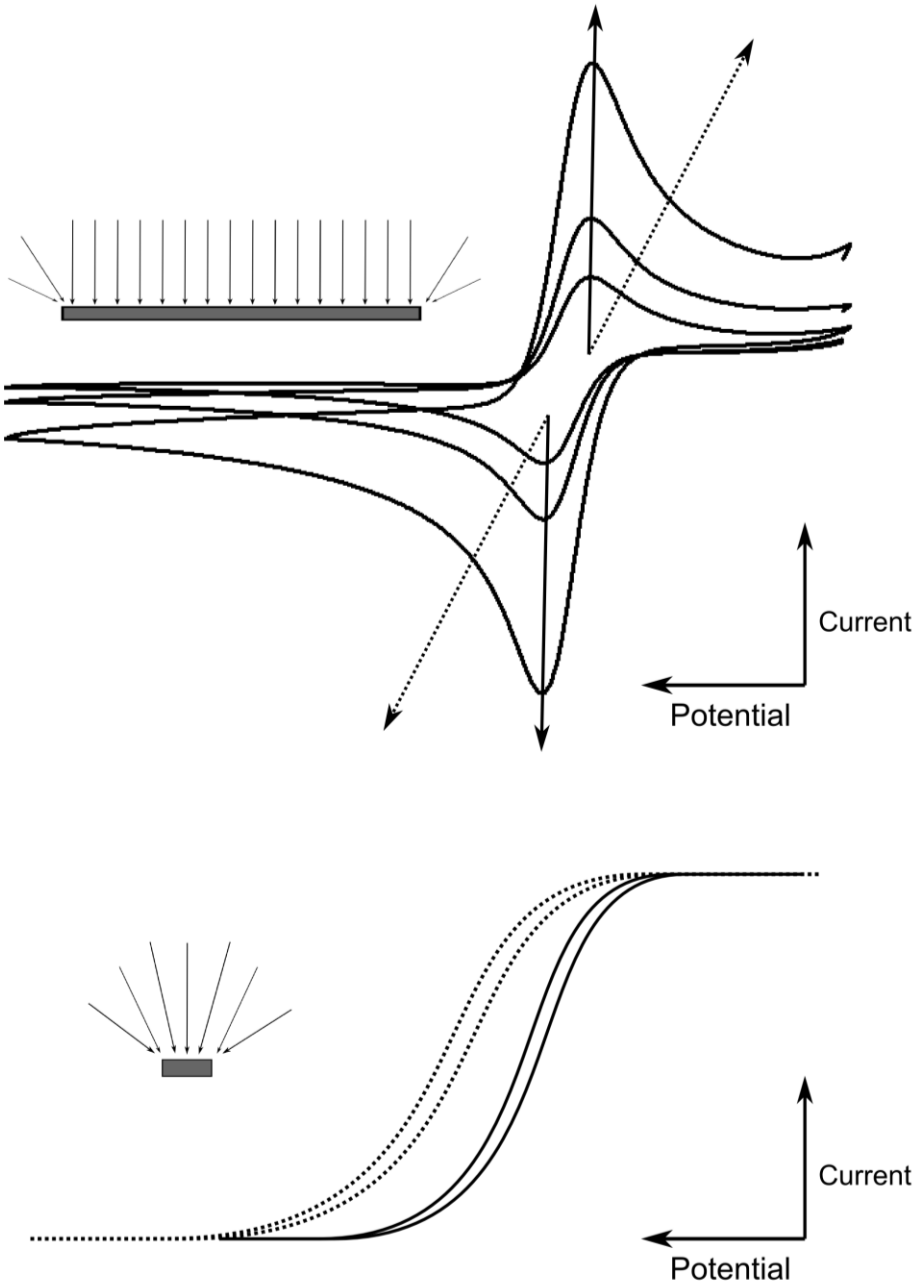

Figure 2.12.1 – Example CV scans for a macro- and micro- electrodes

The top figure demonstrates the expected response of a macroscopic electrode. Two peaks are present, for the reductive and oxidative processes. The solid arrow through the increasing peaks shows the change in response with increasing scan rate. The dashed line illustrates how these peaks would change if the kinetics of the reactions were slower, ie, decreasing k^0.

The bottom figure demonstrates the expected response of a microscopic electrode. Only a reductive or oxidative process is present. The dashed response shows the change in shape due to slower kinetics of the reaction, ie, decreasing k^0.

The insets illustrate the ion diffusion towards the electrode surface, with the larger electrode having linear, 2D diffusion and the smaller electrode having a hemispherical, 3D diffusion.

2.13 Redox mediators

The chemical species involved in redox reactions at an electrode surface are generally referred to as *redox mediators.* In many experiments the redox mediator is in the form of ligands bound to a central metal ion, known as a *coordination complex,* illustrated in Figure 2.13.1 [37]. The metal-ligand bond can range between covalent and ionic types and involve the transfer of electrons. The ligands are typically small molecules such NH_3 which stabilise the ion in the aqueous solution. During a redox reaction the ligands can change structure around the central metal ion, with the precise nature of this effect difficult to accurately include into theory [37]. However redox mediators can be separated in to two general types, *outer sphere* and *inner sphere*. Figure 2.13.1 illustrates the key differences between the two types. Outer sphere redox mediators do not need a direct physical contact with the electrode in order for the reaction to occur, with the reaction rate dependent on the overlap of the DoS as described by Marcus-Gerischer theory. The behaviour of this type is easier to understand and the measurements are affected less by difficult to control variables such as surface contamination and the chemical moieties of the electrode surface [37]. Inner sphere redox mediators require a direct contact to the electrode surface for electron transfer to occur, usually via a *bridging ligand.* This ultimately complicates the theory applied to the transfer and also makes measurements particularly sensitive to surface contamination and the chemical moieties of the electrode surface [37]. The bridging ligand may bind more strongly to some surface functional groups than others, aiding electron transfer and making results difficult to interpret unless these groups are carefully controlled [127].

Figure 2.13.1 – Electron transfer

An illustration of the electron transfer mechanism for outer sphere and inner sphere redox mediators for the reaction $O + e \rightarrow R$.

The outer sphere mediator in oxidised form accepts an electron to become reduced without needing direct contact to the electrode.

The inner sphere mediator requires electron transport through a bridging ligand for the reduction to occur.

The diagram also illustrates the change in ligand structure between the oxidised and reduced state.

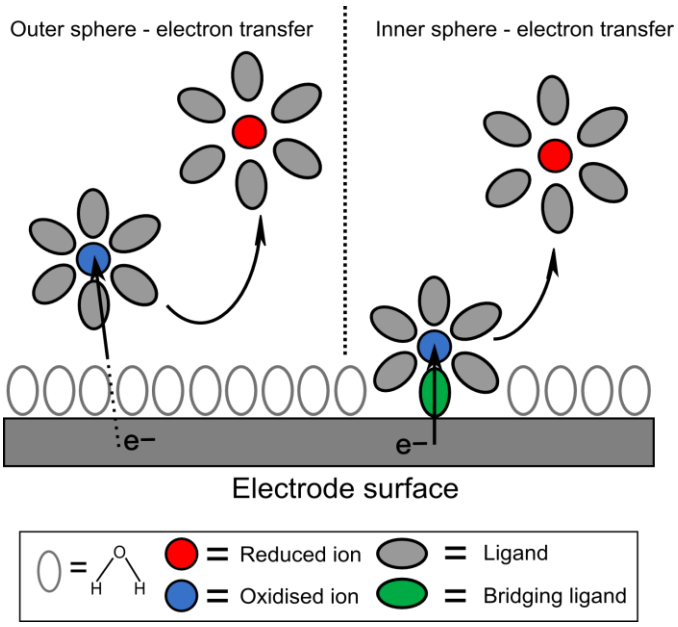

2.14 Graphene electrochemistry

Carbon materials have long been used in electrochemistry as working electrodes [128–131], largely due to carbons relative inertness, good conductivity and low cost. Carbon also has a wide *potential window*, where the potential window is the potential range over which the supporting electrolyte or electrode does not undergo any reactions, hence giving a flat background over which measurements can be made accurately. There are many different types of carbon electrode including glassy carbon, carbon paste and graphite. Graphite electrodes are divided into two types depending on the crystal orientation, basal plane and edge plane, frequently in the form of *highly orientated pyrolytic graphite* (HOPG). The distinction between these two types is important as they are thought to have different behaviour [131], however fabricating an electrode which is specifically one type can be difficult. Inevitably basal plane graphite will have some defects where some edge plane may be exposed, and *vice versa*. This is particularly problematic with larger electrodes where fabricating single crystals over mm^2 areas is difficult, with the individual crystal grains within a piece of HOPG having dimensions of around 1-10 μm [132]. Figure 2.14.1 highlights how a piece of HOPG may have both edge and basal planes sites and how precise masking would be required to isolate just one plane type. The difference between basal and edge plane graphite, and therefore similarly graphene, is thought to be due to the difference in the DoS of the two planes, with edges having a higher free electron density and this therefore facilitates faster electron transfer kinetics [133], as demonstrated in Figure 2.14.2. There are many studies that have compared the two [127,128,134,135] but disagreement still exist in the literature to the extent of the difference, with the experimental difficulty enhancing this issue.

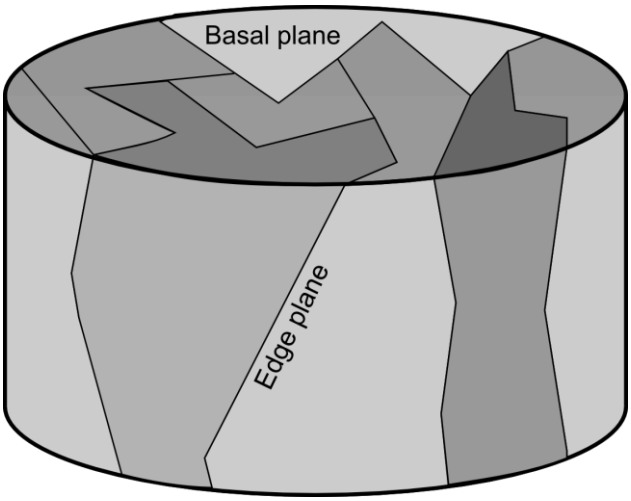

Figure 2.14.1 – HOPG

An illustration of a cylindrical piece of HOPG.

The top surface is basal plane. Different shaded regions indicate different crystal grains, within each the graphite has the same crystal orientation. This surface has the same structure as graphene basal plane, with many identical layers below.

The side surface is edge plane. Along this surface the edges of individual graphene sheets are exposed.

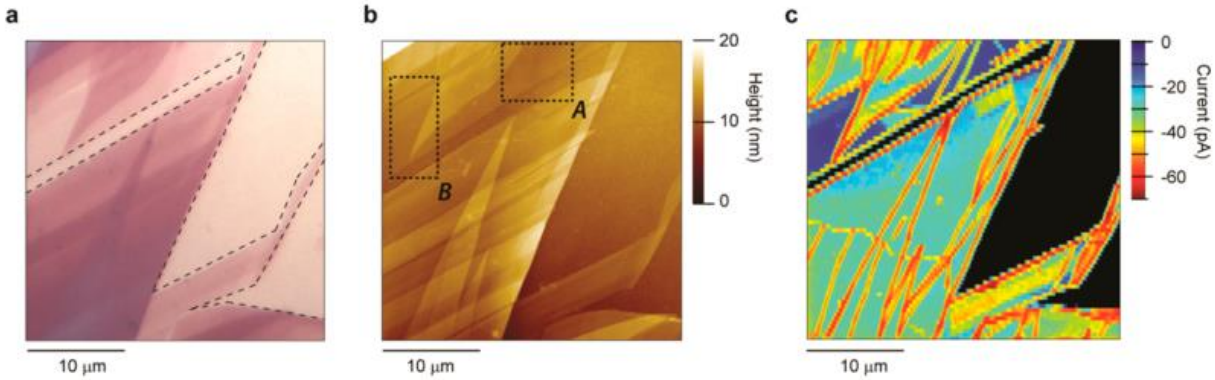

Figure 2.14.2 – Multi-microscopy of exfoliated graphene

(a) Optical microscopy image (dashed lines define the boundaries between the graphene sample and Si/SiO_2 substrate), (b) AFM topographical image, and (c) SECCM EC map for the reduction of $Ru(NH_3)_6^{3+}$ (5mM in 25mM KCl and phosphate buffer, pH = 7.2).

The increased current density is clearly visible at flake edges/boundaries, highlighted by the colour scale.

Image adapted from ACS Nano, 9(4) (2015) 3558-3571.

Graphene has been studied as an electrochemical electrode material to see if in the limit of a single atomic layer any advantages or differences exist over the commonly used HOPG, such as higher sensitivity due to different electronic structure or different electron transfer kinetics. As describe in Section 1, graphene has many interesting properties and how these transfer into electrochemical measurements is still not fully understood and there is plenty of scope for further research. However, the experimental issues arising from studies with HOPG are further compounded with graphene due to the difficulties in fabricating well defined and contamination free samples.

A particular subject of interest is how the heterogeneous reaction kinetics vary with the number of graphene layers. Some studies have found little effect of increasing number of layers up to the point where graphene is essentially graphite as shown in Figure 2.14.3 [75], however some studies have found increased kinetics with fewer layers [76,136]. Reasons for increased kinetics at fewer layers have been suggested as due to corrugations [136] and substrate effects [45] to more complicated mechanisms related to surface flake de-coupling in HOPG [39].

As discussed in Section 2.5, substrate choice has a clearly measurable effect on the electronic properties of graphene, however this has not been the subject of many studies with respect to the electrochemical properties of graphene [137–139] with most studies investigating substrate effects concentrating on non-electrochemical reactions [45,49,90]. Many studies use SiO_2

substrates, which will create considerable charge inhomogeneity [87] leading to enlarged electron transfer rates due to areas of increased electron and hole density [45], however no studies exist using a pristine, insulating, atomically flat substrate such as h-BN. The effect of the SiO_2 substrate is a likely factor in results concluding that the electron transfer rate decreases with increasing number of graphene layers [75,76,136]. Marcus-Gerischer theory suggests that increasing the number of graphene layers would increase electron transfer rates due to more layers having a higher DoS, but doping from the substrate can actually reverse this effect when only a single layer is measured [45]. For more than a single layer, the substrate doping effect is screened by the free electrons in the layer below [140]. When other substrates have been chosen there has been little research into the effect of surface roughness or graphene topology on measurements, with ripples thought to increase electron transfer rates [86,136]. Strain has been shown to increase chemical reactivity for reactions involving electron transfer due to the effect of strain on graphene doping [63].

Figure 2.14.3 – Transfer rate vs no. of layers

Heterogeneous electron transfer rate, k^0, between $IrCl_6^{2-}$ and mechanically exfoliated graphite flakes of varied thicknesses.

Little statistical change is seen with increasing layers.

Image adapted from ACS Nano, 8(10) (2014) 10089-10100.

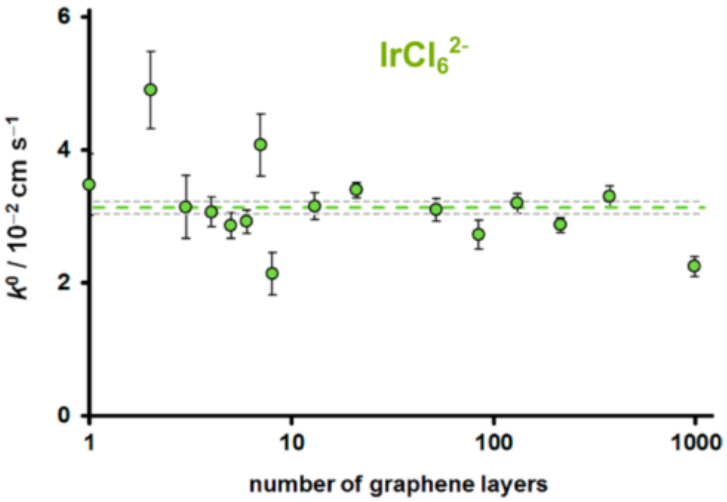

The graphene source material is also a variable between many studies, with researchers using chemical vapour deposition graphene (CVD) [13,139,141], graphene platelets from solvent dispersions [130,142,143] and mechanically exfoliated samples [39,75,76,136,144]. Furthermore, the distinction between graphene and r-GO is often not fully addressed in studies using r-GO as the graphene source [143,145]. All these types of graphene have variation in the number of defects, doping level, edge to basal plane ratio, grain size and contamination [20,146]. All these factors need to be controlled to build an accurate picture of how graphene behaves electrochemically, with mechanically exfoliated graphene thought to present the best quality samples for fundamental studies due to the lowest defect density, near intrinsic doping and low levels of contamination [7,20,33,147] (the preparation of mechanically exfoliated graphene is detailed in Chapter 3).

Contamination plays a role in the electrochemical response of graphene and HOPG. Atmospheric adsorption of hydrocarbons is a rapid process and therefore can only be studied using HOPG, where a freshly cleaved surface can be measured within minutes. Studies using this technique have shown vast increases in the electron transfer rate for freshly cleaved basal plane samples [75,85], however whether this is due to contamination, particularly with outer sphere redox mediators, is subject to debate [39]. Graphene can only be measured after significant exposure to the atmosphere due to preparation methods taking significant time (minimum several hours) and no studies of the electrochemical properties of graphene prepared entirely in a controlled glove box environment currently exist. Beyond atmospheric contamination, fabrication induced contamination has shown an effect on the measurement electron transfer rates. Polymers such as PMMA are commonly used in various aspects of graphene sample fabrication, and they are generally difficult to remove completely. These residues have been shown to effect the electron transfer rate by varying degrees [139,141,148]. Surfactants used to disperse graphene platelets have also been shown to effect the electron transfer rate [142]. Ideally, removing fabrication polymers and surfactants is ideal for electrochemical measurements [72,75].

It is thought that defects will increase the reaction rate of the basal plane (k^0 increases up to orders of magnitude) due to increased DoS at defects, with this effect extensively studied with HOPG electrodes [39,84,149]. It is thought that for outer sphere redox processes on both HOPG and graphene, the precise chemical functionalities on the surface have a limited effect on the reaction rate and the DoS and overall defect density (regardless of type) are the main contributing factors [127,149–151]. Furthermore, atmospheric contamination is only thought to have a small effect for outer sphere redox mediators on graphene and HOPG [39,85].

In summary, removing the effect of defects and crystal edges, substrate, surface topology and fabrication polymers, alongside using an outer sphere redox mediator on mechanically exfoliated graphene are a key way to probe the fundamental electrochemical properties of basal plane graphene and work towards the most accurate sensing surfaces.

3. Graphene device fabrication methods

The following chapter describes the various nano-fabrication techniques used for this project. The techniques are individually outlined in general terms, with the final section bringing them together to describe the fabrication of an electrochemical graphene device structure. All Sections up to and including 3.8 were carried out in class 1000 clean rooms.

3.1 Exfoliated 2D crystals

In general, materials can be described as 2D if two of the dimensions are much greater than the third. Single atomic monolayers represent the ultimate limit to this, however layered materials such as graphite can be prepared in sheets consisting of many individual monolayers but still be thin enough to be described as 2D. To fabricate devices or make measurements with 2D materials such as graphene, mechanically exfoliated samples (commonly and hereinafter referred to as *flakes*) present the best quality, giving single crystals with very few defects and little contamination. Single crystals of typical dimensions 100 x 100 μm^2 can be routinely made on SiO_2 coated silicon substrates (SiO_2/Si). Larger area samples acquired via CVD or solution processed methods have problematic defects, a large number of grain boundaries or contamination associated with them and are therefore best avoided for fundamental studies.

The following steps are summarised in Figure 3.1.1. Mechanically exfoliated graphene flakes were prepared using adhesive tape to cleave a thin layer of graphite from a high quality natural graphite sample (*Graphenium*, Graphit.de). The thickness of this initial layer was not important, but was generally less than 1 mm. The graphite adhered to the tape was then cleaved again with a clean area of the tape to create a two new thinner graphite layers, with this step repeated until a thin coating of graphite covered around 5 x 5 cm^2 area of the tape. The tape was inspected under a microscope to check that the graphite layer had many large, flat crystalline areas that were several times larger than the graphene required. With the graphite crystals face down, the tape was then pressed firmly on to a freshly cleaned SiO_2 surface of a SiO_2/Si wafer.

The cleaning protocol for the SiO_2/Si substrate was as follows: 10 minutes sonication in acetone, rinse with DI H_2O, 5 minutes sonication in IPA. The excess IPA was then blow dried with N_2 gas flow. The substrates were then placed in an oxygen plasma vacuum chamber, pumped down to a pressure of ~ $3x10^{-6}$ mbar. The substrates were exposed to an O_2/Ar plasma at a power of 10 W for 10 mins, leaving a clean SiO_2 surface. The tape with the graphite crystals was pressed on to this surface as rapidly as physically possible, usually

within seconds. The clean surface causes rapid build-up of hydrocarbon contamination, causing poor adhesion of the graphene if this is not avoided.

Once the tape was firmly adhered to the substrate it was left for at least 2 hours to allow good adhesion of the graphite crystals to the substrate surface. The tape was then removed using a MIBK bath at 80 ^{o}C, with the MIBK dissolving the adhesive on the tape. This step took variable time, but was clearly complete when the tape could be seen floating above the substrate and no longer adhered to it. A second 80 ^{o}C MIBK cleaning step for a further 5 mins removed most remaining adhesive residue. The sample was left in 80 ^{o}C IPA for 10 mins as a final cleaning step, with the IPA remaining on the sample surface gently removed with N_2 gas flow. The sample was then baked on a hot plate at 130 ^{o}C for 10-15 mins to improve the adhesion between the substrate and graphite. This process left the graphite flakes from the tape adhered to the SiO_2 surface. A new piece of adhesive tape was then pressed on to this surface and slowly peeled away, ensuring the angle between the tape and substrate was kept to a minimum as shown in Figure 3.1.1. This cleaved the graphite crystals, leaving behind a range of thicknesses down to a single monolayer on the substrate surface, identified via optical microscopy. h-BN flakes were prepared using an identical process to this, however with h-BN simply pressing adhesive tape coated with crystals on to a clean wafer and removing immediately sufficed if only thick (>10 nm) crystals were required. Example flakes prepared in this way are shown in Figure 3.2.3.

3.2 Flake substrate transfer

Samples of 2D materials can be transferred from one substrate to another with near micron precision. Flake transfer was required as the SiO_2/Si substrate routinely used to isolate single monolayers of graphene were not always best suited for making measurements due to the unwanted substrate effects described in Section 2.5. Furthermore, transferring flakes allowed the development of more complex device structures. When a 2D material is transferred on top of another 2D sample, together they are referred to as a *heterostructure*. The whole transfer process is summarised in Figures 3.2.1 and 3.2.2, illustrating the transfer of a h-BN substrate in order to fabricate a h-BN-graphene heterostructure.

Flake transfer was carried out by initially spin coating a thin PMMA layer on to the SiO_2/Si substrate containing the chosen flake to be transferred. The PMMA layer was around 500 nm thick, using 8% PMMA dissolved in anisole span for 1 min at 3000 rpm. The substrate was baked for 1 min at 130 ^{o}C to remove the excess solvent. The flake was then surrounded by a *transfer window*, a square of adhesive tape with an approx. 2 mm x 2 mm hole in the

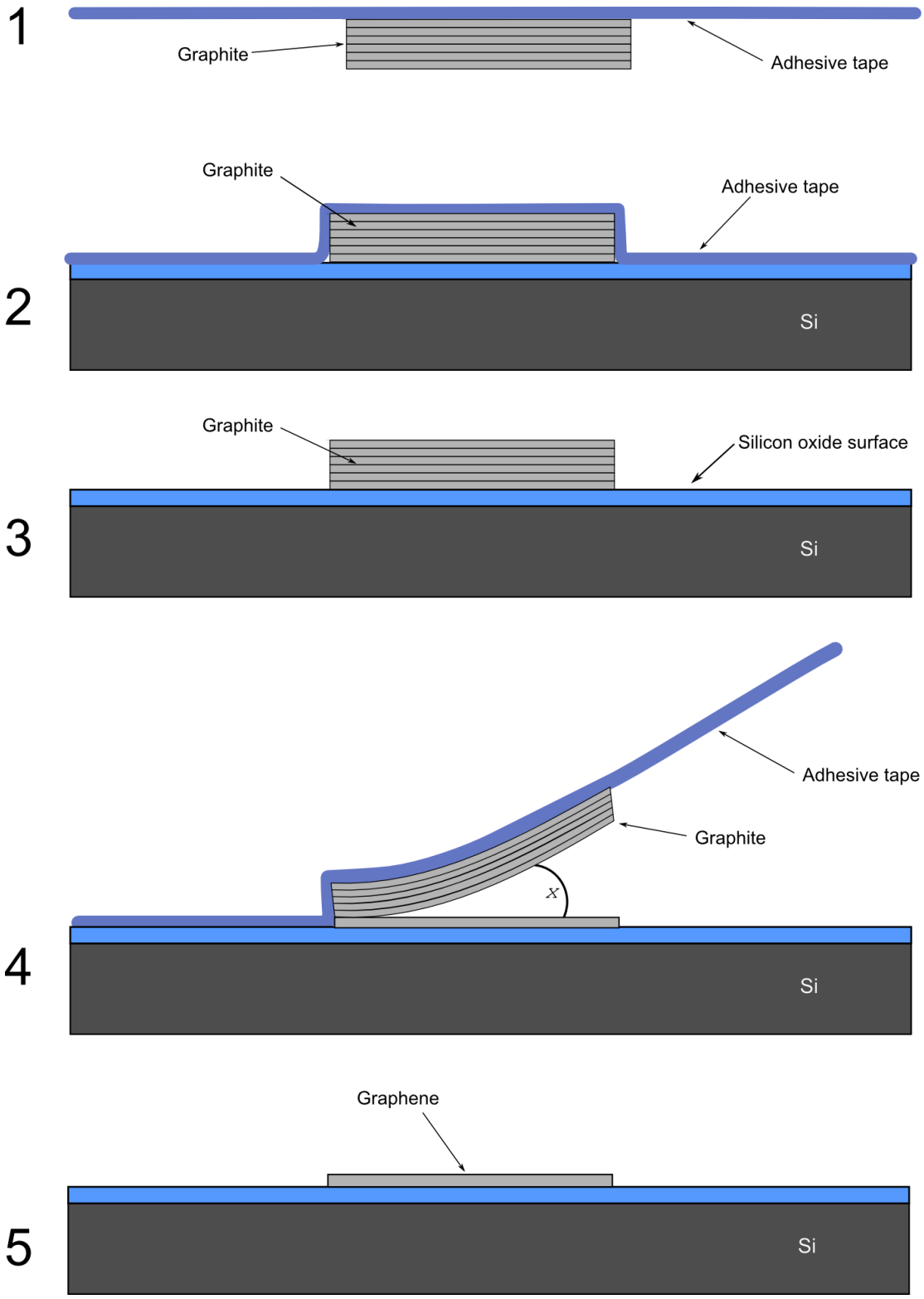

Figure 3.1.1 – Mechanically exfoliated flake preparation

1) Graphite crystals isolated on adhesive tape. 2) Tape and crystals pressed on and adhered to SiO_2 surface. 3) Graphite on surface after tape removal steps. 4) Graphite is cleaved into graphene with second piece of adhesive tape, during this step it was important to minimise the angle X. 5) Graphene monolayer isolated on SiO_2 surface.

centre. The tape was placed on the PMMA coated substrate, with the target flake for transfer in the centre of the hole in the tape. This process left the transfer window adhered to the top surface of the PMMA, with the graphene flake underneath the PMMA layer. A sharp tool was used to scratch away a thin line of PMMA around the outside edge of the transfer window, isolating the transfer window from the rest of the PMMA on the substrate. The substrate was then placed in dilute potassium hydroxide solution ($KOH_{(aq)}$, 3% w/v), wet etching the SiO_2 surface of the substrate. After around 4 hours, the SiO_2 was etched from underneath the target flake and PMMA layer, allowing the PMMA to detach from the substrate. The flake adheres to the PMMA layer during the etching process, so when the PMMA detached the graphene flake was removed with it. This left the transfer window floating on the surface of the KOH solution, with the PMMA layer adhered to the bottom tape surface. The hole in the tape contained a thin PMMA membrane with the target flake visible on the underside. This tape structure could then be removed from the KOH and placed in DI H_2O to remove any KOH residue. Two rinsing steps were used, the initial step required placing the entire tape structure in DI H_2O for 1 min, and then the tape window was left floating in fresh DI H_2O for around 12 hours.

The flake was then ready to be transferred to another substrate. The transfer window was removed from the DI H_2O and the excess water removed using a small absorbent fabric wipe, avoiding contact with the flake. It was then attached to a metal arm with adhesive tape. The metal arm had a fork on the end, with the fork having similar dimensions to the hole in the transfer window containing the PMMA membrane. The transfer window was aligned on the metal arm so that the target flake was in the centre of the fork. Once this had been prepared, the metal arm was attached to a micromanipulator stage and left for a further 5 mins to ensure any remaining DI H_2O had evaporated from the PMMA membrane.

The new substrate for the chosen flake was then placed below the metal arm, sitting on a temperature controlled stage that could be moved independently of the metal arm and also rotated by 360 °. An image of this '*transfer machine*' setup is shown in Figure 3.2.4. The substrate and PMMA membrane could be both viewed through an optical microscope looking vertically downwards. The metal arm was brought downwards towards the target substrate, with small position adjustments made on both the metal arm and substrate stage to keep the flake aligned with the correct area on the target substrate. The distance between the PMMA membrane and the substrate could be estimated by adjusting the focus of the microscope, and when both the PMMA membrane and substrate surface were just in focus at the same time the transfer was ready for the final step. As this point, the substrate stage

heater was set to around 80 ºC, with this temperature softening the PMMA membrane and allowing better adhesion to the substrate. The heat caused the PMMA membrane to relax slightly and move downwards, touching the new substrate surface and adhering to it. When the PMMA attaches to the new substrate surface the flake adheres with it. The PMMA around the flake was carefully scratched away with a sharp tool, isolating the flake from the transfer window. The transfer window was then removed and the new substrate was baked at 130 ºC for 15 mins to improve the adhesion of the flake to the new surface. The substrate was then left in acetone for 5 mins, repeated twice, to remove the PMMA layer, leaving the flake attached to the new substrate surface. This transfer process can be used for any 2D crystal assuming it is thinner than the PMMA membrane (<500 nm).

3.3 Optical lithography

Optical lithography uses a micro-manipulated laser and sample stage system to create micron scale patterns in a polymer on a surface. This was done using optical 'resists', photo-sensitive polymer compounds that change chemical structure when exposed to light of a particular wavelength. Lithography was used to create etch masks, a process to protect one area of a sample with polymer resist so another area can be exposed to etchants to create microscale features. A design was uploaded into the lithography system and the sample placed on the lithography system sample stage. A virtual coordinate system was defined on the sample using the microscope within the system, allowing the arbitrary design to be aligned to the appropriate area on the sample. To expose the sample, the micro-controlled stage was moved relatively to the laser and the laser intensity modulated to expose the areas on the substrate defined by the design to the laser for a pre-set amount of time.

The substrate needed to be spin-coated with a thin, ~ 500 nm layer of resist before exposure, with *Shipley S1805* used for this project. The resist was span at 5000 rpm for 1 minute, and the substrate was then subsequently baked on a hotplate at 110 ºC for 1 minute to remove the solvent.

After the laser exposure, the exposed pattern was then developed with the alkaline chemical developer TMAH to create the pattern in the resist, where the TMAH dissolves the resist that had been exposed to the laser light, leaving non-exposed areas unmodified.

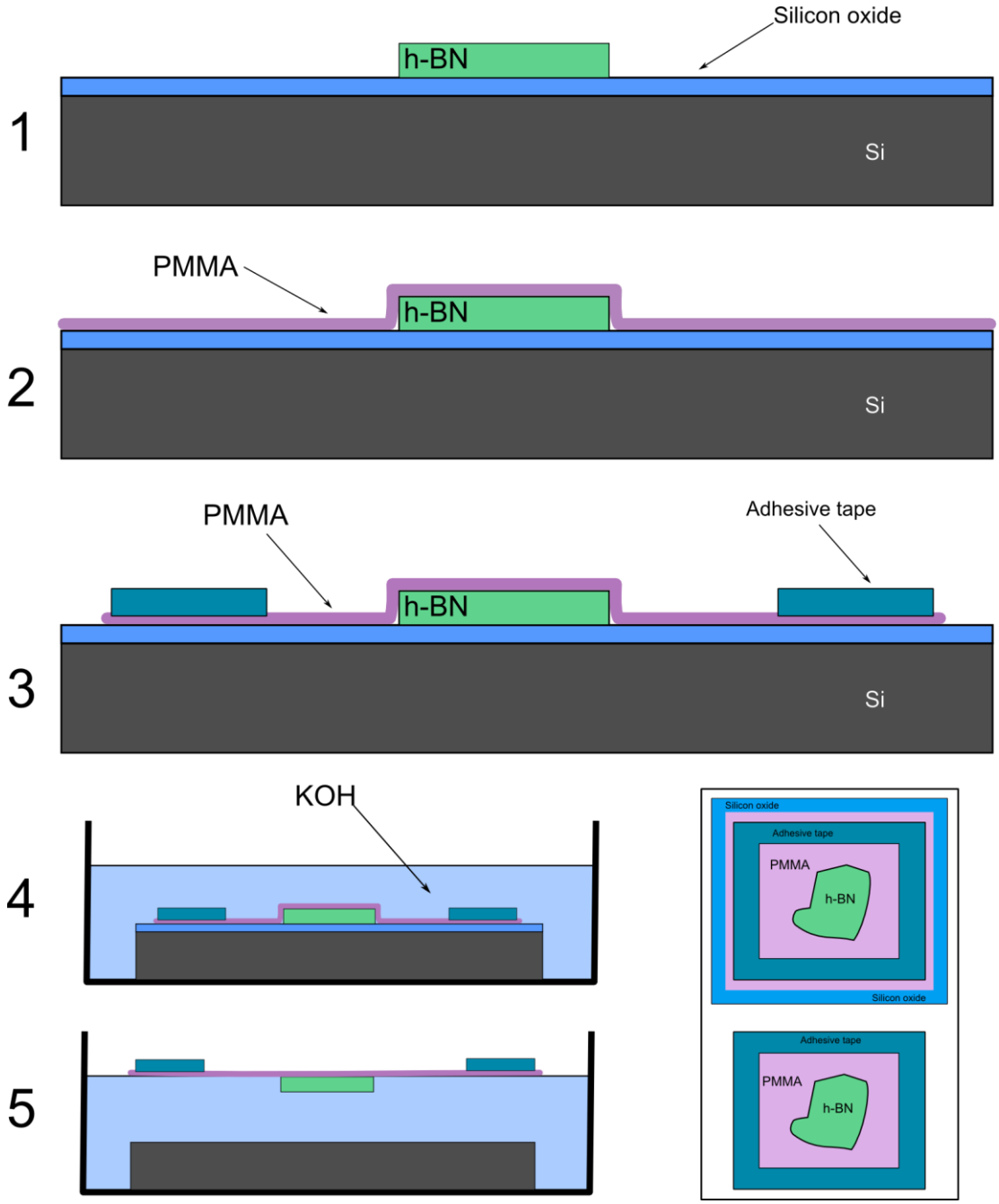

Figure 3.2.1 – Transfer preparation for a 2D crystal

1) h-BN flake chosen for transfer on a SiO_2 surface. 2) PMMA layer spin coated on to the substrate. 3) Adhesive tape 'transfer window' attached to substrate. 4) The substrate placed in KOH etchant. 5) The substrate with KOH etched away, leaving the transfer window with flake attached floating on the surface, and this is subsequently rinsed in DI H_2O. Inset (right of steps 4 and 5) shows transfer window and substrate from above, with the top image showing how the transfer window appears on the substrate and the bottom image showing how the transfer window appears when removed from the substrate.

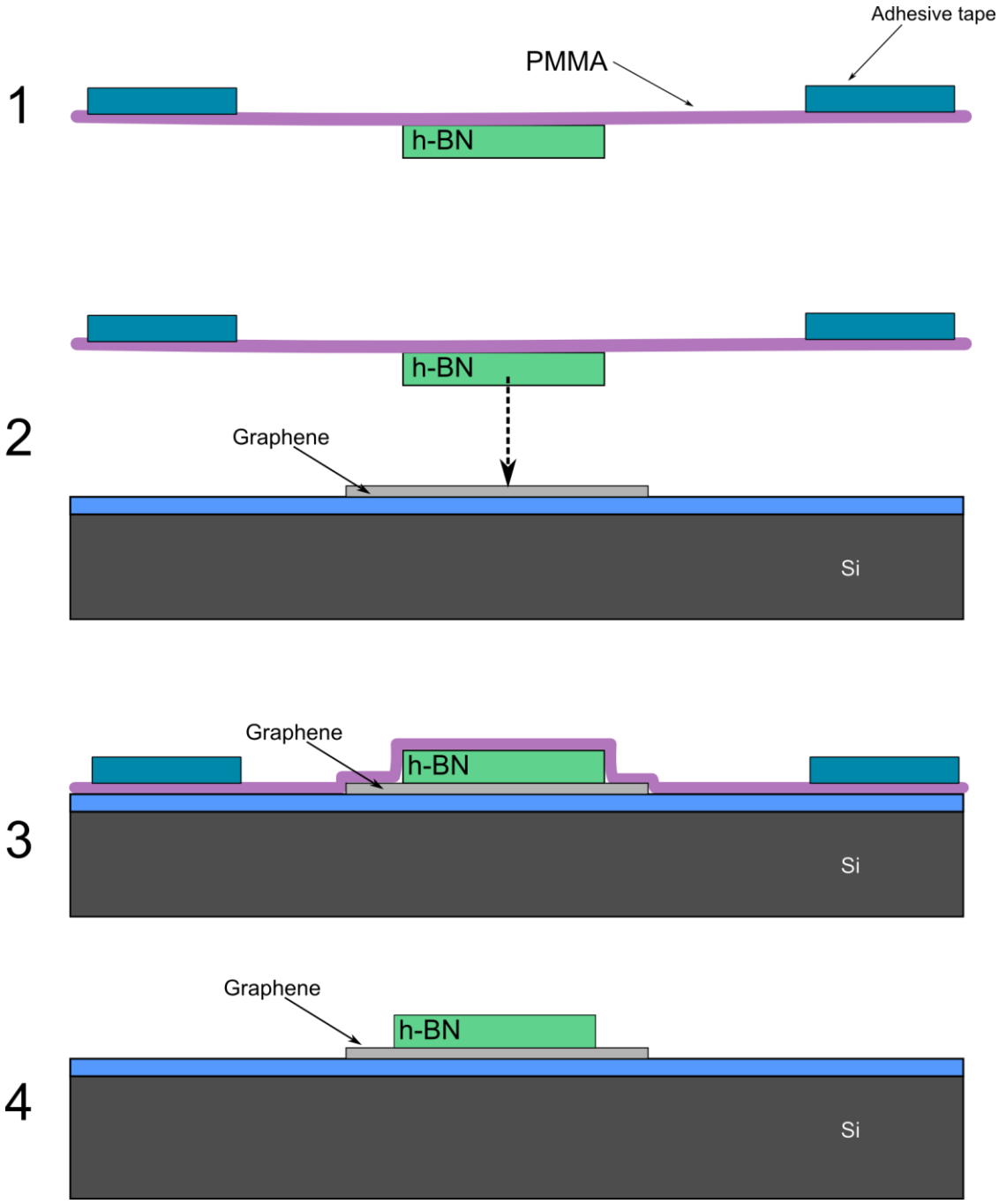

Figure 3.2.2 – Transfer alignment for a 2D heterostructure

1) Transfer window with PMMA membrane and flake attached. 2) The transfer window is attached from above to a metal arm controlled by a micromanipulator (not shown). The PMMA membrane and flake can then be aligned to and brought into contact with the target substrate. 3) The PMMA adheres to the target substrate. 4) The tape is removed and the PMMA is dissolved in acetone, leaving the flake attached in its new position.

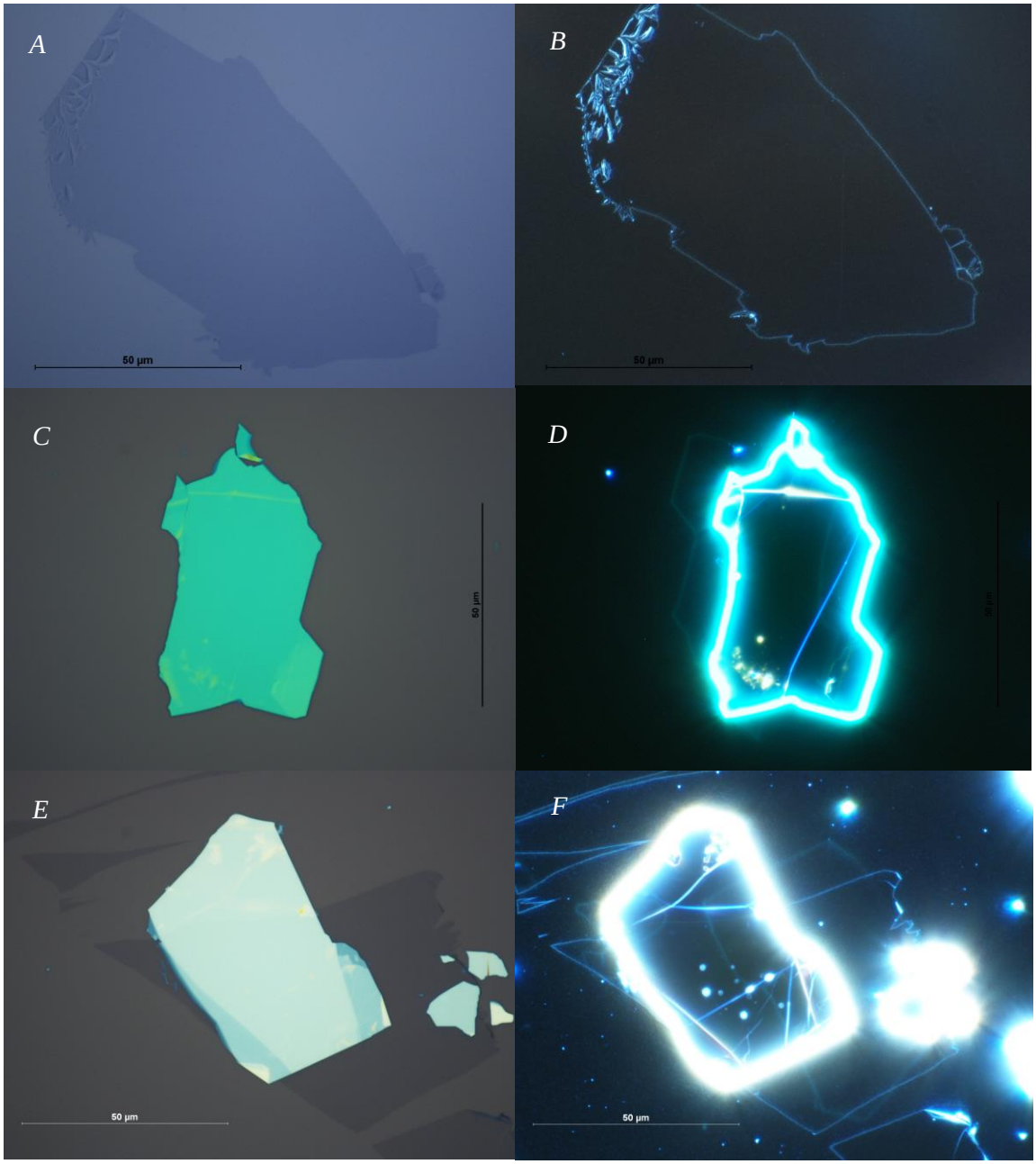

Figure 3.2.3 – Optical images of flakes

Optical images of 2D crystals. A – Mechanically exfoliated graphene flake on 90 nm SiO_2. B – DF image of A. C – Mechanically exfoliated h-BN sample (around 80 nm thick) on 90 nm SiO_2. D – DF image C. E – h-BN-graphene heterostructure after transfer of h-BN crystal on to target graphene flake. F- DF image of E. Dark field images highlight defects, edges and contamination.

3.4 Metal deposition

Metal deposition was used to make electrical contact to graphene samples. This was carried out in an electron beam evaporator. This used a vacuum chamber at a pressure of 10^{-8} mbar containing an electrode producing an accelerated electron beam focussed on to a target metal source. The electron energy was increased until sufficient enough to evaporate metal atoms causing them to travel radially outwards from the source. A sample was placed around 20 cm

from the source, with the sample surface tangential to the radial flow of metal atoms, allowing the metal to be deposited evenly on the surface. For this project, Ti and Au were used, with Ti acting as an adhesion layer and Au acting as an inert conduction layer. An adhesion layer was required as Au does not typically adhere to surfaces well by itself, due to its inherent inertness and crystal lattice mismatch with typical dielectric substrates. A 5 nm Ti layer chemically reacts with the surface it is evaporated onto causing strong adhesion. Around 100 nm of Au was then immediately evaporated on to this Ti layer, with the metal-metal interaction giving the Au far better adhesion to the clean metal surface than the sample surface. The thickness of metal deposited was monitored by a quartz crystal microbalance placed close to the metal source, where the change in resonant frequency was proportional to the weight of metal on the surface.

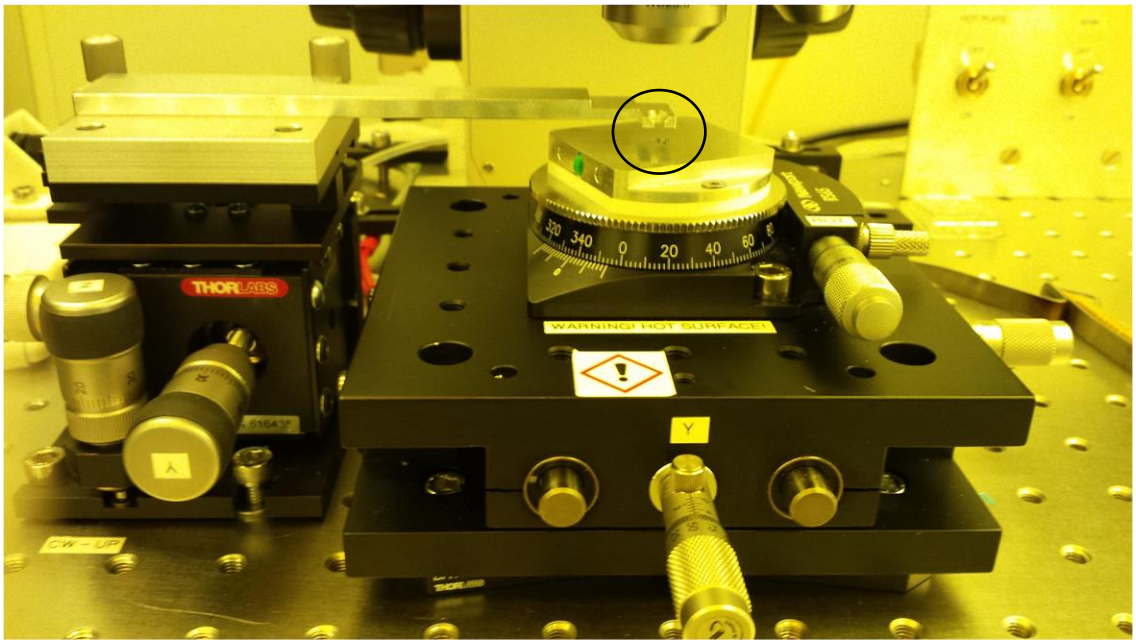

Figure 3.2.4 – Photograph of the transfer machine

The tape transfer window is attached to the bottom of the metal arm in the area circled. This can then be aligned using the screw controls to the left. The substrate stage sits directly below the arm and can be independently moved using the screw controls below the stage.

The microscope lens for viewing the transfer process is at the top-centre of the image.

(This apparatus was developed by Dr Peter Blake, Dr Andrey Kretinin and Dr Roman Gorbachev of the University of Manchester, UK.)

3.5 Dry etching of silicon nitride

Silicon nitride is used as a dielectric and can be grown or deposited as a thin layer on silicon wafers. In this form it is often referred to as SiN_x due to the imperfect chemical stoichiometry and crystalline structure of the thin films. As well as a dielectric layer it serves as a useful etch mask for nano-device fabrication, particularly for the wet etching of silicon, described in Section 3.6. To be used for Si etch masking purposes, the SiN_x needs to be etched into the appropriate pattern on the wafer surface.

For this project, SiN_x etching was carried out using reactive ion etching (RIE). RIE uses a chemically reactive plasma to selectively remove material from a surface [152], with optical resist acting as a mask to protect chosen areas of the sample from the plasma. Using optical lithography a pattern was created in 500 nm optical resist on one side of a clean double side SiN_x coated silicon wafer (SiN_x/Si/SiN_x), leaving the wafer surface with some areas protected by polymer resist and others exposed. The resist patterned sample was then placed into the vacuum chamber of the RIE apparatus. The apparatus exposed the sample to a CHF_3/SF_6 plasma for 2 minutes, with the highly reactive F ions chemically reacting with the exposed SiN_x surface and removing it. The products of this reaction are gaseous and can therefore be pumped away easily. The areas of the sample protected by resist were unaffected by this process, transferring the optically exposed lithography pattern into the SiN_x coating of the silicon wafer. Immediately after the CHF_3/SF_6 plasma, the sample was exposed to an O_2/Ar plasma for 2 minutes, removing the polymer resist. This O_2/Ar plasma step does not extensively react with Si or SiN_x and therefore does not affect the pattern made in the previous step. Figure 3.5.1 illustrates the dry etching of SiN_x.

3.6 Wet etching of silicon

Silicon can be etched in several alkaline solutions, with KOH solutions being used in this project. This etchant gives an anisotropic etch, selective to the different crystal planes of monocrystalline silicon. The etch ratios for the <111:110:100> crystal planes are approximately 1:600:400 [153]. If the wafer surface is terminated in the <100> plane then the etching will proceed to create a pyramidal or trapezoid shaped trench, as shown in Figure 3.5.1. KOH has a negligible etch rate on SiN_x and therefore a layer of SiN_x can be used to protect parts of the silicon that do not require etching. If the silicon wafer has a layer of SiN_x on both sides then etching the whole way through the silicon will leave a '*window'* of SiN_x remaining on the opposite side to that which the etch started, as demonstrated in Figure 3.5.1. If the initial opening of the SiN_x etch mask is too small, the etching will terminate as a

pyramidal pit, with the anisotropy preventing the etch progressing the entire way through a wafer. The geometry of the etching is easily calculated from the etch mask dimensions, wafer thickness and the angle θ (Figure 3.5.1).

To perform the etch, $KOH_{(aq)}$ at a concentration of 30% w/v was heated to 80 ^{o}C with an external water bath and thermometer controlling the temperature. The silicon substrate with RIE patterned SiN_x etch mask was placed in the solution, taking around 2 hours to etch through 300 µm of silicon. The end point of the etching is determined by visual inspection, when the silicon has been entirely etched through the wafer, the remaining SiN_x window becomes visible. Once complete the substrate was removed from the KOH solution and immediately rinsed in a stream of DI H_2O for 3 mins, and subsequently placed in a fresh beaker of DI H_2O for 12 hours to ensure no KOH deposits remained on the sample. An IPA rinse for 1 min followed by drying in a N_2 gas flow finished the etching process.

3.7 HMDS monolayer deposition

HMDS (hexamethyldisilazane) is routinely used in nanotechnology to create hydrophobic surfaces on silicon based materials. The HMDS molecule chemically reacts with hydroxyl (OH) groups on surfaces, grafting a monolayer of methyl (CH_3) groups from the HMDS molecule to the surface, as shown in Figure 3.7.1. Methyl groups are non-polar and therefore give the surface hydrophobic properties. When SiN_x surfaces are exposed to an oxygen plasma, the surface is functionalised with hydroxyl groups, which can in turn be exposed to vapour phase HMDS to allow the methyl grafting to occur.

For HMDS deposition, the SiN_x surface initially required treatment in O_2/Ar plasma using the same protocol as for substrate cleaning in Section 3.1. This left the surface terminated with hydroxyl groups. The substrate was then rapidly transferred to a large petri dish that had been flushed with N_2 gas prior to use. Moving the sample from the oxygen plasma treatment to the petri dish as fast as possible was important to ensure the surface was clean and the hydroxyl groups remained exposed on the surface. The petri dish then had a small vial containing ~100 µL of HMDS liquid added to it. The vial was placed on its side and was left unsealed, allowing the HMDS to evaporate and fill the petri dish. The lid of the petri dish containing both the substrate and HMDS filled vial was then sealed with plastic paraffin tape (*Parafilm*) to prevent the gaseous HMDS escaping. The petri dish was left for at least 4 hours at room temperature to allow the reaction to proceed. After this time the substrates were removed and were ready for further processing.

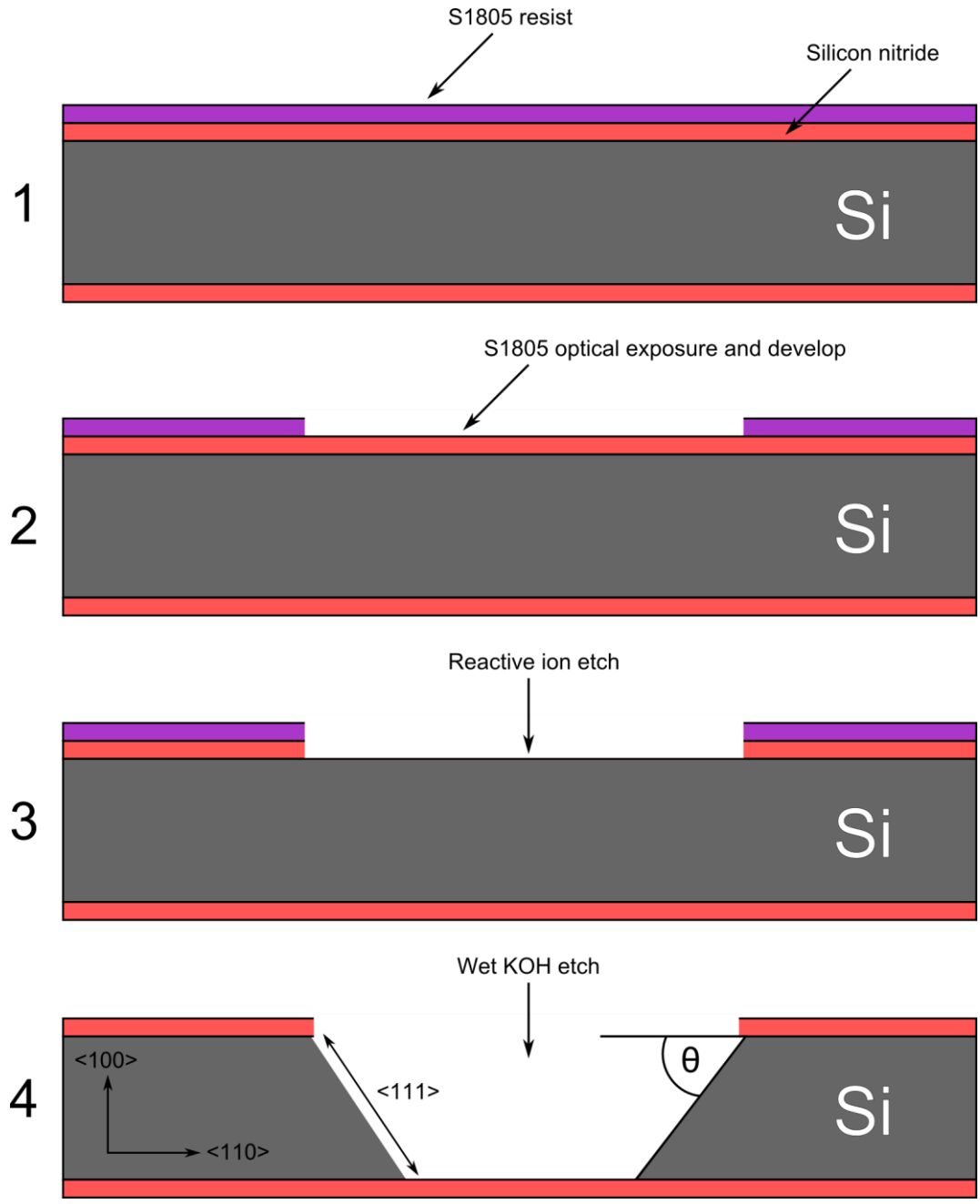

Figure 3.5.1 – Dry and wet etching of SiN_x coated Si substrates

1) A double side SiN_x coated Si substrate is spin coated with a layer of S1805 (Shipley) optical resist for lithography. 2) A section of the SiN_x is revealed via optical exposure and chemical development of the resist. 3) The substrate is exposed to a RIE, removing the SiN_x in the area defined by the developed resist. Where the resist is not exposed during lithography, the SiN_x remains unchanged. 4) The optical resist is removed in acetone, and the substrate is wet etched in KOH solution. The etch is anisotropic, with angle $\theta=54.7^o$. This etch leaves a 'window' of SiN_x on the underside of the wafer.

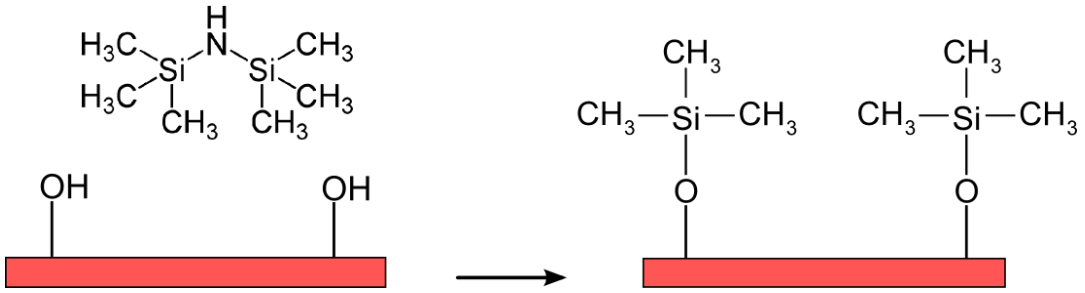

Figure 3.7.1 – HMDS deposition

Illustration of HMDS surface reaction. A molecule of HMDS reacts with two surface hydroxyl groups, leaving the surface terminated with hydrophobic methyl groups.

3.8 Fabrication of graphene electrochemical devices

The following fabrication procedures are illustrated in Figure 3.8.1 to aid in the visual understanding of the process.

A monolayer graphene sample to act as an electrochemical electrode was initially prepared via mechanical exfoliation on a flat SiO_2/Si wafer with 90 nm SiO_2 thickness. The graphene was chosen to have a defect free (determined via DF optical microscopy) domain of at least 30x30 μm^2 in area. This allowed sufficient tolerances to fabricate up to a 15 µm diameter electrode size once the subsequent steps were completed.

A mechanically exfoliated h-BN substrate was prepared on a second SiO_2/Si wafer. A minimum thickness of 70 nm was required for the h-BN flake to reduce strain when suspended. The thickness could be reasonably estimated via the colour contrast of an optical image as flakes of this thickness appear blue-green on a 90 nm SiO_2 coated Si wafer. The thickness could be accurately confirmed via AFM imaging in tapping mode if required. The area of the h-BN substrate needed to be less than the area of the graphene flake, or more importantly that the substrate could be placed on top of the graphene without covering its entire area. The h-BN substrate also needed to be larger than the proposed active electrochemical area of the graphene electrode.

The h-BN substrate was then transferred on top of the graphene layer prepared on the previous SiO_2/Si wafer, creating a h-BN-graphene heterostructure. The h-BN flake needed to fully cover the area of the graphene intended to act as the active electrochemical electrode, with the area outside this available for making electrical contact with a metal.

A 2.5 cm x 2.5 cm SiN_x/Si/SiN_x wafer with 100 nm thickness SiN_x coating was then prepared to act as the electrode body. A 0.38 x 0.38 mm^2 square area was opened in one side of the

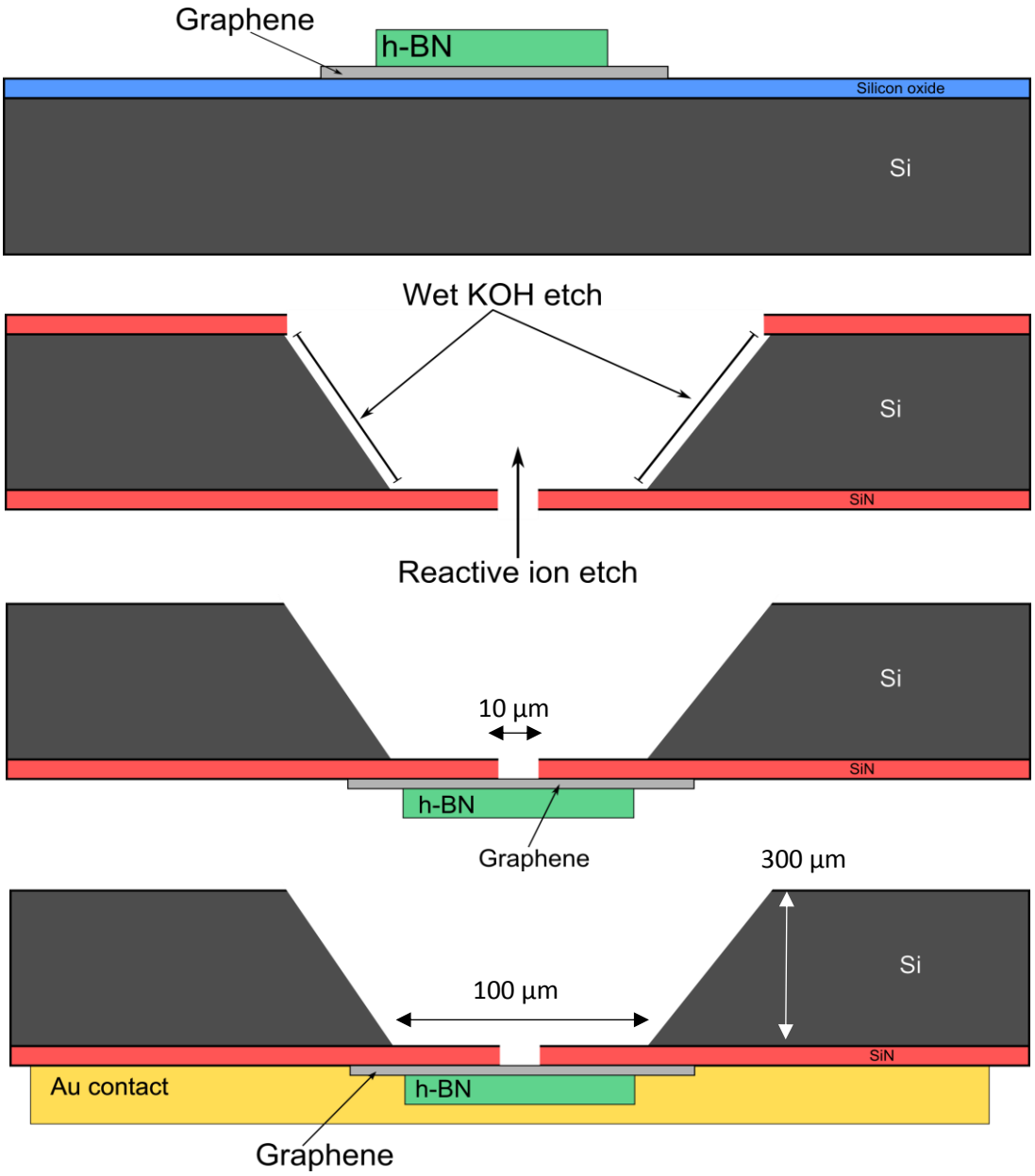

Figure 3.8.1 – Fabrication of the graphene electrochemical device

1) A h-BN-graphene heterostructure is created by transferring a h-BN flake onto a target graphene flake. 2) A second SiN_x/Si/SiN_x wafer is then modified to contain a trench in the silicon with a SiN_x window on one side. A hole is then formed in this window to define the electrochemically active area on the graphene. 3) The h-BN-graphene heterostructure is then transferred over the hole in the SiN_x window with the graphene face down on the SiN_x. 4) An electrical contact is added onto the graphene to allow measurements to be taken.

SiN_x using optical lithography followed by RIE, as shown in Figure 3.5.1. The silicon was then wet etched until a trench was formed the entire way through the wafer, exposing a ~100 x 100 µm^2 SiN_x window. A hole was then created in the SiN_x window that remained, with the area of the hole defining what would be the electrochemically active area on the graphene. For this project circular holes of 10 and 15 µm diameter were used, ensuring the devices were small enough to be within the UME regime but also ensuring the expected nA

signals were large enough to be accurately recorded. The hole was created using the same optical lithography and RIE steps as for initially removing the SiN_x on the opposing surface of the wafer. After this step the wafer was broken down into a 4 mm x 5.6 mm piece, with the SiN_x window in the centre. The modified SiN_x/Si substrate was then cleaned using an O_2/Ar plasma at 10 W for 15 mins to ensure all deposits of resist were removed and functionalising the surface with hydroxyl groups. Immediately following this the wafer was treated with vapour phase HMDS to provide a hydrophobic surface as outlined in Section 3.7.

The graphene-h/BN heterostructure previously prepared was then transferred on to the outside surface of the SiN_x window, ensuring it sat entirely covering the previously fabricated hole. As the hole defines the electrochemically active area, the graphene needed to be aligned so that there were no defects in this region, with the DF images previously taken of the flake used to aid this process. The transfer was done via the same method as for the h-BN to graphene transfer outlined in Figure 3.2.1/2. During this transfer some strain built up in the h-BN-graphene layer due to vdW forces pulling the suspended structure inwards towards the wafer body, as shown in Figure 3.8.2. It was difficult to precisely determine the amount of strain as the h-BN-graphene layers may have also slipped along the SiN_x substrate once contact was made between them. The deformation varied between devices, however AFM images suggest the h-BN-graphene layer deforms around 50 nm into a 10 μm diameter hole when the h-BN was 70 nm thick.

Electronic Ti/Au contact was then added by electron beam evaporation. A simple electrochemical sensor only requires a single contact. No lithography was needed as the outside surface of the wafer could be uniformly covered in metal assuming there were no defects in the SiN_x dielectric, which was carefully checked under optical microscopy prior to metal deposition. There could be no contact between the metal contact and the silicon part of the wafer, only the SiN_x surface, and the edges of the wafer were protected from the evaporated metal using a polyimide (*Kapton*) tape. After deposition the tape could be peeled away, leaving metal only in the central area covering the h-BN-graphene flakes.

This method describes the fabrication of a proposed graphene sensor structure where the sensing surface is not exposed to polymer or resist contamination. The graphene is prepared so the electrochemically active surface is face down on a clean SiO_2 surface, with the opposing side subsequently protected with a h-BN flake. The graphene h-BN is then removed, with the PMMA transfer membrane not contacting the graphene except outside the electrochemically active area. The processing only exposes the electrochemically active

surface to dilute KOH solution and acetone. The metal evaporation takes place on the opposing surface, leaving the area of the graphene defined by the hole in the SiN_x window pristine for sensing purposes. An electrolyte can be placed in the Si trench for measurements, with it only contacting the graphene in the area defined by the hole in the SiN_x window. Optical images of the fabrication are shown in Figure 3.8.3.

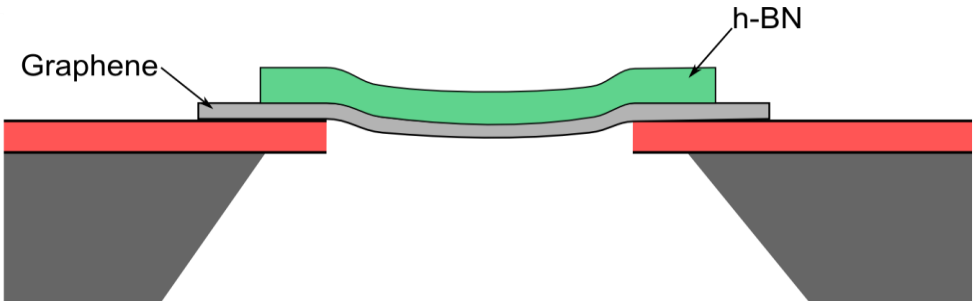

Figure 3.8.2 – Graphene transfer strain

An illustration of how a h-BN-graphene heterostructure deforms when suspended over a hole in SiN_x.

3.9 Chip carrier modification and bonding

The make measurements with the electrochemical devices they needed to be connected to an external measurement system. For this purpose a modified chip carrier was used. A chip carrier is a small unit that an electronic device can be mounted into, with electrical contact pads to connect to the small electrical contacts on the device. The contact pads on the chip carrier can then be connected to an external circuit, avoiding directly connecting to the fragile device. Due to the double sided nature of this device, that being one side for contacts, the other side for electrochemical measurements, the chip carrier needed to be modified. For this purpose a hole was drilled through the backside of a chip carrier, with the hole being slightly smaller than the chip carrier itself, shown in Figure 3.9.1.

The device could then be mounted in the chip carrier, using a small droplet of PMMA (8% in anisole) at the edges for adhesion, making sure no PMMA came into contact with the graphene. The device was mounted so that the etched trench in the silicon aligned in the centre of the hole in the chip carrier, therefore the active graphene area could be accessed through the hole in the chip carrier.

To make electrical contact between the chip carrier and the device required connecting a fine wire between the small electrical contact on the device surface and the pads on the chip carrier. This was done using an ultrasonic bonder, where a microscope allowed the wire to be aligned to the electrical contact pad on the device. Once aligned the wire is pressed into

the surface by an arm connected to an ultrasonic piezo transducer, rapidly oscillating the wire with low amplitude on the contact pad surface. This movement causes enough friction that the thermal energy generated bonds the wire to the metal contact pad creating an electrical contact. The same wire was then bonded in the same way to the pads on the chip carrier, with the bonding repeated three times for redundancy in case of contact or wire failure. The chip carrier was then attached to a glass slide coated in aluminium with double sided adhesive tape, with the sensing surface facing upwards to allow access for measurements. This contacting method required no polymers or solvents and is therefore was the cleanest possible way to make an electrical contact. (*The bonding was performed by Dr G. H Auton, University of Manchester).*

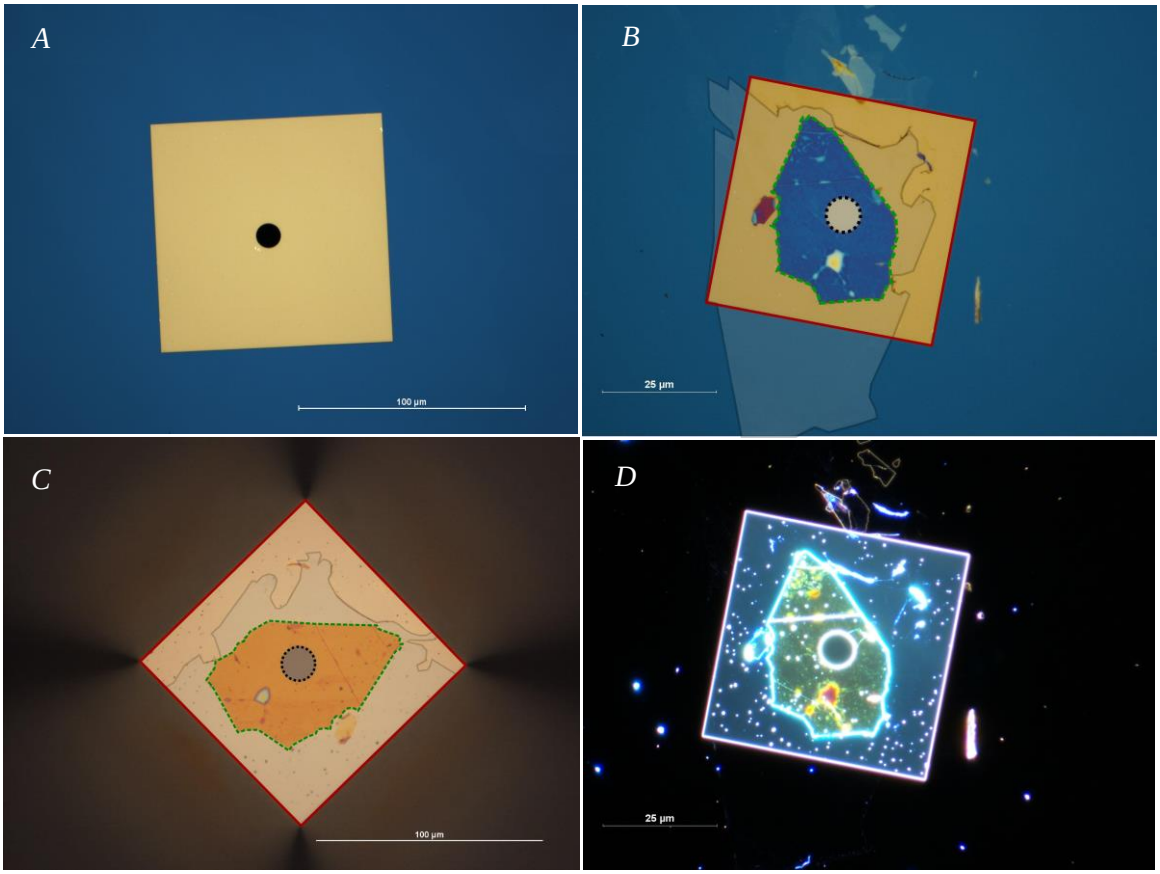

Figure 3.8.3 – Optical images of the graphene electrochemical device fabrication

A – A 100 nm thick SiN_x window with 10 µm hole. B – h-BN-graphene heterostructure transferred over a hole in SiN_x. The constituent materials are highlighted – the graphene flake area is grey, the SiN_x window border is a solid red line, the h-BN flake is the dashed green line and the SiN_x hole is the dashed black line.

C – Looking down through the etched Si trench, at the underside of the SiN_x window. The electrolyte is placed in this trench for measurement. The constituent materials can be seen through the SiN_x and are highlighted as with the above image. D – A DF image of the structure. Contamination is clearly visible, most of which is suspected to be concentrated KOH residue from the etching step (prior to graphene transfer) and PMMA residue from the transfer. The hole appears clear from contamination.

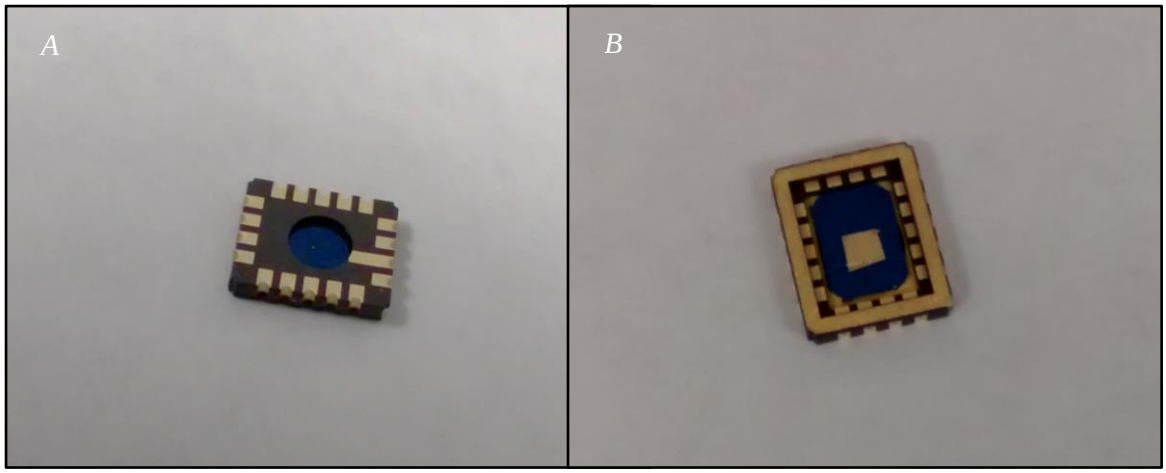

Figure 3.9.1 – Photographs of the graphene device mounted in a chip carrier

A – The mounted device (blue) looking into the etched trench in the Si (visible as a small dot in the centre of the chip carrier hole). The electrical contact pads are connected to an Al coated glass slide (not shown). The chip carrier dimensions are 6 mm x 4.35 mm.

B – The mounted device (blue) with the electrical contact pad on the device clearly visible in the centre (gold square). Around the edge of the chip carrier are contact pads which are connected to the device contact using ultrasonic bonding.

The chip carrier contact pads are electrically connected on both sides, so bonding to the device on one side allows the chip carrier contacts to be used from the opposing side.

4. Electrode characterisation

The following chapter covers the measurements recorded on the various fabricated devices. All solutions were made using DI H_2O (18.2 MΩ, *Milli-Q*, Merck Millipore) and chemicals as received from Sigma-Aldrich UK. For all CV scans, the potential was held at 1 V for 5 seconds before starting the scan. All data sets were filtered with FFT at 500 Hz for smoothing and noise reduction.

4.1 Electrochemical measurement apparatus

The devices were measured on a custom electrochemical measurement system. The system used a micromanipulator on which a holder for a 1.2 mm diameter borosilicate glass pipette could be attached, allowing the pipette to be positioned to an accuracy of 10 µm. The pipette end was shaped using a thermal pipette puller to create a taper to ~ 100 µm diameter at the tip. The holder allowed fine wires to be placed inside the pipette from the opposing end to the tapered tip. The pipette could be filled with electrolyte using a syringe and needle. If the tip of the pipette was positioned within a droplet of electrolyte on the graphene electrode surface, contact between the fluid in the pipette and the droplet allowed electrochemical measurements to be recorded. Two wires within the pipette functioned as Ag/AgCl reference and Pt counter electrodes, with the graphene electrode surface acting as the working electrode. The wires in the pipette needed to be isolated, and therefore a Ag wire with a PTFE insulating coating was used. Prior to being placed in the pipette, the PTFE coating was removed from the end of the wire, and the Ag was anodised in 1M KCl solution until a thin layer of AgCl built up on the exposed wire surface, visible as a darkened-grey colour change. For this anodisation step, the Pt wire was used as the counter electrode in a two electrode cell. The two wires were then inserted into the pipette, ensuring the length of Pt wire was less than the length of remaining PTFE coating on the Ag/AgCl wire to make sure no electrical contact occurred between the two, as shown in Figure 4.1.1. The wires were then connected to the reference and counter electrode terminals on the potentiostat (*PGSTAT302N*, Metrohm Autolab) via metal clips attached to shielded cables.

The graphene device was attached to an Al coated glass slide as previously described. The glass slide was placed on the working surface of a microscope (up to 100x magnification) and secured with adhesive putty (*Blu-Tac*, Bostik). The Al on the glass slide was connected with a metal clip and shielded cables to the working electrode terminal on the potentiostat. A droplet of the electrolyte was placed on the graphene device surface using a syringe with a fine plastic needle (28 gauge, *Microfil*, WPI). The syringe was filled with electrolyte and

the needle attached, with a small amount of pressure creating a ~ 1-2 mm droplet of electrolyte on the end of the needle. This droplet could be carefully placed on the graphene device, positioned so that the trench in the Si filled with electrolyte and made contact with the graphene surface, as shown in Figure 4.1.1. The hydrophobic HMDS layer on the device substrate ensured the droplet did not significantly wet the SiN_x surface surrounding the trench and stayed as a roughly hemispherical droplet. The microscope could be used to check that the droplet had filled the trench and was contacting the graphene.

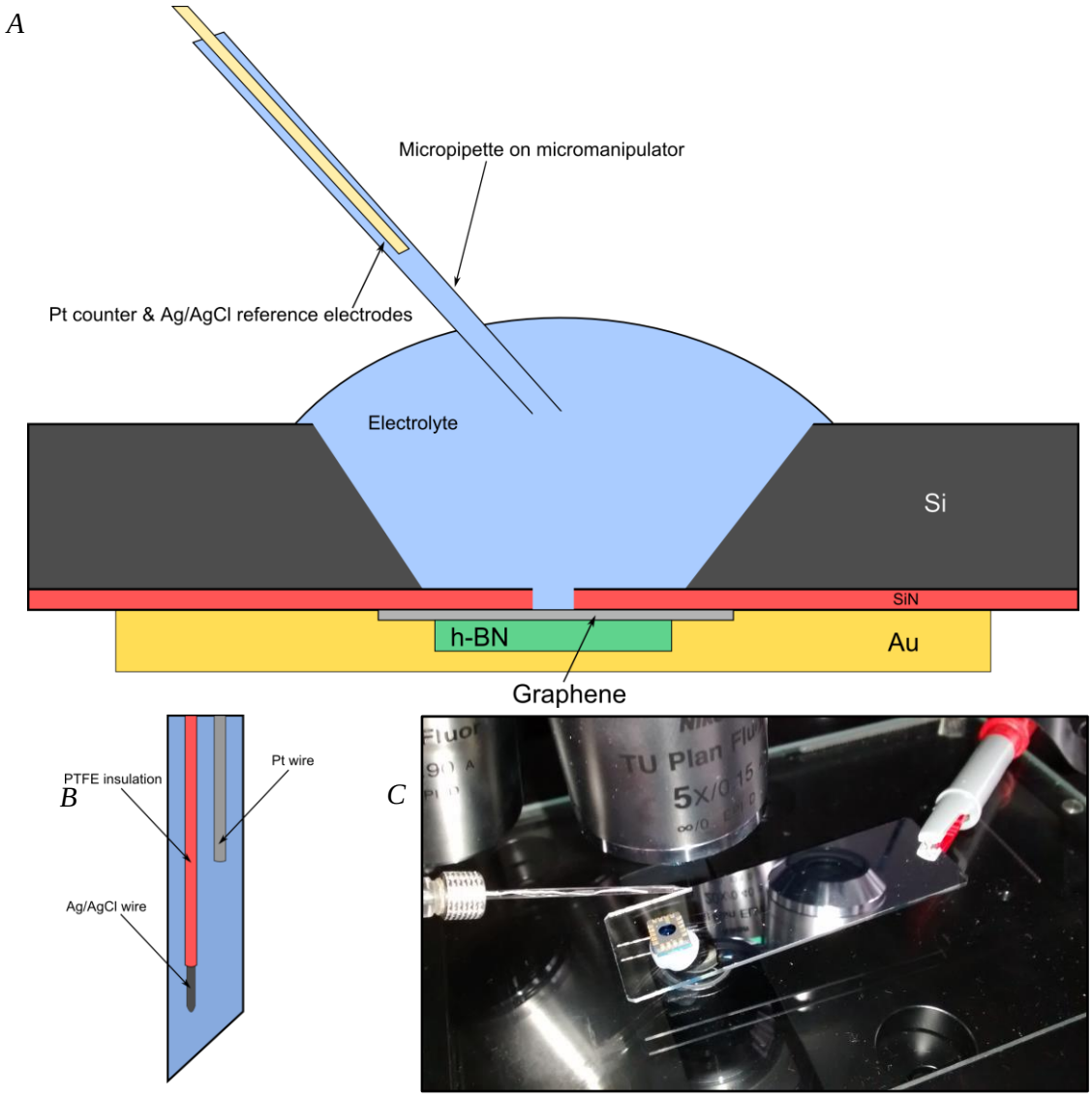

Figure 4.1.1 – Experimental setup

A – Illustration of the measurement setup for the graphene device. The droplet of electrolyte fills the etched Si trench, contacting the graphene working electrode. A pipette containing WE/CE and filled with identical electrolyte then contacts the droplet on the device surface.

B – Illustration of the arrangement of the WE/CE electrodes within the pipette. C – A photograph of the measurement stage, with the device mounted on a glass slide. The pipette and microscope lens are clearly visible above the device.

Once the electrolyte contacted the graphene, the pipette tip was rapidly positioned into the electrolyte drop with the micromanipulator, ensuring the pipette did not draw up the droplet due to capillary forces. This was avoided by placing the pipette into a beaker of identical electrolyte solution before making contact with the droplet. The setup was then ready to record measurements.

An additional setup was used to record measurements with a macro-electrode, which was used for potential calibration as described in Section 5. For these measurements a purchased 3 mm diameter basal plane HOPG electrode (*Cat. No. 002252*, IJ Cambria Scientific) was used. This electrode was used as provided, with a wash in IPA and DI H_2O prior to use. The electrode was used in an atmosphere aged state and therefore a fresh layer of graphite was not cleaved prior to use as to ensure the condition of the electrode was similar to that of the graphene. The make measurements with this electrode it was placed in a 100 ml glass beaker, with the electrode held in place by a metal clamp above the top of the beaker. The electrode was designed with a long plastic tubing with the end of the tube exposing the HOPG, and this tubing could be used to clamp the electrode in place. The end of the tube opposite to the HOPG had a metal lead for connection to a potentiostat. The beaker was filled with the appropriate electrolyte for measurement, and a Pt spade electrode was used as a counter electrode, cleaned via the same protocol as the HOPG working electrode and clamped in place in a similar manner. The reference potential was provided by a Ag/AgCl wire as with the graphene setup, with the wire easily placed in the solution using the clamp for the counter electrode, ensuring there was no contact between the different electrodes.

4.2 Control measurements

To access whether the device structure was functioning as designed, control measurements were taken. Three control experiments were performed using a slightly modified electrode structure.

A device was fabricated using a ~ 80 nm graphite flake in place of the h-BN-graphene heterostructure. Graphite was used as a test conductor to ensure the device would pass a redox current, and could be tested to destruction, avoiding the time consuming transfers required with graphene and h-BN. This device was compared to a device fabricated without a hole in the SiN_x window or a graphene flake, but with a Au contact on the underside of the SiN_x window as with the original device structure. This device still had the etched trench in the Si and was constructed to test if the SiN_x was completely insulating and no current was passed due to reactions with the Si trench.

Another device was fabricated with just a h-BN substrate and Au contact with no graphene layer. This was used to access the sealing between the SiN_x substrate and the flake transferred over the hole. This device should show no current as h-BN is insulating, so if significant current was measured electrolyte was likely to be leaking between the h-BN flake and SiN_x substrate towards to the Au contact at the edges of the h-BN flake. The results of these control measurements are shown in Figure 4.2.1.

4.3 Reduction electrochemistry

Redox measurements were made on four h-BN-graphene heterostructure electrodes using the ammonium salt of $IrCl_6^{2-}$ (*ammonium hexachloroiridate (IV))* in a 0.15 M KCl supporting electrolyte. This outer sphere redox couple undergoes a reduction to $IrCl_6^{3-}$. CV scans were recorded at a range of potential scan rates, over a potential range of $1.2 \rightarrow -0.2$ V. This potential range was recorded to allow the current to reach the steady-state limit. The electrolyte strength was chosen due to its simulation of biological sensing conditions.

All four devices showed similar behaviour. A comparison of fitting parameters is shown in Chapter 5. An example of these redox measurements are shown in Figure 4.3.1.

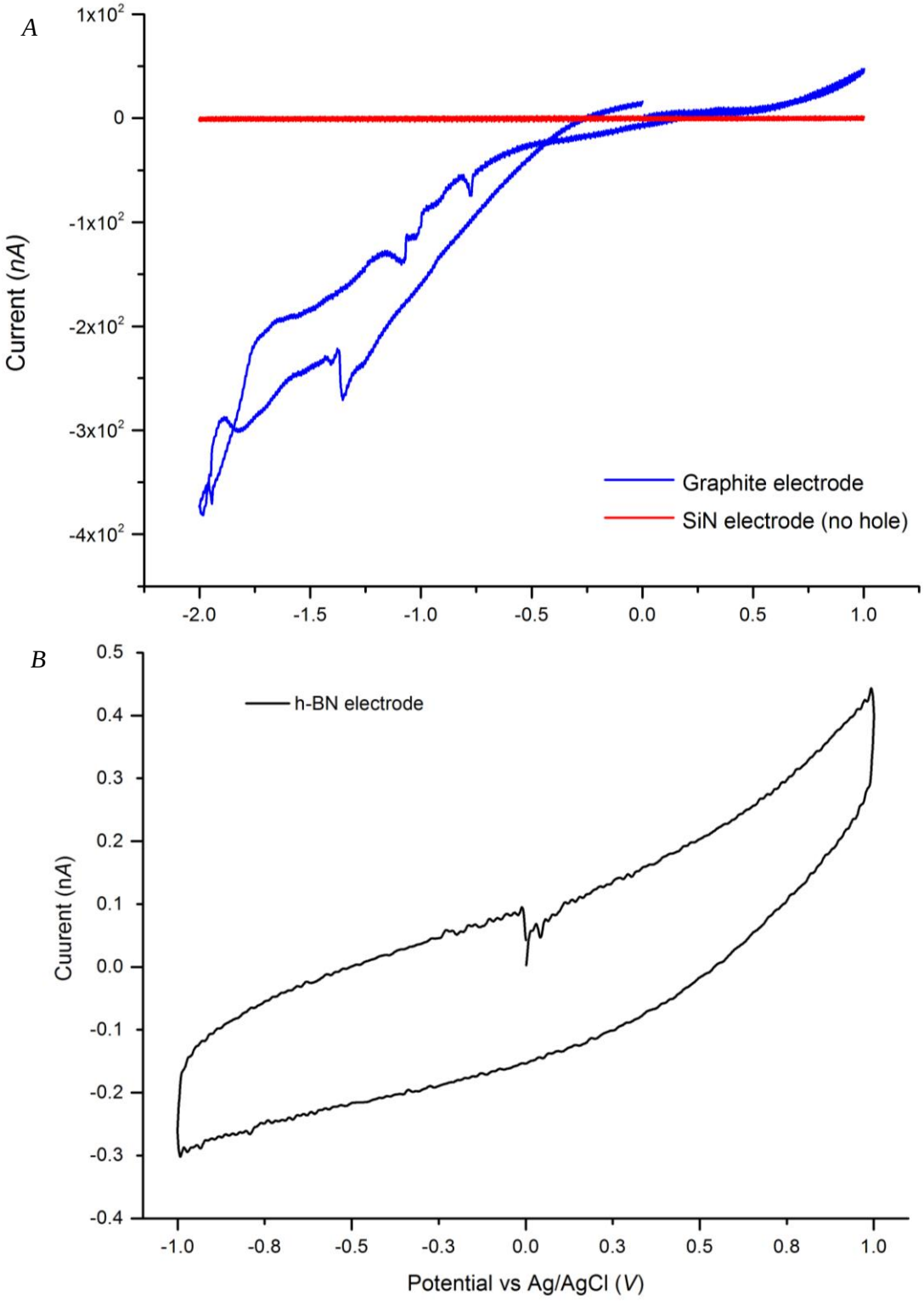

Figure 4.2.1 – Control measurements

A – Measurements taken on a SiN_x electrode with no hole, and a 10 µm graphite electrode. This is the data from the 3rd cycle of a repetitive CV scan. B – Measurement using a 10 µm h-BN electrode.

Electrolyte: 1.5 M KCl. Scan rate: 100 mVs^{-1}.

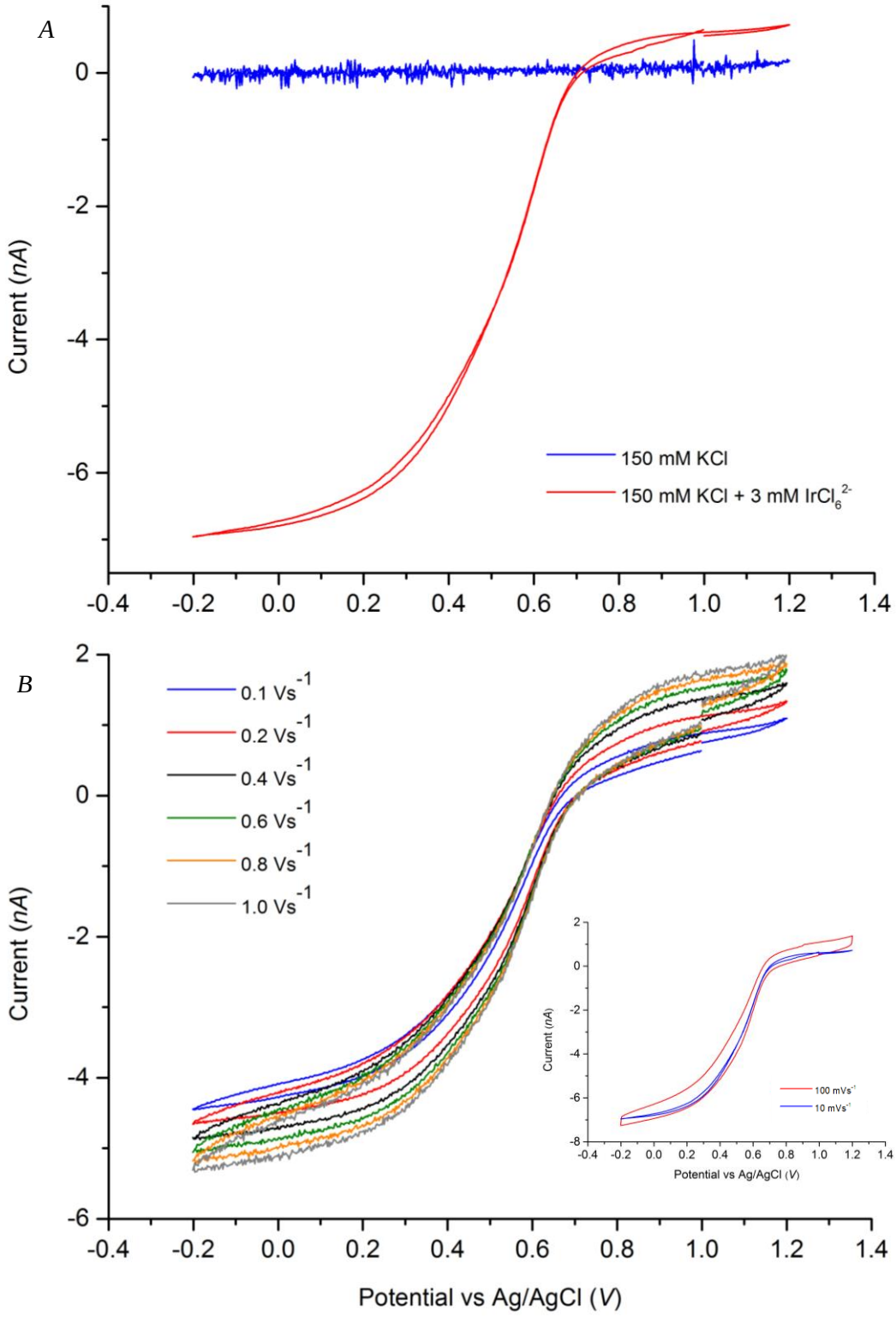

Figure 4.3.1 – Reduction electrochemistry

A – The reduction of 3 mM $IrCl_6^{2-}$ in 150 mM KCl supporting electrolyte compared to the supporting electrolyte with no redox couple (background). Scan rate is 10 mVs^{-1}(15 µm diameter electrode). B – The reduction of 3 mM $IrCl_6^{2-}$ in 150 mM KCl at a range of scan rates 0.1 - 1 Vs^{-1}(10 µm diameter electrode).

The inset (B) shows the comparison of 10 mVs^{-1} to 100 mVs^{-1}(15 µm diameter electrode).

4.4 Repeat measurements on the same device

Repeat measurements were made, whereby the droplet of electrolyte was removed from the device and a new one deposited. This means the device surface will have potentially dried in between measurements leading to contamination on the device. These measurements were recorded to test the re-usability of the devices. The change in response between devices was not consistent and seemed to show random variations, however only 4 devices were measured in this way so not enough data was recorded to deduce any trends. Example data is presented in Figure 4.4.1. Due to this change between measurements, all analysed data is taken from the first run on each device as this data should be most representative of a pristine graphene surface.

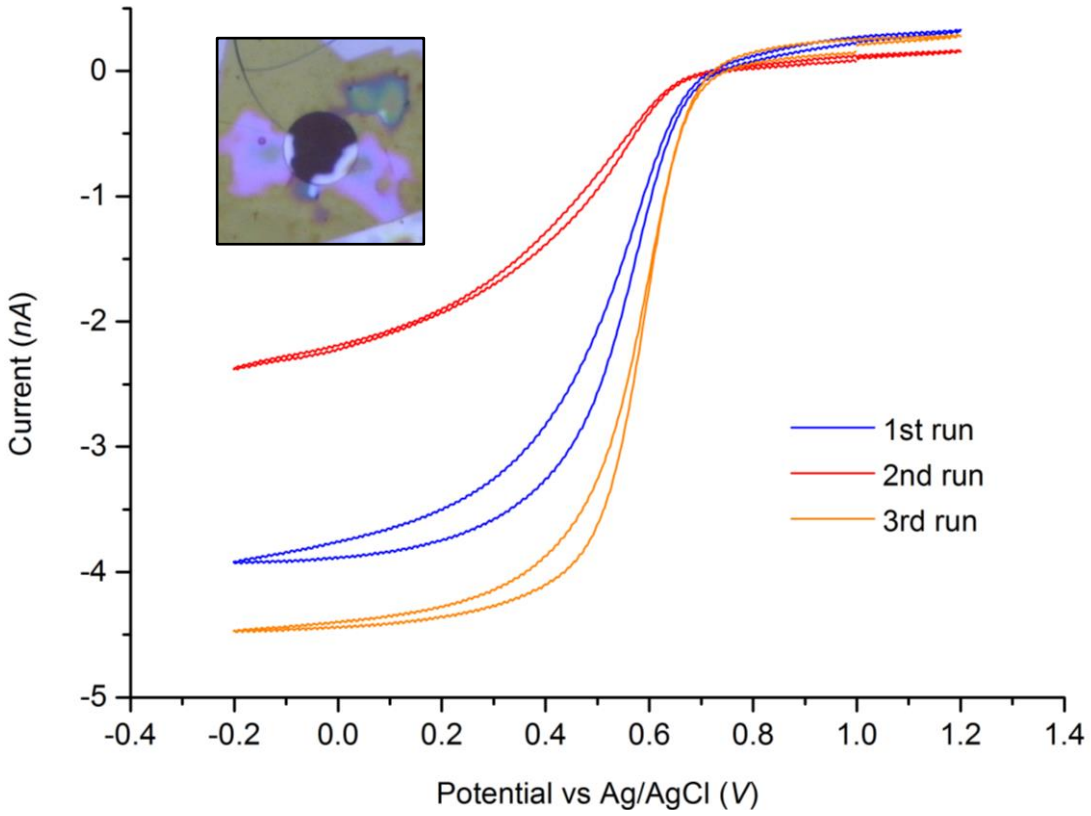

Figure 4.4.1 – Repeat measurements

Comparison of results from re-using the same device 3 times. Each run has had the electrolyte removed and replaced by a new droplet. Inset: post measurement drying contamination

Electrolyte: 3 mM $IrCl_6^{2-}$ in 150 mM KCl. Scan rate: 100 mVs^{-1}(10 µm diameter electrode).

4.5 Raman spectroscopy

Raman spectroscopy measurements were recorded before and after electrochemical measurement of the devices, shown in Figure 4.5.1. This allowed the initial quality of the graphene to be assessed once fabricated into a device structure, and then a comparison could

be made to this initial quality once the device had been exposed to the electrolyte and undergone electron transfer. The number of electrochemical measurements made on each device varied, but all were subject to at least 15 CV scans and 3 deposited droplets of electrolytes. There were no statistically relevant differences in the Raman data between devices so a representative spectrum is show. No significant differences were seen between different areas of the electrode apart from increasing contribution from the SiN_x background toward the electrode edges. The peak positions shifted subtly between devices but this is thought to be due to differences in strain when transferred over the hole in the SiN_x substrate as shown in Figure 3.8.2. *(The Raman measurements and analysis were performed in collaboration with Dr S.D Heeg, Swiss Federal Institute of Technology, Zurich).*

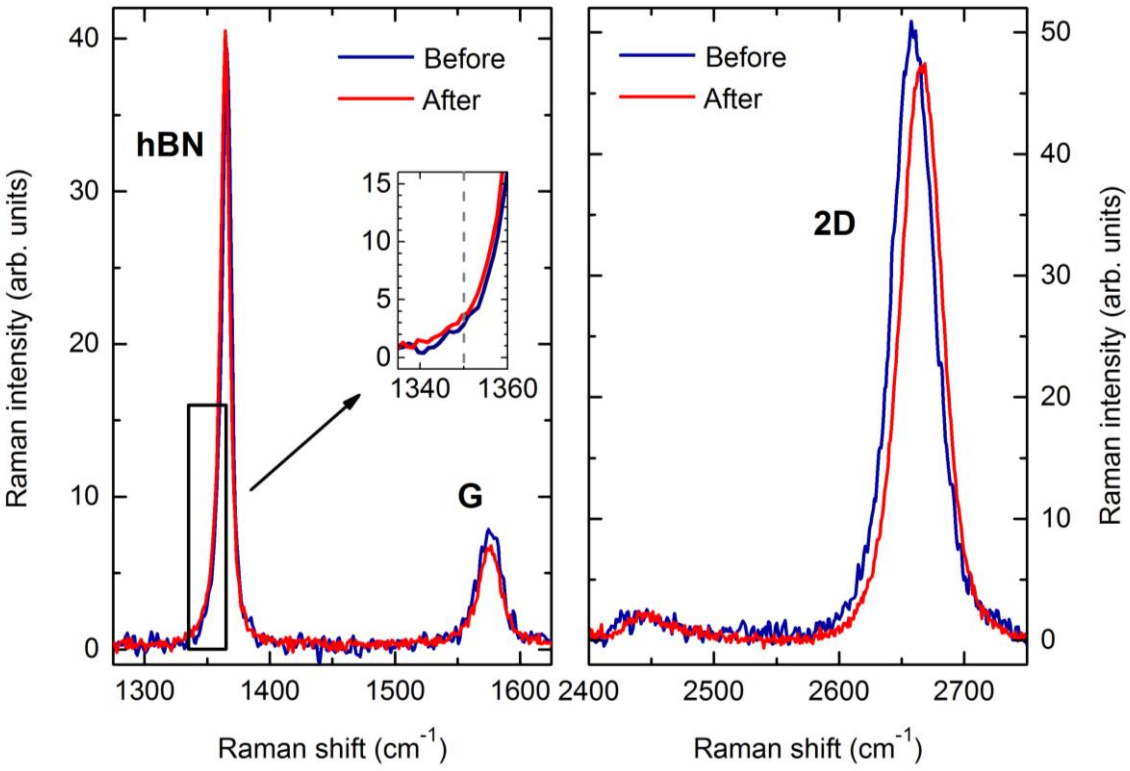

Figure 4.5.1 – Raman spectroscopy

A comparison of Raman spectra for a device before and after electrochemical measurements. Inset shows expected position of the D peak (grey dashed line). Laser wavelength was 532 nm and spectra were taken in the centre of the electrode. Raman shift resolution is ~ 4 cm^{-1}.

FWHM(2D): Before – 36 cm^{-1}, After – 36 cm^{-1}. FWHM(G): Before – 20 cm^{-1}, After – 21 cm^{-1}

Pos(2D): Before – 2660 cm^{-1}, After – 2665 cm^{-1}. Pos(G): Before – 1575 cm^{-1}, After – 1575 cm^{-1}

I(G)/I(2D): Before – 0.1. I(G)/I(2D): After – 0.1

Pos(h-BN) – 1365 cm^{-1}. Pos(D) – 1350 cm^{-1}

5. Electrochemical analysis

5.1 Fitting of experimental data

The experimental data for the reduction of $IrCl_6^{2-}$ was fitted to the empirical formula proposed by *K. B. Oldham* and *C. G. Zoski* (Equations 2.11.9-11), hereinafter referred to as the O-Z formula. A small correction for the electrode recess in the substrate is included, as described in Equation 2.11.13. This manifests as a small correction of ~2.5% in the electrode radius and has no effect on the shape of the fitted curve. The experimental data was fitted to the O-Z formula using a non-linear least squares fitting program with the fitting parameters varied. It is often assumed when fitting electrochemical voltammograms that α=0.5, however this was initially allowed to vary as a fitting parameter to assess whether this assumption is correct for this particular system. The parameter k^0 was the main parameter of interest and was allowed to vary as a fitting parameter. The electrode radius, r_o, was also set as a variable fitting parameter as a way of accessing the effective area of the electrode undergoing electron transfer with the redox mediator. The diffusion constant for both the reduced and oxidised forms of the redox mediator was taken as 7.5×10^{-6} cm^2s^{-1} as this value was commonly used in previous studies [149,154]. The temperature was estimated to be 293 K (room temperature) and *R* and *F* and took standard book values [37].

The formal potential of the reaction, $E^{0'}$, is unknown and needed to be independently estimated. To do this, a CV scan was performed using a purchased 3 mm diameter basal plane HOPG electrode (*Cat. No. 002252*, IJ Cambria Scientific). This electrode was placed in a glass beaker containing 3 mM $IrCl_6^{2-}$ in 150 mM KCl supporting electrolyte as with the graphene measurements. Due to the increased electrode area a departure from the steady-state microelectrode response was seen and two peaks (E_{pa} and E_{pc}) consistent with macro-electrodes were measured. An estimation of $E^{0'}$ is possible from the average potential of the two peaks ($E^{0'} \sim (E_{pa} - E_{pc})/2$), assuming k^0 is not very small (reversible or quasi-reversible kinetics) and the diffusion constants for both oxidised and reduced species are similar [37]. Although $E^{0'}$ may be different for HOPG and graphene electrodes, these surfaces are very similar and other studies comparing carbon surfaces in the same electrolyte do not see significant changes in $E^{0'}$ between surfaces [85,128]. The value of $E^{0'}$ obtained from this method was 651 mV (vs Ag/AgCl in 0.15 M KCl) and is relatively consistent with other studies using $IrCl_6^{2-}$ on graphene [75], HOPG [149] and Pt [154] electrodes. A comparison of the experimental data from the graphene device and HOPG electrode is shown in Figure 5.1.1. The CV on the HOPG electrode yielded a k^0 value of 3.64×10^{-4} cms^{-1}, which is slower than generally recorded [128], however, this may be due to not cleaving a fresh layer of HOPG prior

to use, with atmospheric contamination slowing the kinetics. This is consistent with how the graphene electrodes were prepared, and is therefore a good comparison.

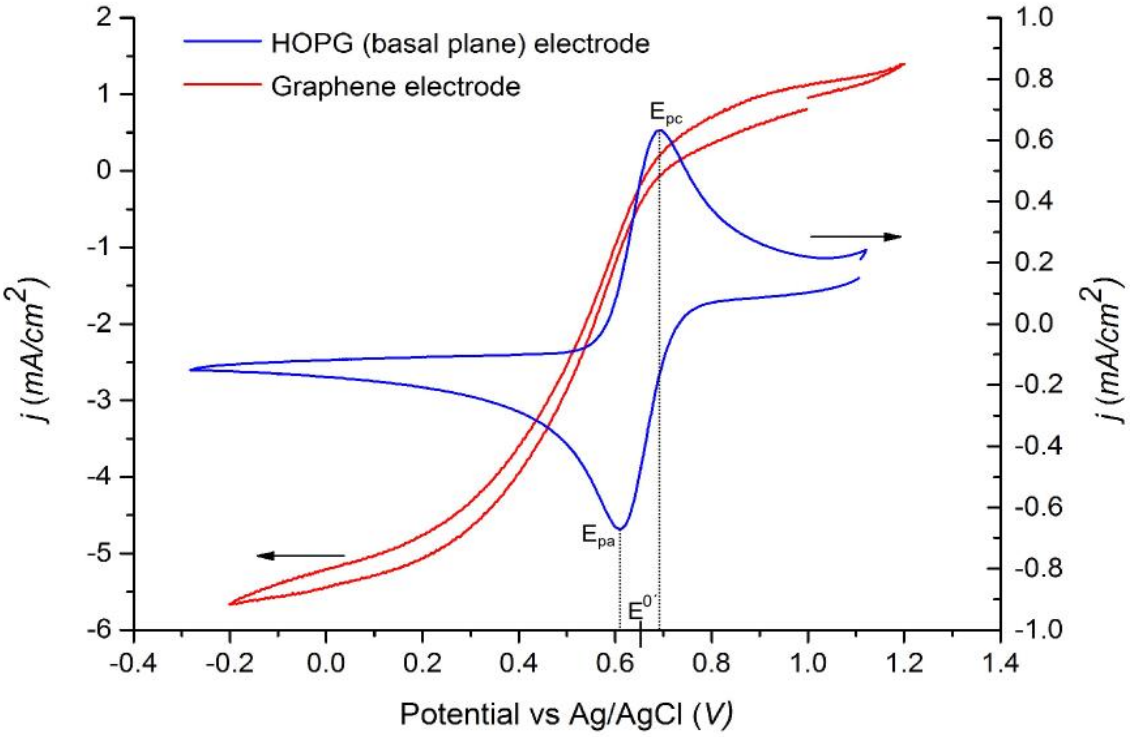

Figure 5.1.1 – HOPG comparison

A comparison of the redox of 3 mM $IrCl_6^{2-}$ in 150 mM KCl supporting electrolyte for graphene and HOPG (basal plane) electrodes. The graphene and HOPG electrodes have a diameter of 10 µm and 3 mm respectively. The estimated value of $E^{0'}$ is calculated as 651 mV (vs Ag/AgCl in 0.15 M KCl). k^0 from Nicholson method - 3.64×10^{-4} cms^{-1}.

The data recorded at a CV scan rate of 100 mVs^{-1} was analysed. Although slower scan rates are preferable due to reduced distortion from capacitive charging currents, the small size of electrolyte droplet on the device surface meant evaporation could be an issue over longer measurement time scales. A scan at 10 mVs^{-1} would take over 4 minutes to be recorded, meaning evaporation could be significant for a ~ 1 mm diameter droplet. Figure 4.3.1 demonstrates that the CV is still within the steady-state regime at these scan rates and that the capacitance background does not lead to any significant departure from the response observed at slower scan rates. A contribution to the capacitance background is a parasitic signal in parallel through the SiN_x substrate. As the Au electrode covers the entire 100 nm thick SiN_x window a capacitance is formed between the Au and the electrolyte solution across this dielectric. This parasitic signal, along with the variation between measurements on the same device made background subtraction unreliable and therefore all data was fitted as measured. Figure 5.1.2 presents the fitting of experimental data to the O-Z formula, including the effects of different fitting parameters.

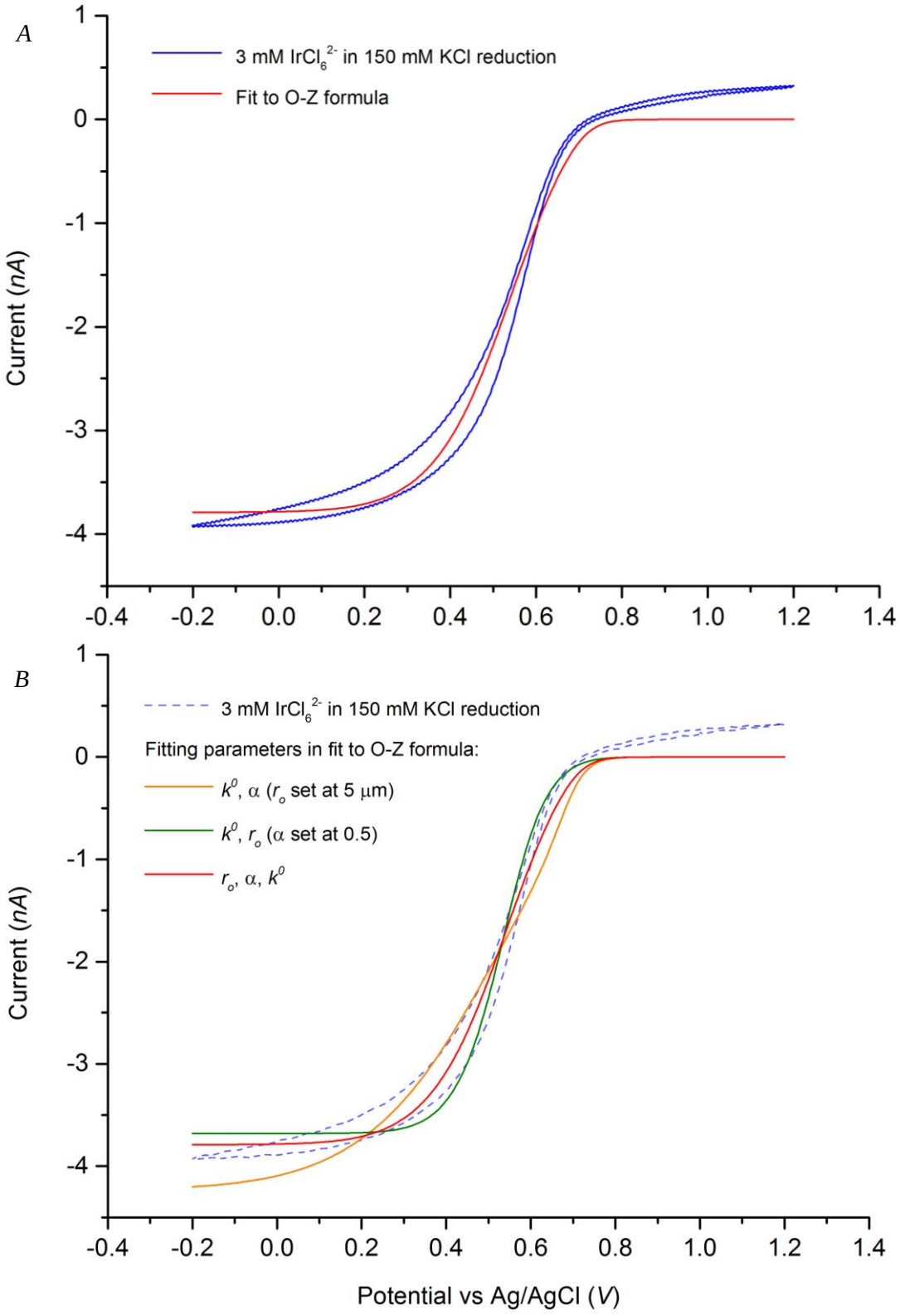

Figure 5.1.2 – Fitting of experimental data

A – Fitting of experimental data to the O-Z formula. α, r_o and k^0 are all varied as fitting parameters. B – Comparison of fitting parameters for goodness of fit to the O-Z formula. Fabricated electrode radius – 5.0 µm. Electrode radius from fit – 4.5 µm.

Experimental data - Electrolyte: 3 mM $IrCl_6^{2-}$ in 150 mM KCl. Scan rate: 100 mVs^{-1}.

Inspection of Figure 5.1.2(B) shows how the quality of the O-Z formula fit depends on which fitting parameters are allowed to vary during the fitting process. Setting α as 0.5 leads to an overshoot of the experimental data at higher potentials near $E^{0'}$ and undershoots the data at lower potentials towards the steady-state limiting current. Therefore it seems necessary to allow α to vary as a fitting parameter to acquire a good fit.

The effect of setting a fixed value for r_o during fitting is particularly detrimental to acquiring a good fit. Although the electrode radius can be directly measured optically, whether this translates directly into the electrochemically active area is less clear and is discussed further is Chapter 6. If r_o is set at the optically measured value, the steady-state limiting current is overestimated by the O-Z formula, suggesting the active electrode area is less than measured optically. As the steady-state limiting current depends on the electrode radius (along with the fixed values of electrolyte concentration, temperature and diffusion constant), the fitting function is forced to tend to the value set by these parameters. This is in turn detrimental to the fitting of the rest of the reduction curve as the values of α and k^0 become unrealistic in an attempt reach the fixed steady-state current value. By setting r_o as a variable fitting parameter the steady-state current magnitude can change allowing far more accurate values of α and k^0 to be obtained. Using an excessive number of fitting parameters is not ideal, however in this case accurate fitting is dependent of increasing the number of degrees of freedom of the fit. The values summarised in Table 5.1.1 are obtained from 4 devices as the result of using 3 variable fitting parameters, r_o, α and k^0.

The variation in the parameters between devices is shown in graphical form in Figure 5.1.3. This graph highlights that the variation between devices is much larger than the error on the fit.

5.2 Experimental errors

To access the effect of other sources of experimental error, in particular on the steady-state limiting current value, a fit was performed with r_o set as the optically measured value and the concentration, temperature and diffusion constant values set at the error limiting values. The steady-state current has a theoretical limit that depends only on these parameters and therefore if none of these can vary during fitting, the steady-state current of the fitted curve will represent the error bounds of the theoretically predicted value. By allowing α and k^0 to vary as fitting parameters, the effect of the experimental error on these values can be assessed. Figure 5.1.4 presents this data. As all the reduction curves showed smaller than expected limiting current the upper limit values have not been shown.

Sample No.	k^0 ($\times 10^{-3}$ cm s^{-1})	$\pm 2\sigma$ ($\times 10^{-3}$ cm s^{-1}) *(fit)*	α	$\pm 2\sigma$ *(fit)*
1	3.46	0.24	0.271	0.010
2	4.54	0.16	0.324	0.006
3	1.41	0.05	0.228	0.004
4	2.74	0.08	0.263	0.005

$\overline{k^0}$ ($\times 10^{-3}$ cm s^{-1})	$\pm \Delta k^0/\sqrt{N}$ ($\times 10^{-3}$ cm s^{-1})		$\bar{\alpha}$	$\pm \Delta\alpha/\sqrt{N}$
3.04	0.78		0.272	0.024

Table 5.1.1 – Results from 4 devices

Top table: The parameters α and k^0 outputted from fitting experimental data to the O-Z formula. σ represents the standard error from the fit (68.3 % confidence level).

Bottom table: The mean of α and k^0 from the 4 devices with the associated error on the mean, where Δ indicates the range of the results (N=4).

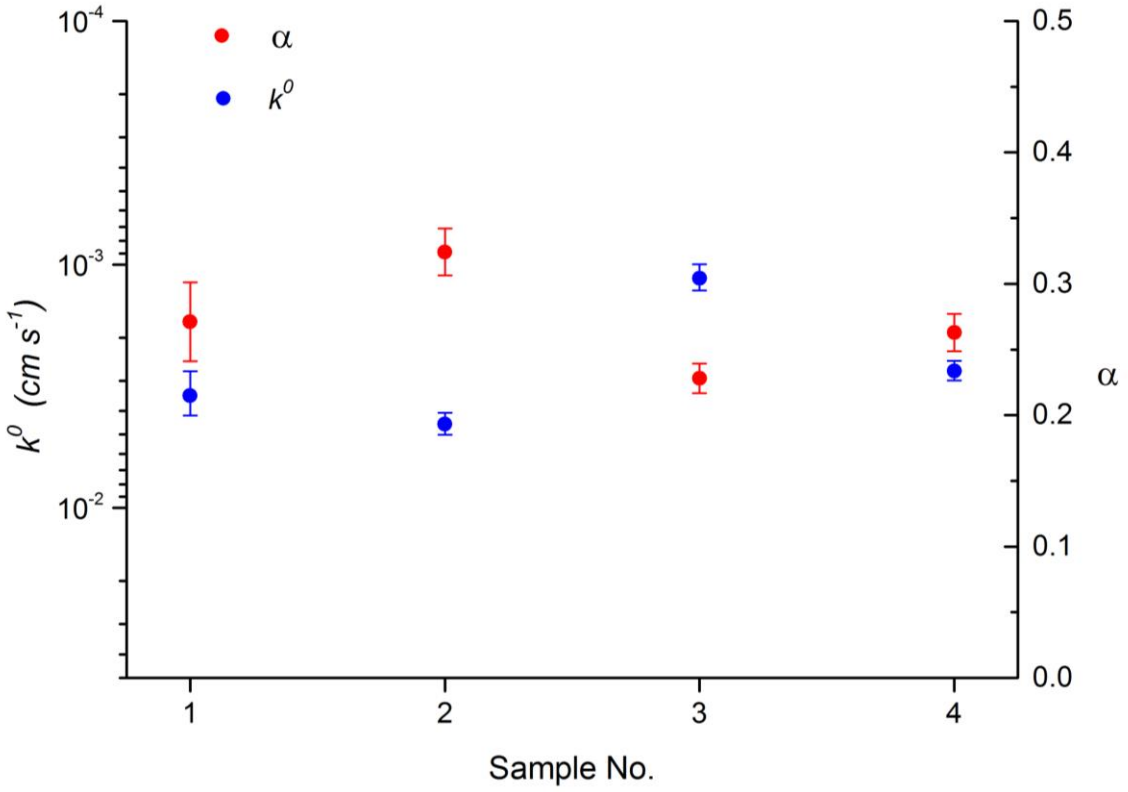

Figure 5.1.3 – Comparison of α and k^0 between devices

A comparison of α and k^0 values outputted from fitting experimental data to the O-Z formula for different devices. The error bars represent the error on the fit and have been increased by a factor of 3 for clarity.

The temperature was estimated to have an error of ± 1% (± 3 K), as the room was not temperature controlled. The actual temperature was not recorded at the time of measurement but a range of 290-296 K is consistent with typical indoor lab temperatures. The error on the concentration of the redox mediator was taken as ± 0.83%, given by standard error propagation for the individual errors on the analytical scales and volumetric flask. The error on the diffusion constant was estimated by inspecting the range of values quoted in previous studies, with a range of 10 % found [149,155]. Figure 5.1.4 shows that the experimentally measured steady-state current is consistent with the theoretical value to within the experimental error. With the lower error limit the value of α increased insignificantly by 2.2%, however the change in k^0 was larger, reducing by 22 %.

No correction was made for uncompensated resistances [156] as the current never exceeded 10 nA. It is assumed the Au-graphene contact resistance is the largest source of resistance (usually < 100 kΩ) [157] and therefore voltage drops ($V=iR$) would be of the order of a few mV and are well below the overall accuracy of the data.

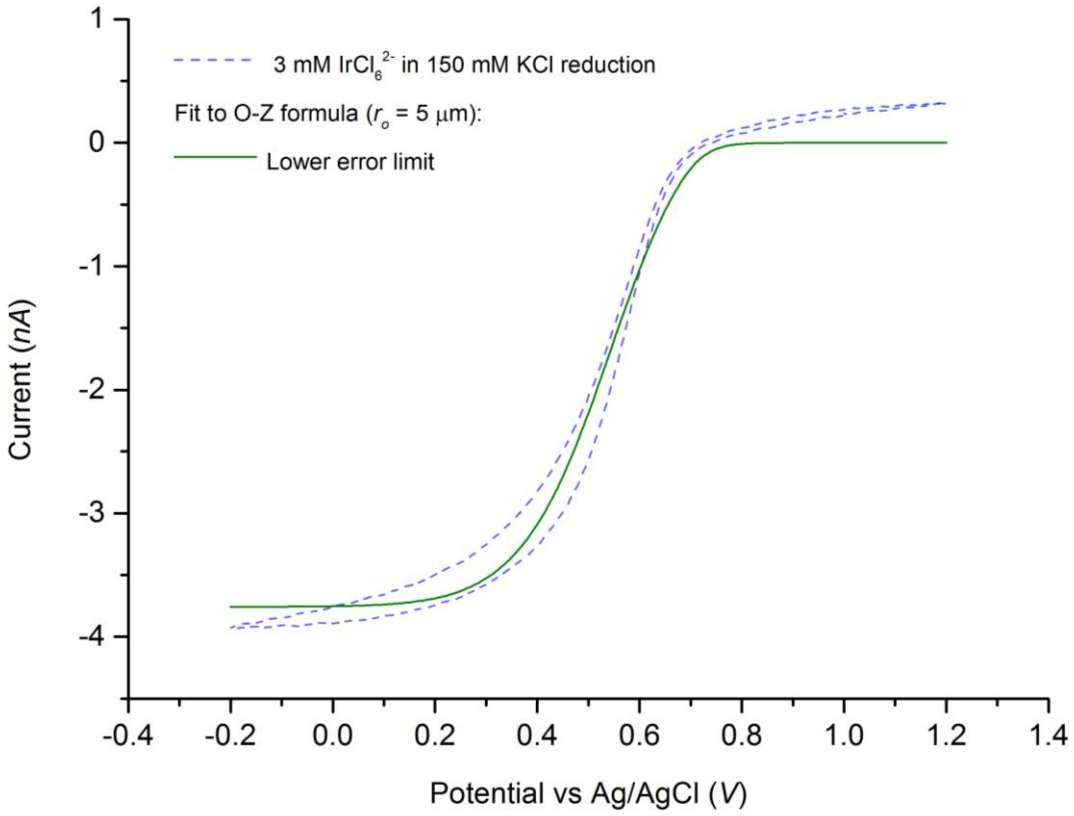

Figure 5.2.1 – Effects of experimental error

The lower error limit curve is a fit to the O-Z formula with r_o set as the measured electrode radius (5 μm) and using the lower bound error values for the concentration, diffusion and temperature. α and k^0 are fitting parameters.

α = 0.331, $k^0 = 3.55 \times 10^{-3}$ cms^{-1}

5.3 Linearising the transfer coefficient

As discussed in Section 2.9, α is assumed a constant. This oversimplification can be tested using the experimental data from the measured devices. By setting α as a linear function within the O-Z formula, the first order potential dependence of α can be estimated.

Figure 5.3.1 shows the result of fitting the O-Z formula with $\alpha(E) = \beta E + \gamma$, using β and γ as fitting parameters.

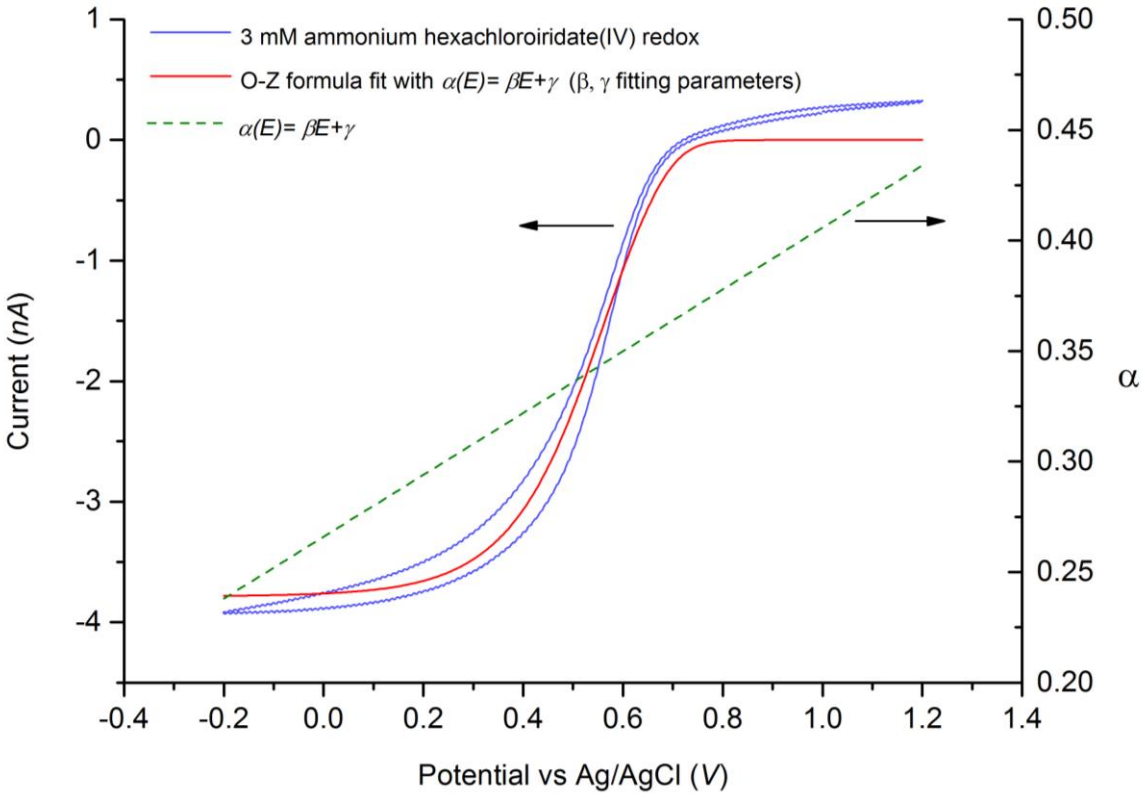

Figure 5.3.1 – Linear transfer coefficient

The effect of linearised α on the fitting of the experimental data to the O-Z formula. This fit uses using β and γ as fitting parameters. r_o and k^0 are set as the values from the initial fit in Figure 5.1.2.

$\beta = 0.140 \pm 0.021\ V^{-1}$, $\gamma = 0.266 \pm 0.009$

Figure 5.3.1 shows that allowing α to vary as a linear function of the potential improves the general quality of the fit. This is particularly evident at lower potentials approaching the steady-state limiting current. The values of β and γ were not consistent between devices, but all gave the same positive gradient (i.e. α increases with increasing potential). As linearising α is a speculative estimate and is not based on theory, comparing precise values between devices is not of particular interest and therefore Figure 5.3.1 is used to show example data.

6. Discussion

The following chapter discusses the significance and limitations of the findings presented in this thesis.

6.1 Proof of concept device operation

One of the key aims in this project was to produce a graphene device that facilitated the generation electrochemical redox current whilst avoiding polymer contamination during fabrication. Figure 4.3.1 demonstrates this aim was successful, as the reduction of $IrCl_6^{2-}$ is clearly distinguishable from the flat background recorded in blank KCl electrolyte. This figure also demonstrates the expected steady-state UME behaviour, with CV scan rates from $0.01 \rightarrow 1\ Vs^{-1}$ showing little deviation apart from an increase in capacitive charging current. Figure 4.2.1 shows that the Si trench does not contribute to the measured current and no current or electrolyte leakage occurs through the SiN_x substrate.

The device using a h-BN flake as the electrode shows an expected capacitance signal, originating from the capacitive coupling between the Au electrode and the electrolyte solution through the ~ 80 nm h-BN dielectric. There will also be a significant contribution in parallel to this capacitance through 100 nm thick SiN_x substrate separating the electrolyte and the Au contact that covers the entire SiN_x window. This capacitance will vary between devices due to the SiN_x substrate fabrication having an inherently large error in the etching process of ~ 25 μm^2. This parasitic signal prevented any capacitive measurements been made and would need to be reduced for future measurements, as outline in Chapter 7, particularly if this device is intended to be used as a sensor.

The h-BN electrode data shows the expected response of a CV scan showing only capacitance (a rectangular 'box' response) with distortion due to diffusion of the electrolyte (sloping linear offset in the 'box' response). At potentials above ~ +0.8 V the scan deviates slightly from this ideal response, maybe due to a small amount of electrolyte leaking between the SiN_x substrate and h-BN flake. However, this deviation is small and less than 0.5 nA. There was further evidence that the sealing between the SiN_x substrate and electrode flake was robust, both within the data and visually. Firstly, the steady-state reduction current measured for $IrCl_6^{2-}$ was slightly less than theoretically expected, which is inconsistent with increased current caused by leaking. Secondly, when a device did leak it appeared visually as a series interference fringes under a microscope, due to the thin water layer between the flake and substrate interacting with the incident light. This leaking could be induced by applying excessive potential between the CE and WE. The potential leaking occurred at was

not tested in detail, however it appeared to occur at potentials in excess of ± 1.5 V. The graphite data in Figure 4.2.1 is an example of a device with leaking due to excessive potential, with the current density in this device above that expected. The leaking in this device was clearly visible. This is thought to be an electro-wetting effect [158], with higher potentials increasing the attraction of water between the SiN_x substrate and the flake. This leaking was not observed in the potential range used to measure $IrCl_6^{2-}$ (-0.2 V → +1.2 V).

The lower than expected steady-state current could have a number of causes. The largest difference between expected and recorded current is –10 %. This could have been due to areas of thick atmospheric contamination, unavoidable and often seen in TEM images [79]. The effect of contamination should be small for outer sphere redox processes, yet particularly thick areas will still effect electron transfer. It is difficult to assess the level of this contamination without exposing the device to electron microscopy, which in turn causes the build up a thick hydrocarbon contamination in areas exposed to the electron beam. As shown in Figure 5.2.1, the estimated error on the steady-state current is in excess of ± 10 % so the lower than expected value is consistent with this. However, all the devices measured had a limiting current towards the lower error limit with different solutions used and ambient conditions present. A true random error would be reflected in values being both above and below the theoretical value and therefore it is more likely a systematic effect is present such as atmospheric contamination. However, only 4 devices were compared and therefore the statistics are limited. It is also worth noting that the atomically flat h-BN substrate means the measured graphene area is a very true reflection of the actual area, and no correction in area due to surface roughness is required.

6.2 Raman analysis

The Raman spectroscopy shows the graphene is a very high quality monolayer. There is no detectable D peak and the I(G)/I(2D) ratio of 0.1 is consistent with pristine graphene, with a ratio of <0.3 being considered low doping [104]. There is no D peak detectable before or after electrochemical measurement, ruling out the effect of defects on the electrochemical reduction measurements and implying that the electrolyte causes no significant damage (sp^3 defects) to the graphene during these measurements. The effect of nanoscale defects cannot be ruled out as the spatial resolution of Raman is ~ 0.5 µm. However, a degree of nanoscale defectiveness is always observable in graphene and is unavoidable [79].

The Raman spectra all show some broadening and downshifting of the of the G and 2D peaks beyond the typically measured values [109,110], although it is not uncommon to see some

variation in Raman spectra between samples [104]. These broadened values are not consistent with doping changes as the I(G)/I(2D) is too low and doping causes upshifting of the G peak [105]. These values indicate strain, which cause peak broadening and downshifting [107,108,159]. The strain is believed to originate from transferring the h-BN-graphene heterostructure over the hole in the SiN_x substrate as shown in Figure 3.8.2. This strain is not uniaxial or constant over the Raman excitation area and therefore represents a complex picture for analysis. An estimation of the strain from the peak positions is given by *T. M. G. Mohiuddin et al.* [108], yielding a value in the range $0.45 \rightarrow 0.55$ %, which is not thought to have any significant effect on the electronic structure of graphene [159]. The slight upshift in 2D peak position after electrochemical measurements could be due to a small rearrangement of this strain after contact with the electrolyte, although this upshift value is on the very limit of the resolution of the Raman system.

6.3 Result reproducibility

Qualitatively, the results between devices were consistent with no anomalous measurements taken. The average values of the kinetic parameters k^0 and α for the reduction of $IrCl_6^{2-}$ are calculated as $3.04 \pm 0.78 \times 10^{-3}$ cms^{-1} and 0.272 ± 0.024 respectively, averaged between 4 devices. The standard deviation in the range of results are 25 % and 8.8 % of the mean value for k^0 and α respectively. A relatively large spread in results is expected for graphene devices [75], with mobility and the DP position having uncontrollable variation in FET measurements [20] so this spread in k^0 is likely reflecting the intrinsic sensitivity of graphene to external factors such as atmospheric conditions and trace contaminants. The Raman spectra indicate consistent low doping on all the devices. The effect of PMMA (or other polymer) residues can be ruled out as the cause of variation between devices as this was not used on the active graphene surface during fabrication. The precise effect of atmospheric contaminants on graphene is still a subject of debate and is likely to play a role [39,75,80,81], but quantitative analysis is still lacking. This effect will be present on any surface-exposed graphene sensor and therefore this range in parameters may represent a limit of the possible consistency between devices using pristine graphene. Moreover, the more pristine the initial graphene the bigger the effect of small amounts of contaminants are likely to be, as the DP and DoS can suddenly vary with small changes in environment [21].

The effect of re-using a device, that is when the electrolyte is removed and replaced by another droplet, caused the results to change dramatically, as shown in Figure 4.4.1. This is thought to be due to the electrolyte drying on the device surface and not re-solubilising when the droplet was replaced. The electrolyte contamination could cause changes in the effective

surface area, concentration and doping, giving increased or decreased currents. Electrolyte contamination could increase the current due to increased concentration on the surface, but also decrease the current if the contamination crystallises on the surface and therefore blocks electron transfer in this area of the electrode. Electrode contamination due to redox products interfering with surfaces is a well-known effect for particular measurements such as the oxidation NADH [160,161] and this is likely to be a factor in certain graphene measurements. Several repeat measurements could also worsen the leaking effect previously discussed, giving an increased current over repeated measurements. These effects need to be carefully considered if a re-useable device is required, however in this research only the data from the first droplet was analysed to avoid this problem.

6.4 Kinetic parameters and substrate effects

The values of k^0 from the experimental data have a relatively high degree of uncertainty. Although the errors from the fitting procedure are small (~ 5 %), the range in results is much larger than this and the experimental errors on the other variables can lead to large (> 20 %) changes in k^0. The error on the formal potential, $E^{0'}$ only has a minor effect when k^0 is small (< 0.01 cms^{-1}). However, when comparing the values of k^0 to similar previous data studying $IrCl_6^{2-}$ redox with graphene electrodes, differences of an order of magnitude are seen. The closest measurements made to those presented in this thesis are the work of *M. Velicky et al.* [75]. In this study mechanically exfoliated flakes were deposited on SiO_2 surfaces and the standard rate constant measured for $IrCl_6^{2-}$ redox on a variety of thicknesses of graphite, including several monolayer graphene samples. The measurements were taken on the basal plane with no edge effect. The technique used means no extensive fabrication was required, as the graphene was contacted using Ag paint and the electrochemistry was performed in a small deposited droplet, meaning the surface was free from polymer contamination (although still atmosphere exposed). An average k^0 value of 34.8 ± 0.47 $\times 10^{-3}$ cms^{-1} was measured for graphene, which is over an order of magnitude larger than the value measured for the work presented in this thesis. Another study [137] using a similar method to *M. Velicky et al.* but with the graphene on a polymer substrate measures k^0 as 3.08 $\times 10^{-3}$ cms^{-1}, which is a very similar value measured for the devices presented in this thesis. $IrCl_6^{2-}$ redox typically shows fast electron transfer kinetics on most surfaces with $k^0 > 10 \times 10^{-3}$ cms^{-1} [149,154,162].

It can be suggested that the substrate may play a key role in the difference between the values for graphene on h-BN and polymer substrates and SiO_2 substrates. The effect of increased chemical reactivity on certain substrate surfaces is well established [45,90], with charged impurities causing substrate doping effects that cause the higher reactivity. With charged

impurities present, the Fermi level in the graphene above is shifted to higher or lower energy depending on the type of impurity, with the overall effect being the creation of electron-hole 'puddles', as described in Section 2.5. These puddles can then facilitate increased reaction rate where they form compared to the un-doped areas. Uncharged polymers and h-BN both have low charge defect density and SiO_2 has a high charge defect density. The fact that high reactivity is seen on atomically smooth mica [90] (a charged surface) suggests that charged impurities are a bigger factor than surface roughness.

This effect has never been directly studied electrochemically and the lower than expected k^0 values for graphene on h-BN is thought to be due to this substrate effect. In particular, reducing contamination from polymers would usually lead to an increased k^0 as contamination acts as a potential barrier to electron transfer. These results show the opposite trend. Alongside this fact, the substrate is the main difference when comparing to the results of *M. Velicky et al.* [75].

The other important factor is the potential dependence of the DoS. The standard transfer constant should in fact change with potential, although this effect is not compatible with the Butler-Volmer formulation. Figure 5.3.1 shows the effect of letting α vary as a linear function of potential. This suggest at higher potentials away from the DP (assumed to be ~ -0.2 V vs Ag/AgCl in other studies [39,150]) α approaches 0.5 then drops to smaller values towards the DP. This effect could indicate that the changing DoS with potential is reflected in the fitting to the O-Z formula as a potential dependence of α. Again, the Butler-Volmer formulation does not take this into account and cannot be used to give a precise physical explanation of the potential dependence of α. Over the large potential ranges measured for the reduction process in this work (> 700 meV) it is possible that α would not be a constant even on metallic surfaces, so this complicates the analysis further [37]. It is clear from the reduction data that α is always less than 0.5 and future work on graphene should take this into account even if assumed a constant.

The application of Marcus-Gerischer theory would be needed to draw physical parameters that include the contribution from the electrode DoS and to see if the linear potential dependence of α is due to this. As previously stated, the DP position and doping are rarely consistent between devices and change with variables such as solution molarity [163]. The DP and DoS would need to be measured whilst performing electrochemical measurements to apply the theory accurately, as discussed in Chapter 7.

7. Conclusions and future work

This chapter summarises the key findings of the thesis and suggests what direction future work could take and how this could be implemented.

7.1 Thesis conclusions

Overall the main aims of this project were completed. The successful design and operation of an electrochemical device was validated by the results attained. The method for defining the electrochemically active area of the graphene without using polymers was proven by measuring current densities for the reduction of $IrCl_6^{2-}$. This research is the first example of a general-use micron scale graphene electrochemical device structure that does not use polymers or lithography to achieve a well-defined electrode area. The expected characteristics of a UME were observed with increasing CV scan rate having little effect on the electrochemical response. Raman data and DF optical microscopy showed the graphene to be of the highest quality, both before and after electrochemical measurements.

This research also presents the first example of electrochemical redox data from graphene on a h-BN substrate. The comparison to previous work suggests the substrate reduces the standard rate constant, k^0, due to reductions in substrate doping, although further independent study would ideally need to be done to confirm this effect.

The values of the standard rate constant showed relatively large variation between devices, demonstrating graphene's susceptibility to varying environmental conditions. Values of the transfer coefficient, α, were less than the commonly assumed value of 0.5 and appeared to show some potential dependence over the large potential ranges required to reach steady-state current. Due to this potential dependence, future modelling of graphene electrochemical response may be more accurate using a theory such as that proposed by Marcus-Gerischer, taking into account the change in DoS with potential.

7.2 Future work

There is a great potential for future work stemming from this project. The fundamental properties of electrochemical reactions at graphene electrodes could be investigated further, alongside new measurements looking into the sensing capabilities of the novel electrode structure.

Determining the Dirac point of the graphene electrode

The Butler-Volmer formulation for electron transfer at graphene electrodes is not a complete model and cannot account for the theoretically negligible DoS at the DP. Marcus-Gerischer theory gives the possibility of applying a more general model to electron transfer with which the electron transfer constant includes the contribution from the electrodes DoS as a function of electrode potential. Applying this accurately to graphene would require this DoS function to be known under the experimental conditions present when performing redox measurements. Devices encapsulated by two layers of h-BN with no interaction with the atmosphere still show deviations in the DP energy and electron transport properties between devices, and this difference is increased when exposed to the atmosphere or electrolytes [164]. If the DP and transport properties of a graphene sample could be experimentally determined whilst also making electrochemical measurements, this would allow a more precise theory to be applied to electron transfer at graphene surfaces.

It may be possible to determine the minimum in the DoS via capacitance measurements [150], but making capacitance measurements on this device structure would require the parasitic capacitance to be reduced. This could easily be done by using a thicker SiN_x layer on the device substrate, with the parasitic capacitance reducing linearly with increased thickness. Reducing the size of the Au electrode contacting the graphene would also help reduce parasitic capacitance. If combining these two measures reduced the capacitance sufficiently to measure the capacitance minimum of the electrode, this would be a good starting point to applying Marcus-Gerischer theory. Alongside this, measuring a range of outer sphere redox mediators over a range of potentials and comparing the results would also reveal useful information on the DoS dependence on electron transfer rates [128].

Ideally electron transport measurements with a FET geometry are needed to get precise information on the DP and how the DoS changes with potential. A FET geometry device could be patterned and transferred on to the device structure presented in this thesis, with the FET gate potential being applied in the electrolyte solution across the EDL. This would allow accurate electron transport and electrochemical measurements to be made on the same device. A FET geometry would require edges exposed to the electrolyte, as the entire width of a graphene sheet would need be to in contact with electrolyte to ensure an equal gate potential is applied to the current flow. These edges could change the electrochemical properties, complicating the analysis of such data. However, these measurements would still help build a picture of how the graphene interacts with electrolytes around the DP.

For these measurements, using '*stamp*' transfer techniques [73] would keep the graphene in the best possible condition and avoid the dilute KOH exposure resulting from '*wet*' transfer. Stamp transfer compatible flakes generally have smaller area when fabricated via mechanical exfoliation. Large flakes are generally too strongly bound to the initial substrate to allow them to be moved without damage between substrates via a PMMA stamp. However, the devices presented in this thesis could be easily scaled down to match the reduced graphene flake dimensions.

Sensing measurements and surface functionalisation

The minimum detection limit of a redox mediator or biological analyte was not investigated in this thesis. This device structure could be ideal for sensing measurements, particularly if the clean fabrication method results in higher SNR for analyte detection. Due to the comparably small values of k^0 measured and the large potential range required to reach steady-state current on this device structure, it is likely that analyte sensing via redox measurements would have poor characteristics, as a useful sensing surface requires fast kinetics and the ability to resolve competing redox processes over small potential ranges. However, this does not necessarily mean that other sensing regimes would not be suited to this device. Measurements that observe charging of the quantum capacitance near the DP [44] could be particularly sensitive on pristine graphene samples with low doping. As stated above, reduction of the parasitic capacitance would be required for these measurements to be feasible. Most useful sensors require some form of surface functionality to improve analyte selectivity. Investigating surface functionalities such as proteins bound to the electrode surface would be the next logical step towards a fully functioning sensor.

References

1. Novoselov, K. S. *et al.* Electric field effect in atomically thin carbon films. *Science* **306,** 666–669 (2004).
2. Lee, C., Wei, X., Kysar, J. W. & Hone, J. Measurement of the Elastic Properties and Intrinsic Strength of Monolayer Graphene. *Science (80-.).* **321,** 385–388 (2008).
3. Geim, A. K. & Kim, P. Carbon Wonderland. *Sci. Am.* 90 (2008).
4. Hu, S. *et al.* Proton transport through one-atom-thick crystals. *Nature* **516,** 227–230 (2014).
5. Blake, P. *et al.* Making graphene visible. *Appl. Phys. Lett.* **91,** 198–201 (2007).
6. Balandin, A. A. *et al.* Superior thermal conductivity of single-layer graphene. *Nano Lett.* **8,** 902–907 (2008).
7. Hill, E. W., Vijayaragahvan, A. & Novoselov, K. Graphene sensors. *IEEE Sens. J.* **11,** 3161–3170 (2011).
8. Schedin, F. *et al.* Detection of individual gas molecules adsorbed on graphene. *Nat. Mater.* **6,** 652–655 (2007).
9. Kravets, V. G. *et al.* Singular phase nano-optics in plasmonic metamaterials for label-free single-molecule detection. *Nat. Mater.* **12,** 304–9 (2013).
10. Garcia-Sanchez, D. *et al.* Imaging mechanical vibrations in suspended graphene sheets. *Nano Lett.* **8,** 1399–1403 (2008).
11. Bitounis, D., Ali-Boucetta, H., Hong, B. H., Min, D. H. & Kostarelos, K. Prospects and challenges of graphene in biomedical applications. *Adv. Mater.* **25,** 2258–2268 (2013).
12. Wu, S., He, Q., Tan, C., Wang, Y. & Zhang, H. Graphene-based electrochemical sensors. *Small* **9,** 1160–1172 (2013).
13. Brownson, D. a. C. & Banks, C. E. The electrochemistry of CVD graphene: progress and prospects. *Phys. Chem. Chem. Phys.* **14,** 8264 (2012).
14. Czolkos, I., Jesorka, A. & Orwar, O. Molecular phospholipid films on solid supports. *Soft Matter* **7,** 4562 (2011).
15. Li, T. *et al.* Microelectrode Electrochemistry with semiconducting microelectrode chips. *Small* **10,** 878–883 (2014).
16. Chen, S. & Kucernak, A. The voltammetric response of nanometer-sized carbon electrodes. *J. Phys. Chem. B* **106,** 9396–9404 (2002).
17. Bond, A. M., Oldham, K. B. & Zoski, C. G. Steady-state voltammetry. *Anal. Chim. Acta* **216,** 177–230 (1989).
18. Chen, S. & Kucernak, A. Fabrication of carbon microelectrodes with an effective radius of 1 nm. *Electrochem. commun.* **4,** 80–85 (2002).
19. Novoselov, K. S. *et al.* A roadmap for graphene. *Nature* **490,** 192–200 (2012).
20. Cooper, D. R. *et al.* Experimental Review of Graphene. *ISRN Condensed Matter Physics* **2012,** 1–56 (2012).
21. Kretinin, A. V. *et al.* Electronic properties of graphene encapsulated with different two-dimensional atomic crystals. *Nano Lett.* **14,** 3270–3276 (2014).
22. Chen, J.-H., Jang, C., Xiao, S., Ishigami, M. & Fuhrer, M. S. Intrinsic and extrinsic performance limits of graphene devices on SiO2. *Nat. Nanotechnol.* **3,** 206–209 (2008).
23. Cheng, Z. *et al.* Toward Intrinsic Graphene Surfaces : A Systematic Study on. *Nano Lett.* **11,** 767–771 (2011).
24. Dean, C. R. *et al.* Boron nitride substrates for high-quality graphene electronics. *Nat. Nanotechnol.* **5,** 722–726 (2010).
25. Lin, Y. C. *et al.* Graphene annealing: How clean can it be? *Nano Lett.* **12,** 414–419 (2012).

26. Slater, J. C. & Koster, G. F. Simplified LCAO method for the periodic potential problem. *Phys. Rev.* **94,** 1498–1524 (1954).

27. Wallace, P. R. The band theory of graphite. *Phys. Rev.* **71,** 622–634 (1947).

28. Castro Neto, a. H., Guinea, F., Peres, N. M. R., Novoselov, K. S. & Geim, a. K. The electronic properties of graphene. *Rev. Mod. Phys.* **81,** 109–162 (2009).

29. Moudgil, H. K. *Textbook of Physical Chemistry*. (PHI Learning Pvt. Ltd., 2014).

30. Li, X. *et al.* Large-area synthesis of high-quality and uniform graphene films on copper foils. *Science* **324,** 1312–1314 (2009).

31. Du, X., Skachko, I., Barker, A. & Andrei, E. Y. Approaching ballistic transport in suspended graphene. *Nature nanotechnology* **3,** 491–495 (2008).

32. Lafkioti, M. *et al.* Graphene on a hydrophobic substrate: Doping reduction and hysteresis suppression under ambient conditions. *Nano Lett.* **10,** 1149–1153 (2010).

33. Bolotin, K. I. *et al.* Ultrahigh electron mobility in suspended graphene. *Solid State Commun.* **146,** 351–355 (2008).

34. Luryi, S. Quantum capacitance. *Appl. Phys. Lett.* **52,** 501 (1988).

35. Voigtländer, B. *Scanning Probe Microscopy: Atomic Force Microscopy and Scanning Tunneling Microscopy*. (Springer Berlin Heidelberg, 2015).

36. Yu, G. L. *et al.* Interaction phenomena in graphene seen through quantum capacitance. *Proc. Natl. Acad. Sci. U. S. A.* **110,** 3282–6 (2013).

37. Bard, A. J. & Faulkner, L. R. *Electrochemical Methods: Fundamentals and Applications, 2nd Edition*. (John Wiley & Sons, Inc., 2001).

38. Xia, J., Chen, F., Li, J. & Tao, N. Measurement of the quantum capacitance of graphene. *Nat. Nanotechnol.* **4,** 505–509 (2009).

39. Guell, A. G. *et al.* Redox-Dependent Spatially Resolved Electrochemistry at Graphene and Graphite Step Edges. *ACS Nano* 3558–3571 (2015).

40. Heller, I., Kong, J., Williams, K. a., Dekker, C. & Lemay, S. G. Electrochemistry at single-walled carbon nanotubes: The role of band structure and quantum capacitance. *J. Am. Chem. Soc.* **128,** 7353–7359 (2006).

41. Stoller, M. D. *et al.* Interfacial capacitance of single layer graphene. *Energy Environ. Sci.* **4,** 4685 (2011).

42. Heiman, F. P. & Warfield, G. Space-Charge Capacitance of an Intrinsic Semiconductor Film. *J. Appl. Phys.* **36,** 3206 (1965).

43. Ji, H. *et al.* Capacitance of carbon-based electrical double-layer capacitors. *Nat. Commun.* **5,** 1–7 (2014).

44. Wang, Y. Y., Pham, T. D., Zand, K., Li, J. & Burke, P. J. Charging the quantum capacitance of graphene with a single biological ion channel. *ACS Nano* **8,** 4228–4238 (2014).

45. Wang, Q. H. *et al.* Understanding and controlling the substrate effect on graphene electron-transfer chemistry via reactivity imprint lithography. *Nat. Chem.* **4,** 724–732 (2012).

46. Elias, D. C. *et al.* Control of graphene's properties by reversible hydrogenation: evidence for graphane. *Science (80-.).* **323,** 610–613 (2009).

47. Choi, M. S., Lee, S. H. & Yoo, W. J. Plasma treatments to improve metal contacts in graphene field effect transistor. *J. Appl. Phys.* **110,** (2011).

48. Loh, K. P., Bao, Q., Ang, P. K. & Yang, J. The chemistry of graphene. *J. Mater. Chem.* **20,** 2277 (2010).

49. Sharma, R., Baik, J. H., Perera, C. J. & Strano, M. S. Anomalously large reactivity of single graphene layers and edges toward electron transfer chemistries. *Nano Lett.* **10,** 398–405 (2010).

50. Koehler, F. M., Jacobsen, A., Ihn, T., Ensslin, K. & Stark, W. J. Chemical modification of

graphene characterized by Raman and transport experiments. *Nanoscale* **4,** 3781 (2012).

51. Lu, Y. *et al.* Graphene-protein bioelectronic devices with wavelength-dependent photoresponse. *Appl. Phys. Lett.* **100,** 22–25 (2012).
52. Park, S. J. *et al.* Ultrasensitive flexible graphene based field-effect transistor (FET)-type bioelectronic nose. *Nano Lett.* **12,** 5082–5090 (2012).
53. Gao, W., Alemany, L. B., Ci, L. & Ajayan, P. M. New insights into the structure and reduction of graphite oxide. *Nat. Chem.* **1,** 403–408 (2009).
54. William S. Hummers, J. & Offeman, R. E. Preparation of Graphitic Oxide. *J. Am. Chem. Soc* **80,** 1339 (1958).
55. Myung, S. *et al.* Graphene-encapsulated nanoparticle-based biosensor for the selective detection of cancer biomarkers. *Adv. Mater.* **23,** 2221–2225 (2011).
56. Liu, Y., Yu, D., Zeng, C., Miao, Z. & Dai, L. Biocompatible graphene oxide-based glucose biosensors. *Langmuir* **26,** 6158–6160 (2010).
57. Liu, H., Liu, Y. & Zhu, D. Chemical doping of graphene. *J. Mater. Chem.* **21,** 3335 (2011).
58. Wehling, T. O. *et al.* Molecular doping of graphene. *Nano Lett.* **8,** 173–177 (2008).
59. Shih, C. J. *et al.* Understanding surfactant/graphene interactions using a graphene field effect transistor: Relating molecular structure to hysteresis and carrier mobility. *Langmuir* **28,** 8579–8586 (2012).
60. Panchakarla, L. S. *et al.* Synthesis, structure, and properties of boron- and nitrogen-doped graphene. *Adv. Mater.* **21,** 4726–4730 (2009).
61. Rai-Choudhury, P. *Handbook of Microlithography, Micromachining, and Microfabrication: Microlithography*. (SPIE Press, 1997).
62. Kim, H. H. *et al.* Substrate-induced solvent intercalation for stable graphene doping. *ACS Nano* **7,** 1155–1162 (2013).
63. Bissett, M. a., Konabe, S., Okada, S., Tsuji, M. & Ago, H. Enhanced chemical reactivity of graphene induced by mechanical strain. *ACS Nano* **7,** 10335–10343 (2013).
64. Li, X. *et al.* Transfer of Large-Area Graphene Films for High-Performance Transparent Conductive Electrodes. *Nano Lett.* **9,** 4359–4363 (2009).
65. Borin Barin, G. *et al.* Optimized graphene transfer: Influence of polymethylmethacrylate (PMMA) layer concentration and baking time on graphene final performance. *Carbon N. Y.* **84,** 82–90 (2015).
66. Fan, J. *et al.* Investigation of the influence on graphene by using electron-beam and photo-lithography. *Solid State Commun.* **151,** 1574–1578 (2011).
67. Ishigami, M., Chen, J. H., Cullen, W. G., Fuhrer, M. S. & Williams, E. D. Atomic structure of graphene on SiO2. *Nano Lett.* **7,** 1643–1648 (2007).
68. Liu, Y. & Freund, M. S. Influence of Organic Solvents on the Kinetics of Electron Transfer and the Adsorption at Highly Ordered Pyrolytic Graphite. *Langmuir* **16,** 283–286 (2000).
69. Koenig, S. P., Wang, L., Pellegrino, J. & Bunch, J. S. Selective molecular sieving through porous graphene. *Nat. Nanotechnol.* **7,** (2012).
70. Ziegler, K. J. *et al.* Controlled oxidative cutting of single-walled carbon nanotubes. *J. Am. Chem. Soc.* **127,** 1541–1547 (2005).
71. Hernandez, Y. *et al.* High-yield production of graphene by liquid-phase exfoliation of graphite. *Nat. Nanotechnol.* **3,** 563–568 (2008).
72. Wang, Y. Y. & Burke, P. J. A large-area and contamination-free graphene transistor for liquid-gated sensing applications. *Appl. Phys. Lett.* **103,** (2013).
73. Wang, L. *et al.* One-dimensional electrical contact to a two-dimensional material. *Science* **342,** 614–7 (2013).
74. Lei, N., Li, P., Xue, W. & Xu, J. Simple graphene chemiresistors as pH sensors: fabrication

and characterization. *Meas. Sci. Technol.* **107002,** (2011).

75. Velický, M. *et al.* Electron Transfer Kinetics on Mono- and Multilayer Graphene. *ACS Nano* **8,** 10089–10100 (2014).
76. Valota, A. T. *et al.* Electrochemical behaviour of monolayer and bilayer graphene. 20 (2011).
77. Ang, P. K. *et al.* A Bioelectronic Platform Using a Graphene− Lipid Bilayer Interface. *ACS Nano* **4,** 7387–7394 (2010).
78. Levesque, P. L. *et al.* Probing charge transfer at surfaces using graphene transistors. *Nano Lett.* **11,** 132–137 (2011).
79. Gass, M. H. *et al.* Free-standing graphene at atomic resolution. *Nat. Nanotechnol.* **3,** 676–681 (2008).
80. Haigh, S. J. *et al.* Cross-sectional imaging of individual layers and buried interfaces of graphene-based heterostructures and superlattices. *Nat. Mater.* **11,** 764–767 (2012).
81. Li, Z. *et al.* Effect of airborne contaminants on the wettability of supported graphene and graphite. *Nat. Mater.* **12,** 925–31 (2013).
82. Lai, S. C. S., Patel, A. N., McKelvey, K. & Unwin, P. R. Definitive evidence for fast electron transfer at pristine basal plane graphite from high-resolution electrochemical imaging. *Angew. Chemie - Int. Ed.* **51,** 5405–5408 (2012).
83. Patel, A. N. *et al.* A new view of electrochemistry at highly oriented pyrolytic graphite. *J. Am. Chem. Soc.* **134,** 20117–20130 (2012).
84. Robinson, R. S. Morphology and Electrochemical Effects of Defects on Highly Oriented Pyrolytic Graphite. *J. Electrochem. Soc.* **138,** 2412 (1991).
85. Velicky, M. *et al.* Electron transfer kinetics on natural crystals of MoS 2 and graphite. *Phys. Chem. Chem. Phys.* 23–26 (2015).
86. Fan, X., Nouchi, R. & Tanigaki, K. Effect of charge puddles and ripples on the chemical reactivity of single layer graphene supported by SiO2/Si substrate. *J. Phys. Chem. C* **115,** 12960–12964 (2011).
87. Martin, J. *et al.* Observation of Electron-Hole Puddles in Graphene Using a Scanning Single Electron Transistor. *Nat. Phys.* **4,** 13 (2007).
88. Xu, G. *et al.* Effect of spatial charge inhomogeneity on 1/f noise behavior in graphene. *Nano Lett.* **10,** 3312–3317 (2010).
89. Zhang, Y., Brar, V. W., Girit, C., Zettl, A. & Crommie, M. F. Origin of Spatial Charge Inhomogeneity in Graphene. *Nat. Phys.* **5,** 722–726 (2009).
90. Yamamoto, M., Einstein, T. L., Fuhrer, M. S. & Cullen, W. G. Charge inhomogeneity determines oxidative reactivity of graphene on substrates. *ACS Nano* **6,** 8335–8341 (2012).
91. Rudenko, A. N., Keil, F. J., Katsnelson, M. I. & Lichtenstein, A. I. Graphene adhesion on mica: Role of surface morphology. *Phys. Rev. B* **83,** 45409 (2011).
92. Liu, Z., Bol, A. A. & Haensch, W. Large-scale graphene transistors with enhanced performance and reliability based on interface engineering by phenylsilane self-assembled monolayers. *Nano Lett.* **11,** 523–528 (2011).
93. Yokota, K., Takai, K. & Enoki, T. Carrier control of graphene driven by the proximity effect of functionalized self-assembled monolayers. *Nano Lett.* **11,** 3669–3675 (2011).
94. Paciĺ, D., Meyer, J. C., Girit, Ç. & Zettl, a. The two-dimensional phase of boron nitride: Few-atomic-layer sheets and suspended membranes. *Appl. Phys. Lett.* **92,** 212–214 (2008).
95. Geim, a K. & Grigorieva, I. V. Van der Waals heterostructures. *Nature* **499,** 419–25 (2013).
96. Woods, C. R. *et al.* Commensurate–incommensurate transition in graphene on hexagonal boron nitride. *Nat. Phys.* **10,** 1–6 (2014).

97. Sachs, B., Wehling, T. O., Katsnelson, M. I. & Lichtenstein, a. I. Adhesion and electronic structure of graphene on hexagonal boron nitride substrates. *Phys. Rev. B - Condens. Matter Mater. Phys.* **84,** 1–7 (2011).

98. Abergel, D. S. L., Russell, a. & Fal'Ko, V. I. Visibility of graphene flakes on a dielectric substrate. *Appl. Phys. Lett.* **91,** 2007–2009 (2007).

99. Casiraghi, C. *et al.* Rayleigh imagging of graphene and graphene layers. *Nano Lett.* **7,** 2711–2717 (2007).

100. Goossens, a. M. *et al.* Mechanical cleaning of graphene. *Appl. Phys. Lett.* **100,** 98–101 (2012).

101. Ferrari, a. C. *et al.* Raman spectrum of graphene and graphene layers. *Phys. Rev. Lett.* **97,** 1–5 (2006).

102. Ferrari, A. C. Raman spectroscopy of graphene and graphite: Disorder, electron-phonon coupling, doping and nonadiabatic effects. *Solid State Commun.* **143,** 47–57 (2007).

103. Casiraghi, C. Probing disorder and charged impurities in graphene by Raman spectroscopy. *Phys. Status Solidi - Rapid Res. Lett.* **3,** 175–177 (2009).

104. Casiraghi, C., Pisana, S., Novoselov, K. S., Geim, a. K. & Ferrari, a. C. Raman fingerprint of charged impurities in graphene. *Appl. Phys. Lett.* **91,** 24–27 (2007).

105. Das, a *et al.* Monitoring dopants by Raman scattering in an electrochemically top-gated graphene transistor. *Nat. Nanotechnol.* **3,** 210–215 (2008).

106. Ni, Z. H. *et al.* Uniaxial strain on graphene: Raman spectroscopy study and band-gap opening. *ACS Nano* **2,** 2301–2305 (2008).

107. Huang, M. *et al.* Phonon softening and crystallographic orientation of strained graphene studied by Raman spectroscopy. *Proc. Natl. Acad. Sci. U. S. A.* **106,** 7304–7308 (2009).

108. Mohiuddin, T. M. G. *et al.* Uniaxial strain in graphene by Raman spectroscopy: G peak splitting, Grüneisen parameters, and sample orientation. *Phys. Rev. B - Condens. Matter Mater. Phys.* **79,** 1–8 (2009).

109. Eckmann, A. *et al.* Raman fingerprint of aligned graphene/h-BN superlattices. *Nano Lett.* **13,** 5242–5246 (2013).

110. Forster, F. *et al.* Dielectric screening of the Kohn anomaly of graphene on hexagonal boron nitride. *Phys. Rev. B - Condens. Matter Mater. Phys.* **88,** 1–7 (2013).

111. Bard, A. J. & Faulkner, L. R. *Electrochemical Methods: Fundamentals and Applications*. *Analytica Chimica Acta* **677,** (2001).

112. Butt, H. J., Graf, K. & Kappl, M. Physics and Chemistry of Interfaces. (2006).

113. Liu, Y. & Chen, S. Electronic structure related electric-double-layer effects on heterogeneous ET kinetics on graphene electrode. *J. Electroanal. Chem.* **753,** 3–8 (2015).

114. Marcus, R. A. On the Theory of Oxidation-Reduction Reactions Involving Electron Transfer. I. *J. Chem. Phys.* **24,** 966 (1956).

115. H. Eyring, D.Henderson & W.Jost. *Physical Chemistry: An advanced treatise*. (Academic Press Inc., 1970).

116. Castro Neto, A. H., Peres, N. M. R., Novoselov, K. S. & Geim, A. K. The electronic properties of graphene. *Reviews of Modern Physics* **81,** 109–162 (2009).

117. Smith, E. An Examination of Some Methods for Obtaining Approximate Solutions to the Expanding-Sphere Boundary Value Problem in Direct Current Polarography. *J. Phys. Chemestry* **71,** 2138–2149 (1967).

118. Bond, A. M., Oldham, K. B. & Zoski, C. G. Theory of electrochemical processes at an inlaid disc microelectrode under steady-state conditions. *J. Electroanal. Chem. Interfacial Electrochem.* **245,** 71–104 (1988).

119. Oldham, K. B. & Zoski, C. G. Comparison of voltammetric steady states at hemispherical

and disc microelectrodes. *J. Electroanal. Chem. Interfacial Electrochem.* **256,** 11–19 (1988).

120. Mirkin, M. V & Bard, A. J. Simple Analysis of Quasi-Reversible Steady-State Voltammograms. *Anal. Chem.* **64,** 2293–2302 (1992).

121. Bond, A. M. & Mahon, P. J. Linear and non-linear analysis using the Oldham–Zoski steady-state equation for determining heterogeneous electrode kinetics at microdisk electrodes and digital simulation of the microdisk geometry with the fast quasi-explicit finite difference method. *J. Electroanal. Chem.* **439,** 37–53 (1997).

122. Bond, A. M., Luscombe, D., Oldham, K. D. & Zoski, C. G. Comparison of the Chronoamperometric Response At Inland and Recessed Disc Microelectrodes. *J. Electroanal. Chem. interfacial Electrochem.* **249,** 35–62 (1988).

123. Bartlett, P. N. & Taylor, S. L. An accurate microdisc simulation model for recessed microdisc electrodes. *J. Electroanal. Chem.* **453,** 49–60 (1998).

124. Guo, J. & Lindner, E. Cyclic Voltammetry at Shallow Recessed Microdisc Electrode: Theoretical and Experimental Study. *J. Electroanal. Chem.* **48,** 1–6 (2010).

125. Compton, R. G. & Banks, C. E. *Understanding Voltammetry*. (IC Publications, 2010).

126. Nicholson, R. S. Theory and Application of Cyclic Voltammetry for Measurement of Electrode Reaction Kinetics. *Anal. Chem.* **37,** 1351–1355 (1965).

127. Cline, K. K., Mcdermott, M. T. & Mccreery, R. L. Anomalously Slow Electron Transfer at Ordered Graphite Electrodes: Influence of Electronic Factors and Reactive Sites. *J. Phys. Chem.* **98,** 5314–5319 (1994).

128. Kneten, K. R. & Mccreery, R. L. Effects of redox system structure on electron-transfer kinetics at ordered graphite and glassy carbon electrodes. *Anal. Chem.* 2518–2524 (1992).

129. Nissim, R., Batchelor-McAuley, C., Henstridge, M. C. & Compton, R. G. Electrode kinetics at carbon electrodes and the density of electronic states. *Chem. Commun.* **48,** 3294 (2012).

130. Ambrosi, A., Chua, C. K., Bonanni, A. & Pumera, M. Electrochemistry of graphene and related materials. *Chem. Rev.* **114,** 7150–88 (2014).

131. Brownson, D. a. C., Munro, L. J., Kampouris, D. K. & Banks, C. E. Electrochemistry of graphene: not such a beneficial electrode material? *RSC Adv.* **1,** 978 (2011).

132. Blackman, L. C. F. & Ubbelohde, A. R. Stress recrystallization of graphite. *Proc. Roy. Soc. A* **266,** (1961).

133. Banerjee, S. *et al.* Electrochemistry at the edge of a single graphene layer in a nanopore. *ACS Nano* **7,** 834–843 (2013).

134. Ritzert, N. L. *et al.* Single layer graphene as an electrochemical platform. *Faraday Discuss.* 27–45 (2014).

135. McCreery, R. L. & McDermott, M. T. Comment on electrochemical kinetics at ordered graphite electrodes. *Anal. Chem.* **84,** 2602–2605 (2012).

136. Li, W., Tan, C. & Lowe, M. a. Electrochemistry of Individual Monolayer Graphene Sheets. 2264–2270 (2011).

137. Toth, P. S. *et al.* Electrochemistry in a drop: a study of the electrochemical behaviour of mechanically exfoliated graphene on photoresist coated silicon substrate. *Chem. Sci.* **5,** 582–9 (2014).

138. Various. *Faraday Discussions 172: Carbon in Electrochemistry*. (Royal Society of Chemistry).

139. Chen, R. *et al.* Ultrafast Electron Transfer Kinetics of Graphene Grown by Chemical Vapor Deposition. *Angew. Chemie Int. Ed.* 15349–15352 (2015).

140. Rafiee, J. *et al.* Wetting transparency of graphene. *Nat. Mater.* **11,** 217–222 (2012).

141. Tan, C. *et al.* Reactivity of monolayer chemical vapor deposited graphene imperfections

studied using scanning electrochemical microscopy. *ACS Nano* **6,** 3070–3079 (2012).

142. Bonanni, A. & Pumera, M. Surfactants used for dispersion of graphenes exhibit strong influence on electrochemical impedance spectroscopic response. *Electrochem. commun.* **16,** 19–21 (2012).

143. Zhang, B., Fan, L., Zhong, H., Liu, Y. & Chen, S. Graphene nanoelectrodes: Fabrication and size-dependent electrochemistry. *J. Am. Chem. Soc.* **135,** 10073–10080 (2013).

144. Yuan, W. *et al.* The edge- and basal-plane-specific electrochemistry of a single-layer graphene sheet. *Nat. Sci. reports* **3,** 2248 (2013).

145. Casero, E. *et al.* Differentiation between graphene oxide and reduced graphene by electrochemical impedance spectroscopy (EIS). *Electrochem. commun.* **20,** 63–66 (2012).

146. Brownson, D. a. C., Kelly, P. J. & Banks, C. E. In situ electrochemical characterisation of graphene and various carbon-based electrode materials: an internal standard approach. *RSC Adv.* **5,** 37281–37286 (2015).

147. Ferrari, A. C. *et al.* Science and technology roadmap for graphene, related two-dimensional crystals, and hybrid systems. *Nanoscale* **7,** 4598–4810 (2014).

148. Patten, H. V. *et al.* Electrochemistry of well-defined graphene samples: role of contaminants. *Faraday Discuss.* (2014).

149. Zhang, G., Cuharuc, A. S., Güell, A. G. & Unwin, P. R. Electrochemistry at highly oriented pyrolytic graphite (HOPG): lower limit for the kinetics of outer-sphere redox processes and general implications for electron transfer models. *Phys. Chem. Chem. Phys.* **17,** 11827–11838 (2015).

150. Gerischer, H., McIntyre, R., Scherson, D. & Storck, W. Density of the Electronic States of Graphite: Derivation from Differential Capacitance Measurements. *J. Phys. Chem.* **91,** 1930 (1987).

151. Zhong, J. *et al.* Quantitative Correlation between Defect Density and Heterogeneous Electron Transfer Rate of Single Layer Graphene. *J. Am. Chem. Soc.* **136,** 16609–16617 (2014).

152. Pant, B. D. & Tandon, U. S. Etching of Silicon Nitride in CCl2F2, CHF3, SiF4, and SF6 Reactive Plasma: A Comparative Study. *Plasma Chem. Plasma Process.* **19,** 545–563 (1999).

153. Seidel, H., Csepregi, L., Heuberger, A. & Baumgärtel, H. Anisotropic Etching of Crystalline Silicon in Alkaline Solutions. *J. Electrochem. Soc.* **137,** 3612 (1990).

154. Beriet, C. & Pletcher, D. A further microelectrode study of the influence of electrolyte concentration on the kinetics of redox couples. *J. Electroanal. Chem.* **375,** 213–218 (1994).

155. Watkins, J. J. & White, H. S. The role of the electrical double layer and ion pairing on the electrochemical oxidation of hexachloroiridate(III) at pt electrodes of nanometer dimensions. *Langmuir* **20,** 5474–5483 (2004).

156. Myland, J. C. & Oldham, K. B. Uncompensated resistance. 1. The effect of cell geometry. *Anal Chem* **72,** 3972–3980 (2000).

157. Xia, F., Perebeinos, V., Lin, Y., Wu, Y. & Avouris, P. The origins and limits of metal-graphene junction resistance. *Nat. Nanotechnol.* **6,** 179–184 (2011).

158. Cahill, B. P. *et al.* Reversible electrowetting on silanized silicon nitride. *Sensors Actuators, B Chem.* **144,** 380–386 (2010).

159. Zabel, J. *et al.* Raman spectroscopy of graphene and bilayer under biaxial strain: Bubbles and balloons. *Nano Lett.* **12,** 617–621 (2012).

160. Banks, C. E. & Compton, R. G. Exploring the electrocatalytic sites of carbon nanotubes for NADH detection: an edge plane pyrolytic graphite electrode study. *Analyst* **130,** 1232–1239 (2005).

161. Rao, T. N., Yagi, I., Miwa, T., Tryk, D. a. & Fujishima, a. Electrochemical oxidation of

NADH at highly boron-doped diamond electodes. *Anal. Chem.* **71,** 2506–2511 (1999).

162. Song, Y., Hu, H., Feng, M. & Zhan, H. Carbon Nanotubes with Tailored Density of Electronic States for Electrochemical Applications. *ACS Appl. Mater. Interfaces* **7,** 25793–25803 (2015).

163. Heller, I. *et al.* Influence of electrolyte composition on liquid-gated carbon nanotube and graphene transistors. *J. Am. Chem. Soc.* **132,** 17149–17156 (2010).

164. Levesque, P. L. *et al.* Probing charge transfer at surfaces using graphene transistors. *Nano Lett.* **11,** 132–137 (2011).